Time-Offset Fractional-N PLLs for Heterodyne FMCW SAR

Darryn Anton Jordan
Department of Electrical Engineering
University of Cape Town

Supervised By:
Dr. Mohammed Yunus Abdul Gaffar &
Prof. Emer. Michael Raymond Inggs
Department of Electrical Engineering
University of Cape Town

A thesis submitted to the Department of Electrical Engineering, University of Cape Town, in fulfilment of the requirements for the degree of Doctor of Philosophy.

March 2021

Declaration

1. I know that plagiarism is wrong. Plagiarism is to use another's work and pretend that it is one's own.
2. I have used the IEEE convention for citation and referencing. Each contribution to, and quotation in, this report from the work(s) of other people has been attributed, and has been cited and referenced.
3. This report is my own work.
4. I have not allowed, and will not allow, anyone to copy my work with the intention of passing it off as their own work or part thereof.

Signed by candidate

Darryn Anton Jordan
Cape Town, South Africa

Friday 26th March, 2021

Abstract

This text contains an investigation into the use of time-offset fractional-N phase locked loops (PLLs) for heterodyne frequency-modulated continuous-wave (FMCW) synthetic aperture radar (SAR) and the impact of spurii on such a system.

Heterodyne receiver architectures avoid phenomena which limit the sensitivity of their homodyne counterparts, and enable certain inter-antenna feed-through suppression techniques. Despite these advantages, homodyne receivers are more prevalent owing to advantages in size, weight and cost. Designed to address this dilemma, the *miloSAR* is believed to be the only heterodyne FMCW SAR to employ a pair of time-offset fractional-N PLLs for waveform synthesis to enable low-cost heterodyning and simplify filter-based feed-through suppression.

This system architecture is revealed to be susceptible to swept-offset spurii termed *spur chirps* which hinder the sensor's performance. While integer boundary spurs and phase detector harmonics infamously plague fractional-N PLLs, their resultant spur-chirps have not seen analysis in the context of FMCW SAR.

Simulations and measurements reveal that these spurii significantly degrade SAR image quality in terms of peak sidelobe ratio, structural similarity index measure and root mean square error. To combat this, several suppression techniques were assessed, namely: time domain zeroing, PLL loop bandwidth reduction, and a novel method termed *range-Doppler spur masking.*

A subset of these suppression techniques were applied to measured SAR data sets, including car-borne data measured in Iowa, USA and airborne data captured in Oudtshoorn, South Africa. These results show that the impact of spur chirps can be effectively quelled, meaning that time-offset fractional-N PLLs offer an attractive, low-cost approach to the implementation of heterodyne FMCW SAR.

Acknowledgements

I have numerous people to thank for my colourful postgraduate journey, which included imaging in Iowa, being airborne over ostriches in Oudtshoorn, and attempting to repair radars in Riyadh.

Foremost, I would like to thank my supervisors. Michael Raymond Inggs sparked my interest in radar during my undergraduate studies, encouraged me to pursue a masters, and then skilfully nudged me to upgrade to a PhD. He provided guidance, funding, support and motivation when I needed it most. I thank him for the major role he has played in my life. Mohammed Yunus Abdul Gaffar took me under his wing as a PhD candidate. He was always available to discuss hiccups along the way and kept me on the right path when all seemed lost. I am privileged to have had the opportunity to work under both of these exceptional individuals.

I'll never forget laughs and late nights in the radar lab with members of the Radar Remote Sensing Group (RRSG), including: Skippy Burger, Dominique Gouveia, Tighe Barris, Michael Malape, Jean Swart, Harry Mafukidze, Motlatsi Setsubi, Xavier Frans, Daniel Czech, Alexandra Filip, Laurent Krier, and Stephanie Jonkers. I especially thank Tinashe Gwatiringa, Po-Kai 'Randy' Cheng, Stephen Paine, Ming Gao and Simon Lewis for all the hours spent under the hot African sun, collecting data sets and listening to me complain about things that were never really all that bad. Your friendship made it all worthwhile.

Alan Langman, Gordon Inggs and Japie Ludick are thanked for their generous contributions to the project. Their hard work allowed me to pursue an exciting start-up opportunity and capture data sets in Iowa, USA. Alan is especially thanked for hours of technical discussions, financial contributions and laughs shared during this trip.

Airborne measurements in Oudtshoorn would not have been possible without the generosity of Jean Rossouw and his team at the Test Flight Academy of South Africa (TFASA). Thanks to Petri van Zyl and James O'Connell for keeping me safe in the air.

Without funding provided by the Technology Innovation Agency (TIA) of South Africa, droneSAR and Sigma0, this project would not have been possible.

My thanks go out to the anonymous reviewers of my publications, who volunteered their valuable time and provided insightful feedback.

Finally, I would like to thank my friends and family, for devising timeous distractions and putting up with me during this journey. Without the motivation, support, coaching and encouragement of my parents, Erich and Ingrid, and the love of my life, Sarah, I would not have made it to the end.

Publications

The research presented in this thesis has contributed to the following publications:

D. A. Jordan, M. R. Inggs and M. Y. Abdul Gaffar, “Suppression of spur chirps for fractional-N PLL-based heterodyne FMCW SAR,” *IEEE Trans. Microw. Theory Techn.*, vol. 69, no. 1, pp. 409–417, Jan. 2021, doi: 10.1109/TMTT.2020.3030273.

D. A. Jordan, M. R. Inggs and M. Y. Abdul Gaffar, “Integer boundary spur considerations for fractional-N PLL based FMCW radar,” *Electron. Lett.*, vol. 56, no. 14, pp. 729–732, Jul. 2020, doi: 10.1049/el.2020.0764.

D. A. Jordan, P. Cheng, M. R. Inggs, A. Langman and M. Y. Abdul Gaffar, “Development of the miloSAR testbed for the one kilogramme radioCamera SAR for small drones,” in *Proc. IEEE Radar Conf. (RadarConf)*, Apr. 2019, pp. 1–6, doi: 10.1109/RADAR.2019.8835721 (Presented).

D. A. Jordan, M. R. Inggs and D. O’Hagan, “NeXtLook a lightweight, real-time quick-look processor for NeXtRAD,” in *Proc. Int. Conf. Radar Syst.*, Oct. 2017, pp. 1–6, doi: 10.1049/cp.2017.0470 (Presented).

M. R. Inggs, D. A. Jordan and T. Learner, “Through the clouds: Exploring the potential of infrastructure-as-a-service for radar,” in *Proc. Int. Conf. Radar Syst.*, Oct. 2017, pp. 1–6, doi: 10.1049/cp.2017.0447 (Presented).

S. Alhuwaimel et al., “First measurements with NeXtRAD, a polarimetric X/L Band radar network,” in *Proc. IEEE Radar Conf. (RadarConf)*, May 2017, pp. 1663–1668, doi: 10.1109/RADAR.2017.7944474.

Contents

List of Figures

List of Tables

List of Acronyms

AC Alternating Current. 32

ADC Analogue-to-Digital Converter. 7, 18, 19, 34, 35, 37, 54–56

ADPLL All-Digital Phase-Locked Loop. 26

AGL Above Ground Level. 62, 109

AM Amplitude Modulation. 5, 17, 20, 21, 24, 25

ARM Advanced RISC Machine. 34, 36

AWG Additive White Gaussian. 57

BPF Band-Pass Filter. 5, 23, 25, 37, 52, 53, 76

CFAR Constant False Alarm Rate. 103–105, 122

CPG Charge Pump Gain. 7, 9, 29, 43, 69, 98–100, 117, 120

CW Continuous-Wave. 13

DAC Digital-to-Analogue Converter. 15, 55, 56

DC Direct Current. 4, 14, 17, 32, 37

DDC Digital Down-Converter/Conversion. 6, 17, 25, 36–39, 49, 52, 53, 69

DDS Direct Digital Synthesis. 4, 5, 15, 16, 21, 24, 25, 29, 30, 37, 122

DF Decimation Factor. 37, 38, 40

DR Data Rate. 36–39, 52, 69

DSB Double-Sideband. 17–20, 25

DVGA Digitally-Controlled Variable Gain Amplifier. 7, 55, 57

DX Dechirp. 1, 2, 5, 6, 8, 17–19, 21–25, 40, 47–49, 51, 52, 71–77, 122

ENBW Equivalent Noise Bandwidth. 54, 87

ENOB Effective Number of Bits. 34

FERS Flexible Extensible Radar Simulator. 86, 104

FFT Fast Fourier Transform. 54, 78, 97

FIFO First-In First-Out. 39

FIR Finite Impulse Response. 37–39

FM Frequency Modulation. 17, 78, 80

FMCW Frequency-Modulated Continuous-Wave. 1–13, 15–23, 26–31, 40, 47, 52, 69–71, 76, 86, 93, 94, 101, 117, 119–122

FMICW Frequency-Modulated Interrupted Continuous-Wave. 13, 22, 25

FPGA Field-Programmable Gate Array. 6, 34–36, 40, 69

GNSS Global Navigation Satellite System. 32, 40, 62, 67, 109

HEMT High-Electron-Mobility Transistor. 17, 18

HPF High-Pass Filter. 5, 23, 25

I/Q In-Phase/Quadrature. 17, 19–22, 25, 37

IBS Integer Boundary Spur. 5, 7, 8, 27, 30, 44–47, 69–78, 83, 84, 91, 93, 94, 97–99, 120

IF Intermediate Frequency. 2, 5, 8, 14, 16–19, 21–23, 25, 37, 48, 49, 52, 53, 55, 61, 69, 76–78, 80, 82, 83, 94, 119

IP Intellectual Property. 37

LO Local Oscillator. 4, 5, 16, 17, 37, 48, 49, 51

LPC Leakage Power Cancellation. 14

LPF Low-Pass Filter. 35, 37, 77

LSB Least-Significant Bit. 37

MCA Morphological Component Analysis. 97, 117

OMP Orthogonal Matching Pursuit. 97, 117

PDF Probability Density Function. 57

PDH Phase Detector Harmonic. 5, 7, 8, 28, 30, 46–48, 69–72, 76–78, 91, 93, 94, 98, 120

PLL Phase-Locked Loop. 2–11, 16, 21, 23–32, 35, 40–46, 48–50, 62, 69, 71, 72, 76, 77, 83, 93, 94, 98–101, 106, 111, 117, 119–122

PRF Pulse Repetition Frequency. 39, 40, 83, 111

PRI Pulse Repetition Interval. 37, 39, 40, 50

PS Power Spectrum. 54, 57

PSD Power Spectral Density. 54, 55, 57

PSLR Peak Sidelobe Ratio. 10, 89, 91, 92, 95, 106, 108, 117, 120

RBW Resolution Bandwidth. 35, 36, 44, 48, 54

RCS Radar Cross Section. 63, 88

RDM Range-Doppler Map. 8, 63, 65, 70, 83–86, 91, 98, 102–104, 111, 113, 114, 120, 122

RDSM Range-Doppler Spur Masking. 4, 9, 10, 93, 101–109, 111, 113–117, 120–122

RF Radio Frequency. 2, 6, 9, 14–16, 26–28, 32, 34, 40, 41, 46, 48, 70, 74, 76, 94, 98, 119

RGB Red, Green, Blue. 62, 65, 67

RMSE Root Mean Square Error. 10, 15, 89, 92, 106, 108, 117, 120

RPC Reflected Power Cancellation. 14

RTI Range-Time-Intensity. 62, 64, 65

RTK Real-Time Kinematic. 32, 62, 67, 109

RX Receive. 1, 2, 6, 12–14, 17–19, 22, 25, 34, 47, 58, 61, 75, 86

SA Spectrum Analyser. 35, 54–57

SAR Synthetic Aperture Radar. 3–10, 13, 15, 16, 21–23, 26–32, 36, 47, 60, 62–70, 85, 86, 89, 91, 98, 100, 102, 103, 106–111, 114, 117, 119–122

SATA Serial at Attachment. 34

SC Suppressed-Carrier. 17–20, 25

SFC Sensitivity Frequency Control. 14

SFDR Spurious-Free Dynamic Range. 7, 29, 37, 67, 69

SNR Signal-to-Noise Ratio. 17, 25, 39, 61, 65, 88, 89, 95, 111

SoC System-On-Chip. 34

SSB Single-Sideband. 17–20, 25

SSIM Structural Similarity Index Measure. 10, 89, 92, 106, 108, 117, 120

STC Sensitivity Time Control. 14

STFT Short-Time Fourier Transform. 79, 97

TCU Timing Control Unit. 6, 36, 40

TX Transmit. 1, 2, 5, 6, 8, 12–14, 16–25, 34, 40, 48, 49, 51, 52, 58, 61, 71–77, 86

UCT University of Cape Town. 62, 66

VCO Voltage-Controlled Oscillator. 9, 15, 18, 19, 21, 22, 24, 25, 27, 28, 32, 41, 43, 44, 46, 51, 74, 75, 78, 94, 97, 98, 100, 117

VH Vertical Transmit, Horizontal Receive. 62, 66, 115

VV Vertical Transmit, Vertical Receive. 62, 64, 66, 115

XO Crystal Oscillator. 34

Chapter 1

Introduction

Short-range remote sensing is required in numerous commercial and research applications, such as autonomous vehicle localisation, bulk-solids level measurement and low-altitude imaging. Radars are regularly employed for these applications, owing to their measurement of target range and radial velocity in all weather conditions, day or night. Unlike their pulsed counterparts, Frequency-Modulated Continuous-Wave (FMCW) radars are particularly well-suited for short-range sensing, since they do not suffer from a blind range and operate with low peak power levels. Furthermore, FMCW radars support high-resolution measurements, by combining digital processing and analogue dechirp [1].

Analogue dechirp (or *deramp*) is a down-conversion procedure in which Receive (RX) echoes are mixed with a reference Dechirp (DX) signal, and the product is filtered to extract a beat frequency. In a typical homodyne FMCW radar, as illustrated in Figure 1.1, the DX waveform is simply a coupled portion of the Transmit (TX) waveform. Analogue dechirp thus requires continuous operation, i.e. the radar is required to TX and RX simultaneously.

Continuous operation gives rise to a direct coupling signal known as *feed-through*, whose magnitude is typically much larger than that of any target echo. As a result, the radar's receiver gain is limited by feed-through, such that signal distortion and component damage are avoided. This is a necessary precaution, but leads to a reduction in the radar's effective dynamic range and sensitivity. Techniques for the suppression of feed-through are therefore highly desirable.

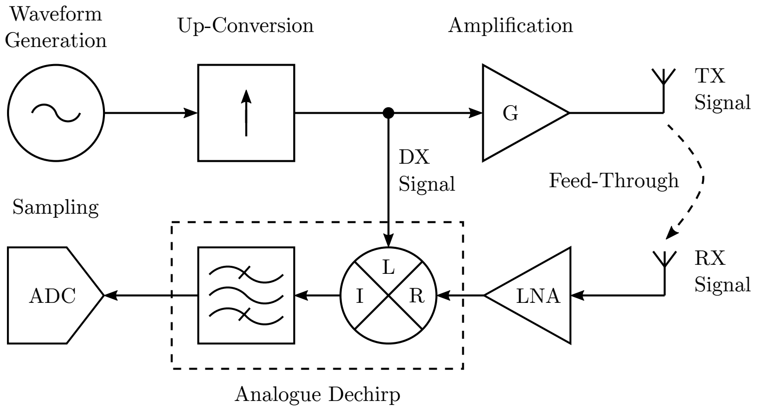

Figure 1.1: Block diagram of a generic homodyne FMCW radar. The path of the feed-through signal has been indicated between the TX and RX antennas.

Feed-through suppression techniques such as analogue range gating [1–3] and adaptive leakage cancellation [4–6] require that the radar employ a heterodyne receiver architecture. In addition to enabling these techniques, heterodyne receivers can avoid the infamous sensitivity-limiting phenomena that plague homodyne receivers [7, 8]. Despite these advantages, the homodyne receiver architecture remains ubiquitous in the field of FMCW, owing to comparative cost, size and weight advantages.

Tchekashkin [9] addressed this dilemma through the development of an unconventional heterodyne FMCW radar. His system used a pair of fractional-N Phase-Locked Loops (PLLs), such that the TX and DX waveforms could be synthesised individually. As such, a relative time and/or frequency offset could be introduced between the otherwise equivalent TX and DX waveforms to shift the beat spectrum to an adjustable Intermediate Frequency (IF). Fractional-N PLLs are inexpensive, and enable FMCW waveform synthesis directly at Radio Frequency (RF). They therefore eliminate the hardware required for mixer-based up-conversion, which leads to further reductions in system cost, size and weight. The developed heterodyne FMCW radar is therefore an attractive alternative to more conventional systems.

The author inherited Tchekashkin's system in 2016. At that time, the system operated non-coherently, featured a single polarisation and was limited to measurement lengths of under 8.59 s. Despite the system's intended application of low-cost imaging for small drones, it was clearly incapable of Synthetic Aperture Radar (SAR) operation at that stage. As such, the system required a partial redesign, characterisation and calibration before its implementation as a SAR.

In the course of system characterisation, it became clear that the radar's sensitivity was significantly limited by the infamous spurious output products that are generated by fractional-N PLLs. To the best of the author's knowledge, the impact of these spurs on heterodyne FMCW SAR imagery had not been addressed in the literature. As such, the viability of time-offset fractional-N PLLs for heterodyne FMCW SAR was not a certainty, giving rise to the project hypothesis.

1.1 Hypothesis

Time-offset fractional-N PLLs offer a low-cost approach for the implementation of heterodyne FMCW SAR.

1.2 Research Questions

The following research questions extend from the hypothesis and were posed to guide the research process.

1. Why use a pair of fractional-N PLLs to implement a heterodyne FMCW SAR?
2. Can such a radar operate coherently without a reference channel?
3. Do the notorious spurious signals generated by fractional-N PLLs affect the images produced by this SAR?
4. If these spurious signals do present a problem, how can they be suppressed effectively?

1.3 Statement of Originality

The following contributions are believed by the author to constitute original research.

1. Implementation of the only fully-polarimetric heterodyne FMCW SAR to employ a pair of time-offset fractional-N PLLs.
2. Identification, simulation and measurement of the *spur chirps* which affect this system.
3. Presentation of guidelines for the avoidance of spur chirps.
4. Identification of existing, transferable techniques for the suppression of spur chirps.
5. Demonstration of spur chirp suppression through PLL loop bandwidth reduction.
6. Presentation of Range-Doppler Spur Masking (RDSM): a novel spur chirp suppression technique.
7. A comparison between time-domain zeroing, loop bandwidth reduction and RDSM for the suppression of spur chirps, using simulated and measured SAR data.

1.4 Chapter Summary

The main findings of each chapter are discussed briefly in this section.

Chapter 2

This chapter presents a review of literature deemed pertinent to this thesis. First, the classic challenges of FMCW radar are presented, namely feed-through and frequency sweep linearity. Prevalent feed-through suppression techniques are briefly discussed, with focus on analogue range gating. Methods of FMCW waveform synthesis are then explored where Direct Digital Synthesis (DDS) and fractional-N PLL based synthesisers are identified as linear solutions.

Next, FMCW receiver architectures are reviewed. Phenomena which limit the sensitivity of the homodyne receiver (Direct Current (DC)-offset, Local Oscillator (LO) self-mixing, flicker noise, etc.) are noted. Case studies of systems

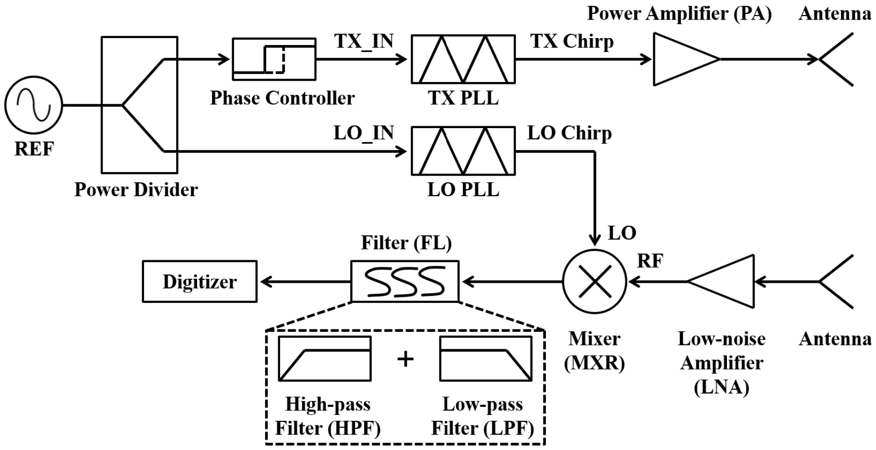

Figure 1.2: Time-offset heterodyne architecture developed by Kim *et al.* [11] A phase controller is used to advance the TX PLL with respect to the LO.

with heterodyne receivers, which can avoid the aforementioned phenomena, are categorised into three classes: Amplitude Modulation (AM), offset up-conversion, and time offset. Here, a gap in the literature is revealed: there exists no FMCW SAR which employs a pair of time-offset fractional-N PLLs for heterodyning.

The most similar work to the identified gap is likely the SlimSAR [10], which employs a pair of time-offset DDSs. The SlimSAR's IF is, however, mainly determined by a difference in the up-conversion factor applied to the output of each DDS, and is only adjusted using the time-offset between DDSs. In contrast, a gap exists for a system which only utilises the time-offset between PLLs to set the IF.

Kim *et al.* [11] developed a similar system: a heterodyne FMCW radar which employs time-offset fractional-N PLLs. Intended for wall-penetration applications, they use a phase controller to advance the TX waveform in time with respect to the DX, as illustrated in Figure 1.2. This serves to decrease the IF and increase the degree of clutter attenuation afforded by a low-order High-Pass Filter (HPF). Alternatively, in the identified gap each PLL could be programmed with a unique set of waveform parameters to introduce a relative time offset. Furthermore, the IF would be increased, rather than decreased, such that targets of interest pass through a range-gate based on a Band-Pass Filter (BPF).

Finally, a review of the spurious signals produced by fractional-N PLLs is presented. It is found that the impact of Integer Boundary Spur (IBS) and Phase

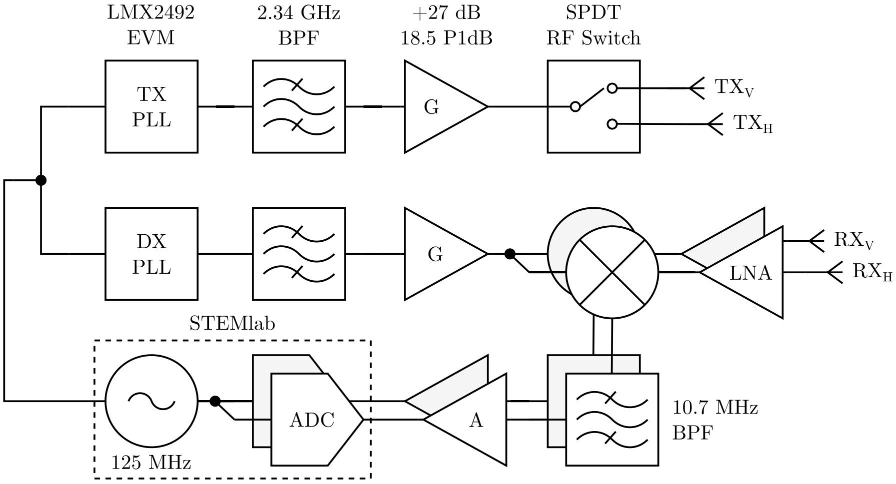

Figure 1.3: Block diagram of the miloSAR [12]. Fully polarimetric operation is enabled by the single-pole double-throw RF switch in the TX chain, in combination with the two RX channels.

Detector Harmonic (PDH) on the performance of heterodyne FMCW SAR has not been reported on, exposing a secondary gap to be addressed in this thesis.

Chapter 3

This chapter presents an overview of the miloSAR. The purpose of this overview is to provide the reader with a firm background on the system's functionality, upon which later chapters will build. Specifically, the overview provides context for the problem of *spur chirps*; an integral aspect of this thesis. For reference, a high-level block diagram of the developed system is provided in Figure. 1.3.

First, the STEMlab's pivotal role in the miloSAR is explored. The gateware developed specifically for its Field-Programmable Gate Array (FPGA) is assessed, namely a Digital Down-Converter/Conversion (DDC), profile integrator and Timing Control Unit (TCU). The radar's master clock source (generated by the STEMlab) is shown to contain spurs that propagate into in the synthesised TX and DX waveforms, and the resultant beat spectrum. These spurs are, however, eliminated through coherent integration.

Next, the radar's fractional-N PLL based waveform synthesisers are explored. PLL loop bandwidth is shown to be a critical design parameter, since it affects the linearity of the frequency sweep, the efficacy of analogue range gating, and the suppression of low-offset noise and spurs. The ability to adjust loop bandwidth using the Charge Pump Gain (CPG) is demonstrated. IBS and PDH are shown to be examples of spurious signals whose carrier offset varies during the generation of a frequency sweep.

Time- and frequency-offset approaches to heterodyning are compared. The time-offset approach is shown to eliminate the need for a reference channel, and is thus preferred over the frequency-offset approach. This is the initial step in addressing the second research question.

The results of a series of lab-based characterisation tests are presented. Noise generated by the receiver's cascaded Digitally-Controlled Variable Gain Amplifiers (DVGAs) set the system's noise floor to $-118.5\,\mathrm{dBm/Hz}$. Leakage within the system leads to zero-range interferers at a level of $-67.8\,\mathrm{dBm}$, and Analogue-to-Digital Converter (ADC) channel cross-talk is measured to be $57.7\,\mathrm{dB}$. The system's ability to accurately measure signal power, and precisely measure target magnitude and phase are demonstrated. The most important result of the characterisation tests is that coherent integration reveals spurious, coherent content in the sidebands of the radar's target response. This spurious content produces *ripples* throughout each range profile and significantly reduces the Spurious-Free Dynamic Range (SFDR).

Finally, the system's ability to produce polarimetric SAR images is illustrated through the results of a car-borne measurement campaign. Using a combination of reflectors, the radar's ability to accurately locate and distinguish between even- and odd-bounce targets is demonstrated. However, since the aforementioned ripple interference becomes apparent through coherent integration, SAR image quality is significantly deteriorated.

Chapter 4

This chapter presents a combination of theory, simulations and measurements to explain the origin and assess the impact of *spur chirps* in fractional-N PLL based FMCW SAR.

First, the origin of *spur chirps* is explored through analysis of a single fast-

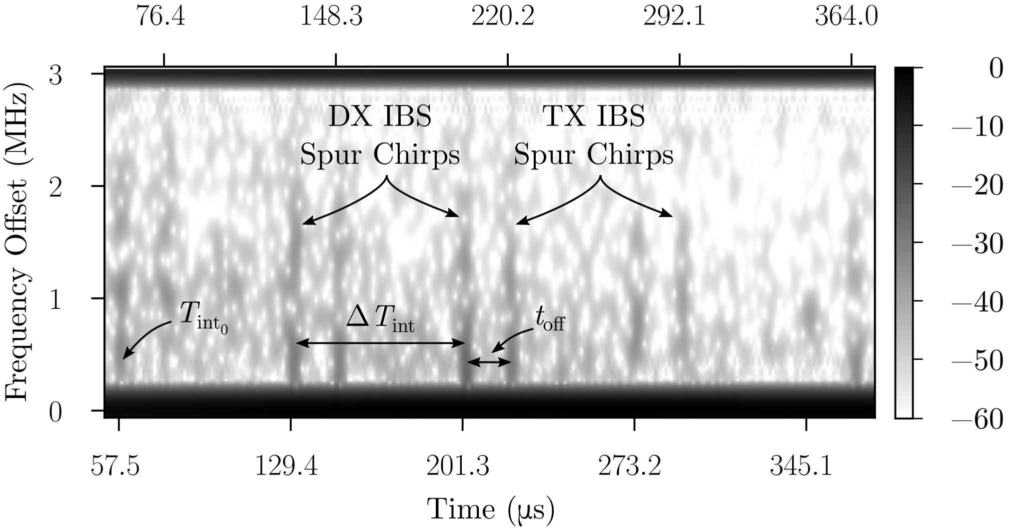

Figure 1.4: Identification of spur chirps in a spectogram of a measured beat signal. The time axis ticks have been selected to match the interference intersection points.

time point in the FMCW waveform cycle. At this point in time, the frequency offset of several IBS and PDH in the TX and DX spectra is accurately predicted and measured. Following dechirp, these spurs are shown to appear at the same offset in the beat spectrum. Since the offset of these spurs is a function of the PLL fractional numerator, which is swept through fast-time, it is the IBS and PDH that give rise to spur chirps in the beat signal.

The nature of spur chirps in the beat signal is then assessed through simulation and measurement of the IF spectrogram. The precise location of spur chirps in this spectrogram is demonstrated to be predictable, since their time-offset, duration, sweep-rate and bandwidth can be calculated. One such spectrogram is illustrated in Figure 1.4.

Next, the Fourier transform used for FMCW range compression is shown to transform the beat signal spur chirps into Fresnel ripples in the range domain. Simulations and measurements agree that these ripples oscillate throughout the compressed range profile with a period of δf_{VCO}. These Fresnel ripples are the source of interference that is observed in the SAR imagery of the preceding chapter.

The manifestation of spur chirps in the Range-Doppler Map (RDM) is then investigated by reassessing the single point in fast-time. The aliased Doppler frequency of several IBS is predicted and measured in an averaged RDM, where the spurs are distributed throughout the map. In the case of a full FMCW up-ramp, spur chirps are shown to appear at deterministic Doppler frequencies as Fresnel ripples throughout range.

Finally, quantitative assessment of the impact of spur chirps on SAR imagery is carried out through simulation. Two SAR images are formed of a single point target under different conditions: the case where spur chirps are absent versus present. All performance metrics agree that the spur chirps cause significant degradation to image quality, hindering the ability to distinguish targets from interference.

Chapter 5

In this chapter, several approaches for avoiding and mitigating the impact of spur chirp interference are presented and applied to simulated and measured SAR data sets for comparison.

Guidelines for the complete avoidance of spur chirps are put forward, including constraints on RF bandwidth, elimination of Voltage-Controlled Oscillator (VCO) dividers, and the use of a variable PLL reference frequency. Next, a set of suppression techniques, originally intended to combat automotive mutual interference, are identified as transferable to the problem of spur chirps. Of these techniques, time domain zeroing is selected for implementation as a baseline for comparison with alternatives.

Reduction of PLL loop bandwidth through adjustment of the CPG is then explored as a technique to address modulated spurs. While effective and simple to implement, this technique has the disadvantage of increasing PLL settling time and lowering the corner frequency of the VCO noise transfer function. Furthermore, it is ineffective for in the near range which corresponds to the PLL loop filter bandwidth.

A novel technique, developed specifically to combat spur chirp interference, is then put forward. Termed RDSM, this technique is computationally inexpensive and takes advantage of the sparsity of spur chirp interference in the range-Doppler domain, where it is filtered at high resolution. This technique has a number of prerequisites, however, all of which are inherently met in SAR applications of appreciable time length.

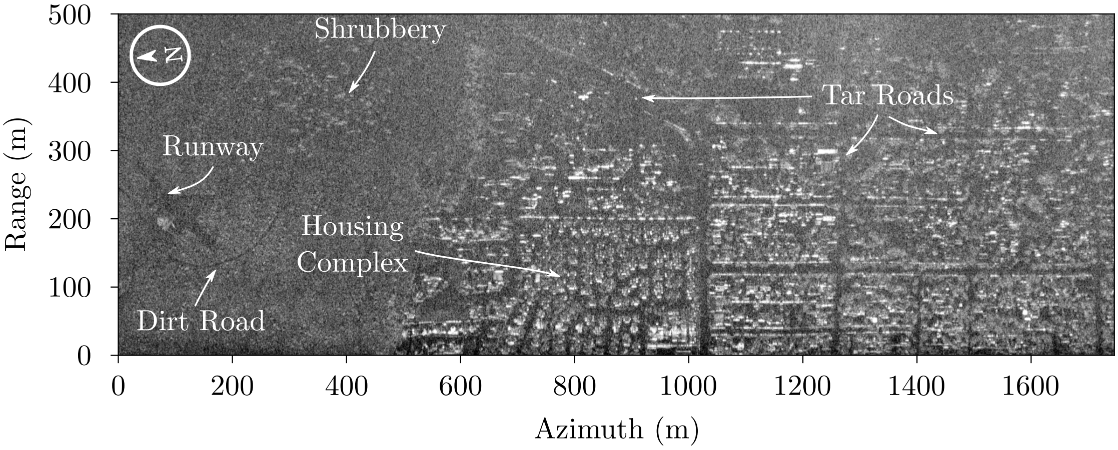

Figure 1.5: SAR image produced using RDSM.

The efficacy of zeroing, loop bandwidth reduction and RDSM are then assessed using simulated SAR data. Despite the resource-limited extent of slow-time, RDSM is found to outperform the other techniques in terms of Root Mean Square Error (RMSE), Structural Similarity Index Measure (SSIM) and Peak Sidelobe Ratio (PSLR) in the azimuth and range domains.

Finally, these techniques are applied to measured SAR data sets, where the results of the simulation are echoed. Figure 1.5 presents an example SAR image produced after the application of RDSM. All three techniques could not, however, be applied to the same measured data set since no campaign to date has consisted of a repeat-pass measurement with variable loop bandwidth. Despite this, the RDSM is demonstrated to outperform the alternatives.

Chapter 6

The thesis is concluded in the final chapter with a summary of answers to the posed research questions, along with recommendations for how these findings may be extended into future research.

The hypothesis is found to be true, as time-offset fractional-N PLLs do offer a low-cost approach for the implementation of heterodyne FMCW SAR. However, additional steps are required to deal with the spur chirps that affect the performance of such a system. It is hoped that this work may aid in promoting the use of fractional-N PLLs for low-cost heterodyne FMCW radar.

Future work may include the implementation of alternative spur suppression techniques, such as the sparse representation techniques used to mitigate mutual interference. Furthermore, the implementation of a variable PLL reference frequency for swept-frequency applications is an enticing prospect.

Chapter 2

Literature Review

2.1 Classic Challenges of FMCW Radar

Feed-through and frequency sweep linearity are appreciated as the classic challenges in FMCW radar design [13, 14].

2.1.1 Feed-Through

Feed-through is a component of the TX signal which unintentionally couples directly into the RX antenna owing to inadequate inter-antenna isolation, as illustrated in Figure 1.1. The negligible propagation path between antennas results in a received signal power which may be orders of magnitude larger than that associated with any target. As a result, feed-through occupies a significant portion of the receiver's dynamic range and limits the receiver's maximum gain, reducing the radar's sensitivity. Of further concern, the feed-through signal's large relative magnitude means that its associated phase noise skirt may exceed the receiver's noise floor and mask signals of interest [15].

Terminology surrounding this phenomenon lacks strict definition. Some of the alternative terms used to describe it include bleed-through, spillover, leakage and cross-talk. In this thesis, the term *feed-through* has been adopted to differentiate it from alternative leakage signals, such as those due to substrate coupling.

The myriad of techniques developed to address the problem of feed-through can be divided in to two distinct categories: preventative and curative. The former aims to prevent the TX signal from entering the receiver at all, typically through physical means, while the latter attempts to mitigate the severity of the feedthrough once it is present in the system. A selection of these techniques are now briefly discussed.

Notched Radiation Pattern

Preventative methods mainly focus on the improvement of inter-antenna isolation. For example, Guo *et al.* [16] demonstrated that TX and RX antenna radiation patterns can be designed to contain a notch in the direction of their counterpart, for use in FMCW SARs.

Antenna Blade

Systems such as the 5N62 square pair FMCW radar make use of a blade (or *knife*) between the TX and RX antennas to increase isolation. In this exceptional case, the blade enables Continuous-Wave (CW) operation at 100 kW, which results in an operational range exceeding 250 km [17].

FMICW

Frequency-Modulated Interrupted Continuous-Wave (FMICW) radars switch between actively transmitting and receiving throughout each frequency sweep, according to an interrupt sequence [18]. This is equivalent to modulating the TX and RX waveforms with anti-phase, syntonised[1] square waves. The drawback of this technique is the induction of spectral replicas at the switching frequency, with sinc magnitude weighting [19]. Both deterministic and random interrupt sequences have been explored to address this [20]. While no longer operating truly continuously, 70 dB to 90 dB of isolation can be achieved with little degradation in system performance [21].

---

[1] Matched in frequency.

Power Cancellation

Alternatively, Leakage Power Cancellation (LPC) and Reflected Power Cancellation (RPC) are curative techniques which eliminate feed-through, antenna reflections and internal leakage through the introduction of an anti-phase cancellation signal. A TX-to-RX isolation of 40.5 dB was achieved by Kim *et al.* [22], using a balanced front-end which comprised only passive components. Venkatamuni *et al.* [23] implemented a digital LPC scheme and reported 25 dB of suppression over 20 MHz of RF bandwidth. Lin *et al.* [5] also developed a digital LPC implementation which achieved 30 dB of feed-through suppression over 1.7 GHz of RF bandwidth.

Analogue Range Gate

Finally, analogue range gating (or Sensitivity Frequency Control (SFC)) is a technique equivalent to Sensitivity Time Control (STC) for pulsed radars. As suggested by its name, an analogue filter is employed to pass only beat frequencies that correspond to a particular range swath [1]. Stringham *et al.* [3] note, however, that the use of high-Q analogue filters near DC results in distortion of the beat spectrum. As such, this technique is reserved for implementation in heterodyne systems, where filtering can take place at an IF. This technique is particularly attractive owing to its comparative simplicity. However, contrary to the aforementioned power cancellation techniques, analogue range gating is unable to combat the phase noise associated with the feed-through signal, since it falls in the frequency band of the video signal [5]. In light of this, alternative methods of addressing the phase noise must be employed in conjunction with range gating. The simplest example of which is coherent integration over a large number of range profiles [13].

2.1.2 Frequency Sweep Linearity

Successful FMCW range processing is critically dependent on the linearity of the frequency sweep [24], defined as

$$L = \frac{3\sigma_f}{k\Delta F}, \tag{2.1}$$

where σ_f is the RMSE of the true ramp frequency compared to an ideal ramp, k is a scaling factor used to account for portions of the bandwidth which are not processed, and ΔF is the RF sweep bandwidth [25].

Non-linearities in the FMCW waveform may degrade range resolution [26], generate spurs in the beat spectrum [27], and decrease SAR image contrast [28]. A brief overview of the three most prevalent FMCW waveform generation methods is now provided.

Open-Loop VCO

The simplest method to generate an FMCW waveform is to drive an RF VCO with a tuning waveform produced by a Digital-to-Analogue Converter (DAC). However, this approach is particularly susceptible to non-linearities in the DAC tuning waveform and/or the VCO frequency response. While numerous hardware [29, 30] and software [31] based techniques have been developed to compensate for the non-linear effects, those techniques typically have the burden of requiring a reference channel or a calibration procedure. As such, open-loop VCO based waveform generation is now largely reserved for low-cost applications where the disadvantages of the non-linearities can be overlooked.

DDS

Alternatively, DDSs may be used to generate high-accuracy, linear chirp waveforms, owing to their accurate and precise control over frequency and phase. Provided that care is taken in managing dispersion through filters, DDSs provide nominally perfect linearity [32]. These devices are fully-integrated and low-cost, but require RF up-conversion and a stable, high-frequency reference oscillator. These additional components may lead to a significant increase in system cost [33].

Fractional-N PLL

Finally, fractional-N PLLs offer an attractive compromise. These devices are inexpensive owing to full integration, and are capable of generating FMCW waveforms directly at RF. The typical costs associated with up-conversion are therefore avoided, and the complexity of the RF sub-system is reduced. Unlike DDSs, the synthesisable RF bandwidth of a fractional-N PLL is not constrained by the reference oscillator frequency, which carries further cost benefits.

Frequency sweep non-linearities due to PLL undershoot and overshoot at the boundaries between ramp segments can be mitigated with the introduction of short ramp segments of constant frequency [34], or entirely removed through time-gating [27]. As will be explained in Section 3.3.1, the loop bandwidth of the PLL must fall between specific limits to ensure a linear transition between the frequency steps that make up the sweep. When these issues are addressed, fractional-N PLLs have been demonstrated to achieve linearity values of $L = 0.01\,\%$ in a 60 GHz FMCW radar with 7 GHz of bandwidth [25].

The aforementioned advantages provide a compelling case for the use of fractional-N PLLs in FMCW SAR, partially addressing the first research question. To fully address the question, the reasoning behind a time-offset pair of these devices must be put forward.

2.2 Receiver Architectures

2.2.1 Homodyne

Traditionally, FMCW radars are implemented with a homodyne receiver architecture. The ubiquity of the homodyne receiver architecture has in fact led certain authors to fail to acknowledge alternative architectures [35]. Also known as *direct-conversion* or *zero-IF*, homodyne receivers translate desired spectral content at RF, directly to baseband. Within an FMCW radar, this is achieved by driving the dechirp mixer's LO port with a coupled portion of the TX waveform, as depicted in Figure 1.1. The simplicity of this architecture enables lightweight, low-cost, and compact system designs; characteristics which have popularised the homodyne

FMCW radar.

These advantageous characteristics, however, come coupled with a number of infamous challenges. Razavi's classic paper on direct-conversion receivers addresses DC offset, LO self-mixing, In-Phase/Quadrature (I/Q) mismatch, even-order distortion and flicker noise [7], phenomena which are well-known to limit the sensitivity of the homodyne FMCW radar [31, 36]. Furthermore, Mayer *et al.* [37] have assessed the impact of non-linearities in the homodyne receiver, illustrating how unintentional receiver saturation produces harmonics and inter-modulation products which contaminate the beat spectrum and produce false targets.

2.2.2 Heterodyne

Heterodyne receiver architectures introduce a fixed frequency offset between the RX and DX signals, which serves to shift the beat spectrum away from baseband to an IF. This frequency offset negates the problems of DC offset and LO self-mixing. The aforementioned issues of flicker noise and I/Q mismatch are also avoided if DDC is employed [8]. Furthermore, the constraints on high-Q filters are relaxed at an IF, which supports the implementation of an analogue range gate.

Relevant case studies of heterodyne FMCW radars are now presented, having been categorised into three classes: AM, offset up-conversion and time offset. This section ends with a tabulated summary of the findings.

Amplitude Modulation

Double-Sideband (DSB) and Single-Sideband (SSB) Suppressed-Carrier (SC) AM have been widely employed to apply a frequency offset to one of the TX, DX or RX waveforms [38]. The following case studies all employ some form of AM, and are organised chronologically according to the signal being modulated.

First, systems which modulate the RX signal are addressed. Saito *et al.* [39] developed a system that employs a High-Electron-Mobility Transistor (HEMT) switch to DSB-SC modulate the RX waveform with a square wave. They report a 20 dB Signal-to-Noise Ratio (SNR) improvement over a comparable homodyne system, which is attributed to the avoidance of Frequency Modulation (FM)-AM conversion noise present at baseband. Their system architecture is presented in

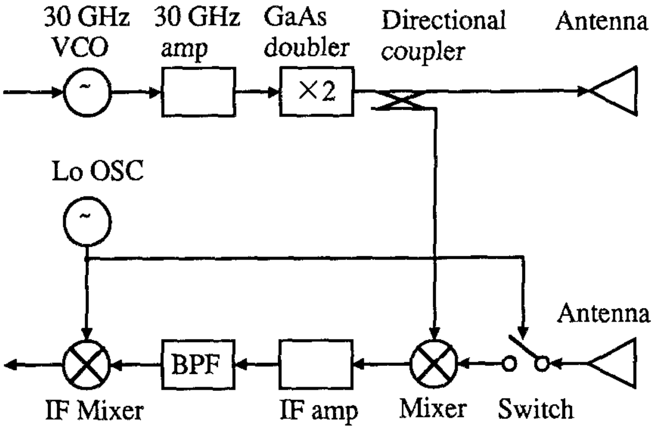

Figure 2.1: Block diagram of the HEMT switch based RX chopper architecture developed by Saito *et al.* [39]

Figure 2.1. Feger *et al.* [40] note that this approach lends itself towards synchronisation with the ADC, serving to avoid the introduction of uncorrelated noise components.

Boukari *et al.* [8] built on the efforts of Saito *et al.*, but used an analogue SSB mixer to introduce a fixed frequency offset between the RX and TX signals. The absence of a redundant sideband leads to a reduction in system cost, since certain filtering requirements are eliminated. The system's bandwidth is, however, limited by the bandwidth of the hybrid coupler within the SSB mixer. Simulation results reveal that their heterodyne implementation offers improved ranging accuracy over a comparable homodyne configuration.

Only one example of an FMCW radar which modulates the DX signal could be found in the literature. Stringham *et al.* [3] implement what they term an *offset IF homodyne receiver* by frequency shifting the DX waveform used for dechirp. The brute-force, filtering method of SSB modulation is employed through analogue mixing and filtering. A block diagram of the system is presented in Figure 2.2.

Finally, systems which modulate the TX signal are explored. Charvat's seminal book [1] describes a heterodyne system intended for demonstrating the applicability of an analogue range gate. DSB-SC modulation of the transmit signal necessitates an analogue filter, which serves the dual purpose of a range gate and suppressing unwanted mixing products. The use of an open-loop VCO for wave-

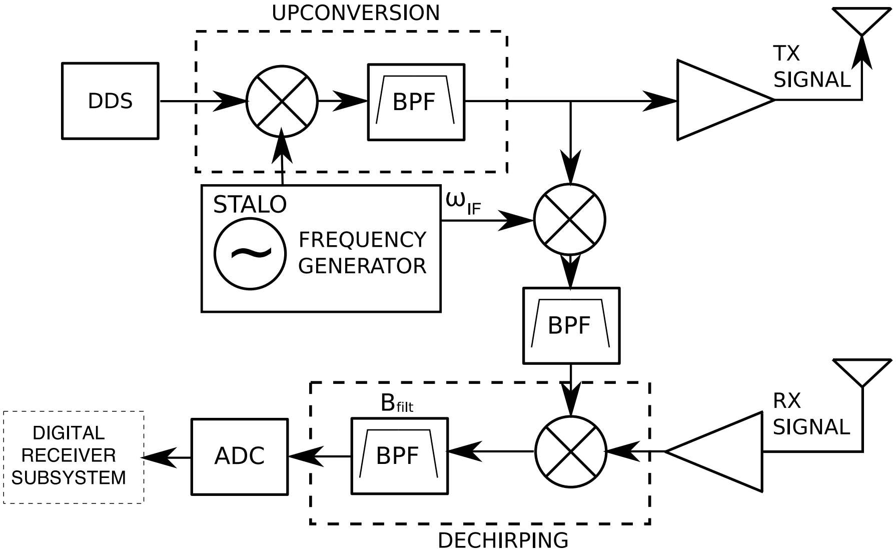

Figure 2.2: Block diagram of the offset IF homodyne receiver design developed by Stringham *et al.* [3], which employs DX waveform modulation.

form generation is a cause for concern, as a notorious source of non-linearity in the FMCW waveform. The beat spectrum is down-converted from IF using analogue mixers prior to digitisation, missing an opportunity to avoid flicker noise. Figure 2.3 presents a block diagram of the system architecture.

While also applying DSB-SC modulation to the TX waveform, Anghel *et al.* [31] extended Charvat's design in two respects. Firstly, a digital non-linearity correction algorithm, based on the reference response from a delay line, was shown to dramatically improve ranging performance. Secondly, down-conversion was performed digitally after filtering. This approach required a secondary ADC channel, however, such that the non-coherent IF frequency could be sampled.

Alternatively, Feger *et al.* [38] used an I/Q modulator in the radar's TX path to implement an SSB mixer. This way, the TX signal can be shifted to realise a frequency offset with respect to the RX, without superfluous sidebands. The IF is therefore digitally adjustable and synchronous with the ADC. This approach avoids the additional phase noise introduced in multiple VCO based implementations. Figure 2.4 illustrates the developed transceiver.

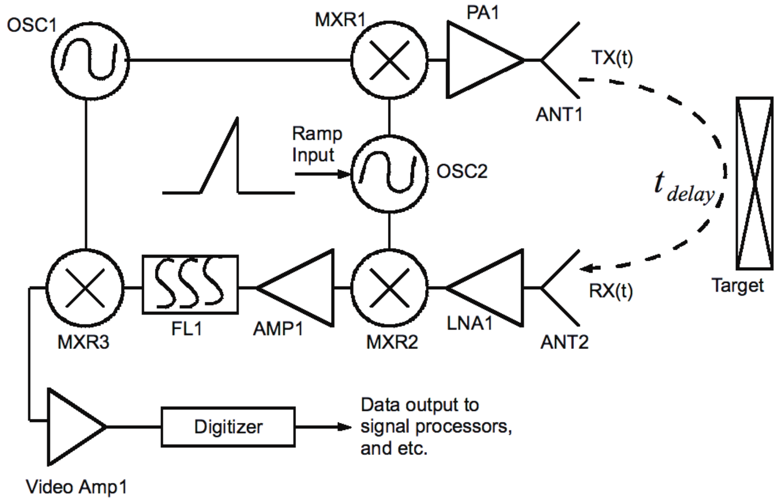

Figure 2.3: Block diagram of Charvat's [1] FMCW radar architecture, which applies DSB-SC AM to the TX waveform and features an analogue range gate.

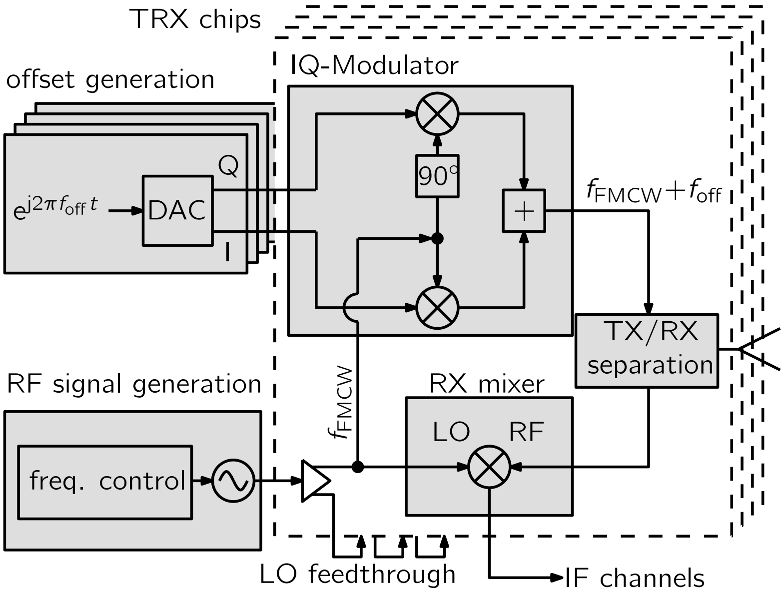

Figure 2.4: Block diagram of the heterodyne transceiver developed by Feger *et al.* [38] I/Q modulation is used to implement an SSB mixer in the TX path.

Offset Up-conversion

Contrary to the AM techniques explored before, offset up-conversion is based on the use of frequency multipliers and PLLs to up-convert TX and DX signals by differing factors to achieve a frequency offset. The case studies that follow are presented in chronological order.

The SlimSAR, designed by Zaugg *et al.* [10, 41–43], is novel in its utilisation of a pair of DDSs for waveform synthesis. In what they term a *delayed mix-down chirp*, the otherwise identical waveforms generated by the DDSs are offset in time. The system's IF is coarsely set by a difference in the up-conversion factor applied to each DDS's output and then fine-tuned thorough digital adjustment of the time offset. Digital control over the IF enables a reduction in wasted bandwidth in their high chirp rate, SAR application. This way, the radar's detection range is extended.

Feger *et al.* [44] developed a heterodyne FMCW radar based on two frequency-offset PLLs for up-conversion. Rather than using high divider values, mixers are used for down-conversion within the PLL feedback paths to avoid deterioration of phase noise performance. The same radar is capable of simultaneous homodyne and heterodyne operation, and includes a reference channel used to compensate for temperature variations which influence the reference frequency. They demonstrate that the TX and DX waveforms generated by independent VCOs are partially correlated, but subtraction of the reference channel serves to eliminate residual uncorrelated phase noise. In their approach, the value of the IF is limited to integer multiples of the reference frequency.

Dao *et al.* [45] produced a heterodyne radar which uses a single DDS and two separate up-conversion chains to introduce a frequency offset between the TX and DX signals. A reference channel is employed for demodulation, and is demonstrated to significantly reduce phase noise associated with uncorrelated VCOs. I/Q sampling is performed at baseband after analogue demodulation, which introduces the problems of I/Q mismatch and flicker noise. A block diagram of the system is presented in Figure 2.5.

More recently, Suh *et al.* [46] developed a Ku-band radar with two IF stages. The system makes use of three PLLs, three mixing stages and several frequency

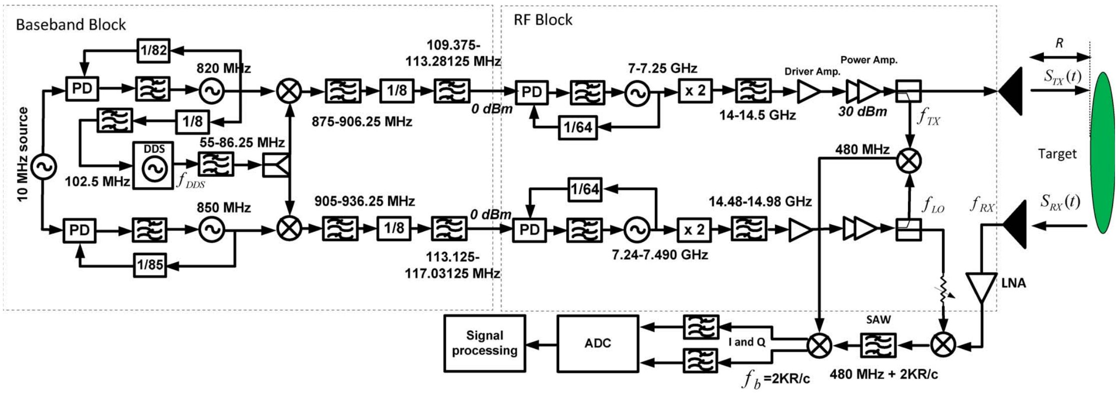

Figure 2.5: Block diagram of the offset up-conversion heterodyne architecture developed by Dao *et al.* [45] The TX and DX waveforms are mixed in a reference channel, which is used for I/Q demodulation.

dividers and multipliers, which results in a relatively complex system architecture. The implication of uncorrelated VCO phase noise is not addressed by the authors, but may not present a significant problem owing to the 10 m displacement between the TX and RX antennas using 75 Ω coaxial cables.

Time Offset

The introduction of a time offset between the DX and RX signals maps to a proportional deviation in beat frequency. This fundamental property of FMCW radars is manipulated in the following case studies to adjust the IF of the beat spectrum. The case studies have been categorised according to which signal is delayed.

Delaying the DX with respect to the TX signal serves to reduce the dechirped beat frequency. Hamran *et al.* [19] describe an FMICW SAR. The inherent displacement between the radar platform and first target in SAR, means that the peak of the sinc weighting function is shifted to an appreciable IF. To recover the specific replica within the sinc's mainlobe, they employ an analogue delay line matched to the propagation time of the ground return. This way, receiver bandwidth requirements are reduced and the magnitude of the beat spectrum is not suppressed.

In a wall-penetrating application, Kim *et al.* [47] describe and simulate how

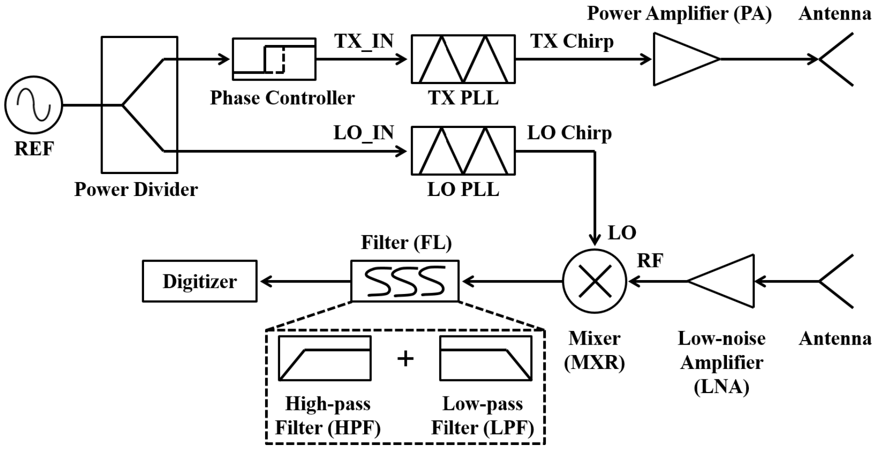

Figure 2.6: Time-offset heterodyne architecture developed by Kim *et al.* [11] A phase controller is used to advance the TX PLL with respect to the DX.

the order of a HPF, used for analogue range gating, can be reduced by lowering the beat frequency associated with short-range clutter. In later developments Kim *et al.* [11] demonstrate the technique using a pair of time-offset PLLs. Seen in Figure 2.6, their implementation requires a phase controller to advance the TX PLL's reference signal by a half-period for each time step.

Only one instance of an FMCW radar which delays its TX waveform with respect to the DX was found in the literature: a wide-range altimeter system developed by Choi *et al.* [48, 49]. As seen in Figure 2.7, this system employs an optical delay line module which converts electrical signals to optical and vice versa. This provides a fixed time offset which serves to increase the IF frequency, such that a BPF can be used to suppress feed-through. The system's chirp rate is varied as a function of altitude. At lower altitudes, the chirp rate is increased and suppression is improved at the cost of reduced range (which is irrelevant in this application). While at higher altitudes the chirp rate can be reduced to increase detection range, while maintaining an acceptable level of suppression owing to the greater displacement between ground and radar.

A gap in the literature therefore exists for the implementation of a heterodyne FMCW SAR that relies solely on a variable time delay of its TX waveform with respect to its DX. If implemented using fractional-N PLLs, the resultant system would be comparatively cheaper and simpler than the SlimSAR, while still

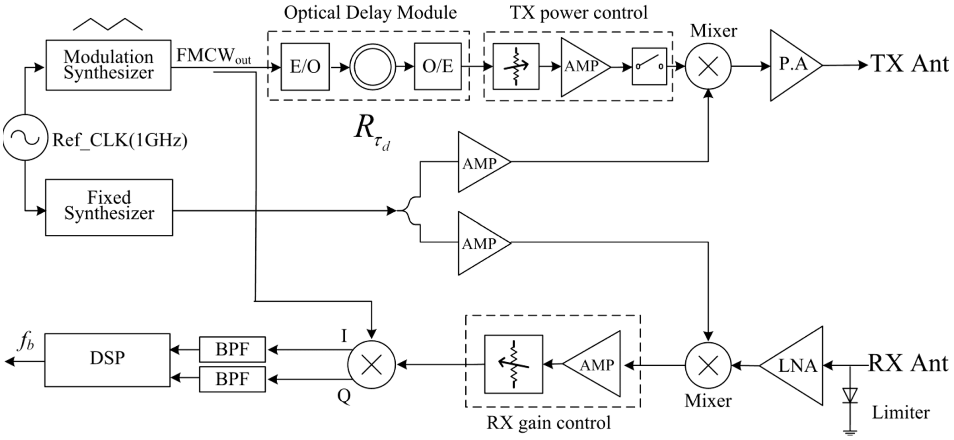

Figure 2.7: Block diagram of the time-offset heterodyne architecture developed by Choi *et al.* [49] An optical delay module is used to delay the TX waveform with respect to the DX.

enabling bandwidth recovery at variable altitudes. Furthermore, such a system would eliminate the need for a phase controller as used by Kim *et al.* This serves to address the first research question.

Summary

Table 2.1 presents a convenient summary of the heterodyne receiver implementations which were reviewed in the preceding sections.

The table reveals that the number of systems that utilise DDS for waveform synthesis dwarf those that use fractional-N PLLs. Furthermore, a move away from open-loop VCOs, and towards DDSs is suggested by the publications. Likewise, a shift away from AM based heterodyne architectures can be observed.

2.3 Fractional-N PLL Spurs

Fractional-N PLLs are notorious for producing undesirable spurious products in their output [50]. As such, the literature contains several works analysing the source of these spurs and presents techniques to suppress them [50–58]. However, these works largely target clock generation applications for communications systems, where synthesis of specific, individual tones is desired. The impact of these

Table 2.1: Summary of FMCW Heterodyne Receiver Implementations

Heterodyne Implementation	Ref.	Year	Waveform Synthesis	Description
(RX) DSB-SC AM	[39]	1992	VCO	20 dB SNR improvement over homodyne counterpart.
(RX) SSB-SC AM	[8]	2009	VCO	Improved range accuracy over homodyne counterpart.
(DX) SSB-SC AM	[3]	2011	DDS	Feed-through suppressed with high-Q BPF at high IF.
(TX) DSB-SC AM	[1]	2014	VCO	Low-cost high-Q BPF at low IF.
(TX) DSB-SC AM	[31]	2014	VCO	Digital non-linearity correction and DDC.
(TX) I/Q Modulation	[38]	2011	DDS	Avoids uncorrelated phase noise due to multiple VCOs.
Offset Up-Conversion	[10]	2010	DDS	Combine time and frequency offsets to recover bandwidth.
	[44]	2011	DDS	Mixers in PLL feedback path reduce phase noise.
	[45]	2013	DDS	Reference channel based demodulation reduces phase noise.
	[46]	2017	DDS	Uncorrelated phase noise not addressed.
(DX) Time Offset	[19]	2008	DDS	Fixed time offset recovers losses due to FMICW.
	[11]	2017	PLL	Phased controller enables clutter attenuation using HPF.
(TX) Time Offset	[49]	2015	DDS	Optical delay line for improved altimeter ranging.

spurs on heterodyne FMCW SAR performance, where a swept frequency waveform is required, has not received adequate analysis in the literature.

In the context of FMCW radar, spurs which manifest within the RF sweep bandwidth are of particular concern. Moreover, the subset of those spurs whose frequency offset is a function of the carrier frequency, present a unique challenge to FMCW radars. To the best of the author's knowledge this unique challenge has not been addressed in the literature. An overview of the spurs associated with fractional-N PLLs is now presented.

2.3.1 Fractional Spurs

Primary fractional spurs appear at an offset equal to the PLL channel spacing, $f_{\text{channel}} = f_{\text{PD}}/F_{\text{d}}$, while sub-fractional spurs occur at fractions thereof, i.e. f_{channel}/h where $h \in \{2, 3, ...\}$. Here, f_{PD} is the PLL phase detector frequency and F_{d} is the fractional denominator. These spurs are the result of periodicity in the feedback modulation sequence, which can be addressed through randomisation through dithering and/or use of large equivalent fractions [59]. To this end, many commercially-available fractional-N PLLs enforce their maximum fractional denominator value when frequency sweeping functionality is requested, thus maximising the equivalent fraction. These techniques effectively spread the primary fractional and sub-fractional spur power into noise.

In a recent publication, Grimaldi *et al.* [60] analysed the impact of fractional spurs on the performance of FMCW radar systems. They state that the impact of spurs in the PLL output spectrum of FMCW radars had not previously been addressed in the literature. Their results show that under certain conditions, fractional spurs can increase the noise floor of the range profile. The authors also assessed the impact of spurs that originate from signal coupling to the PLL output buffer and oscillator. These additional spurs were found to generate ghost targets and raise the noise floor.

Wu *et al.* [61] developed a fractional-N All-Digital Phase-Locked Loop (ADPLL) for FMCW radar applications with fractional spur levels below $-62\,\text{dBc}$. They state that because their in-band fractional spurs are masked by phase noise, are attenuated at offsets exceeding the PLL loop bandwidth, and only appear at any particular frequency for a short time (several reference frequency cycles), they do not pose a problem. Even with their significantly higher fractional spur levels of $-40\,\mathrm{dBc}$, Lee *et al.* [62] concur with Wu *et al.*, stating that fractional spurs have little influence on radar performance since they change continuously.

2.3.2 Integer Boundary Spurs

IBS are modulated spurs[2] which appear at an offset (f_{IBS}) equal to the instantaneous difference between the VCO frequency (f_{VCO}) and nearest integer multiple of the phase detector frequency [59]. This offset simplifies to

$$f_{\mathrm{IBS}} = f_{\mathrm{PD}} \left[n\frac{F_{\mathrm{n}}}{F_{\mathrm{d}}} - \mathrm{NINT}\left(n\frac{F_{\mathrm{n}}}{F_{\mathrm{d}}} \right) \right], \tag{2.2}$$

where n is a natural number, F_{n} is the fractional numerator and NINT rounds to the nearest integer value [51].

Owing to substrate coupling [53], both f_{VCO} and f_{PD} are simultaneously present at the non-linear phase detector [50], as illustrated in Figure 2.8. Here, these non-harmonically related signals mix and alias to produce IBS [51]. IBS are attenuated outside the PLL loop bandwidth, and are therefore of most concern near integer multiples of f_{PD}. If the RF sweep bandwidth is larger than f_{PD}, IBS will transition in and out of the PLL loop filter on multiple occasions during each sweep. To the best of the author's knowledge, the effect of IBS on heterodyne FMCW SAR has not been analysed in the literature.

Note that several names have been given to these spurs in the literature, including *substrate spurs* and *intermodulation spurs*. In this thesis, these spurs are termed IBS.

---

[2] Spurs that modulate the PLL VCO or output buffer and occur in pairs, at equal amplitude and offset from the carrier.

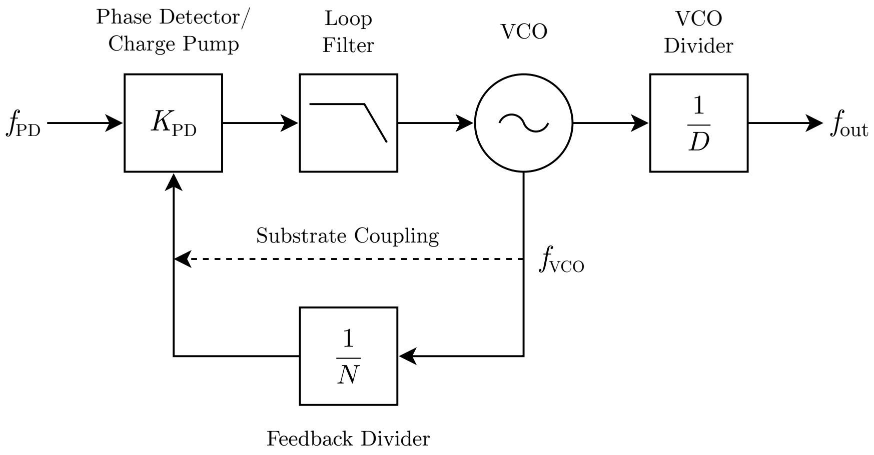

Figure 2.8: Block diagram of a generic fractional-N PLL [12], where fractional mechanisms have been neglected.

2.3.3 Phase Detector Harmonics

Typically the result of charge-pump noise leaking onto the ground plane through a supply pin [59], PDH are direct spurs[3] which manifest at frequencies of

$$f_{\text{PDH}} = h f_{\text{PD}}, \qquad h = 2, 3, ..., m. \tag{2.3}$$

As such, they appear at fixed frequencies in a frequency-time spectrogram. If the RF sweep bandwidth of an FMCW radar is larger than the phase detector frequency (usually the case), several PDHs may appear within the the radar's bandwidth.

The offset of PDH from the sweeping carrier frequency is not constant. The impact of this will be analysed later in this thesis. To the best of the author's knowledge, their exists no prior work analysing the impact of PDH on FMCW SAR performance.

2.3.4 Sweep Non-Linearity Induced Spurs

Piper [26] simulated the effect of sinusoidal non-linearities in the frequency sweep of a homodyne FMCW radar. His simulations showed that in addition to degradation

---

[3] Direct spurs appear in PLL output without modulating the VCO or output buffer.

of range resolution, spurious signals may be produced.

Higuchi *et al.* [63] addressed spurs which are generated as a result of the uniform step size in the staircase-like frequency control word function which is used for producing FMCW waveforms. This is similar to the non-linearity problem described by Piper. They note that the typical loop bandwidth optimisation approach to improve linearity [25] is not appropriate when both slow and fast modulation is required. Instead, they reduce periodicity of the frequency control word function and measure a 13.6 dB reduction in the spur's power level. It is noted that their technique severely disturbs the radar's noise floor flatness and was only tested within a homodyne configuration. A suggested alternative approach may be to adjust the loop bandwidth dynamically using the CPG, such that loop bandwidth could be optimised for both fast and slow modulations.

Weyer *et al.* [27] also tackle the problem of spurs generated as a result of frequency sweep non-linearities. Unlike Higuchi *et al.*, however, they rely on loop bandwidth optimisation to eliminate these spurs. They report an impressive SFDR of approximately 95 dB, demonstrating that these spurs need not hinder the radar's performance.

2.4 Conclusions

A review of the literature surrounding heterodyne FMCW radar has been presented, intended to provide the reader with a foundation of knowledge upon which subsequent chapters will build.

Analysis of the classic challenges for FMCW radar revealed that feed-through (and its associated phase noise) severely limit the sensitivity of these sensors. Analogue range gating was found to offer the simplest method of feed-through suppression for heterodyne systems, but required a supplementary method of phase noise suppression. One such method was identified as coherent integration. Since SAR inherently performs a large degree of coherent integration during azimuth compression, analogue range gating is a viable option for SAR applications.

Both DDSs and fractional-N PLLs were identified as linear waveform synthesisers for FMCW radar. However, a review of heterodyne receiver architectures revealed a large disparity in the implementation rate of these devices, with far more radars opting to use DDS. This is interesting, as the low cost associated with fractional-N PLLs make them a particularly attractive option. A gap in the literature was identified for the implementation of a heterodyne FMCW SAR based on time-offset fractional-N PLLs.

The low implementation rate of fractional-N PLLs for FMCW radar is likely owed to the undesirable spurs produced by these devices. Specifically, it was found that the effects of PDH and IBS on FMCW SAR performance has not been assessed in the literature, representing an additional gap.

To address both of the identified gaps in the literature, the next chapter describes the implementation of the miloSAR: a heterodyne FMCW SAR based on time-offset fractional-N PLLs. Initial measurements with the system reveal that spurious content has a significantly detrimental effect on the resultant SAR imagery.

Chapter 3

Overview of the miloSAR

This chapter presents an overview of the miloSAR: the only known implementation of a fully polarimetric, heterodyne FMCW SAR which employs a pair of time-offset fractional-N PLLs for waveform synthesis. The purpose of this overview is to provide the reader with background on the system's functionality, upon which later chapters will build. Specifically, the overview provides context for the problem of *spur chirps*; an integral aspect of this thesis. To this end, the overview details important hardware and gateware, compares the time- and frequency-offset approaches to heterodyning, presents the results of system characterisation, and assesses the system's ability to produce SAR imagery. Aspects of this chapter are based upon the following publication:

D. A. Jordan, P. Cheng, M. R. Inggs, A. Langman and M. Y. Abdul Gaffar, "Development of the miloSAR testbed for the one kilogramme radioCamera SAR for small drones," in *Proc. IEEE Radar Conf. (RadarConf)*, Apr. 2019, pp. 1–6, doi: 10.1109/RADAR.2019.8835721 (Presented).

3.1 Introduction

The author inherited the bulk of the miloSAR's hardware from Tchekashkin [9] in 2016. At that time, the system operated non-coherently, featured a single polarisation and was limited to measurement lengths of under 8.59 s. Despite the system's intended application of low-cost imaging for small drones, it was clearly incapable of SAR operation at that stage. As such, the system required a partial redesign, characterisation and calibration before its implementation as a SAR. For reference, Figure 3.1 presents a comparison of the radar's internals before and after the author's contribution.

A number of the hardware upgrades made by the author during the course of the project can be seen in Figure 3.1. These include, but are not limited to the following.

1. Replaced the Alternating Current (AC)-DC rectifier with a DC-DC converter to enable SAR experiments using 12 V batteries.
2. Rewired all components to avoid ground loops. 5 V and 12 V supply wires were colour coded for clarity.
3. Added 5 V linear regulators for PLL power supplies to avoid VCO spurs due to switching in the DC-DC converter.
4. Extracted the 125 MHz clock from the STEMlab for use as the PLL phase detector reference signal.
5. Installed of a fan for the STEMlab to limit temperature related clock drift.
6. Enabled PLL programming using the STEMlab over a ribbon cable, which eliminated the need for a USB2ANY module.
7. Added a Real-Time Kinematic (RTK) Global Navigation Satellite System (GNSS) module, with trigger pulses to log the beginning and end of experiments.
8. Installed an RF switch to enable changing of the transmit polarisation.

These upgrades, along with the implementation of time-offset heterodyning, enabled the radar's receiver architecture to be converted from a single receive channel (plus a reference channel), into two receiver channels. As such, the system was upgraded from single polarisation operation, to offer quad polarisation capabilities. This can be seen in the system level block diagram presented in Figure 3.2. Subsequent chapters assess the subsystems of this diagram in more detail.

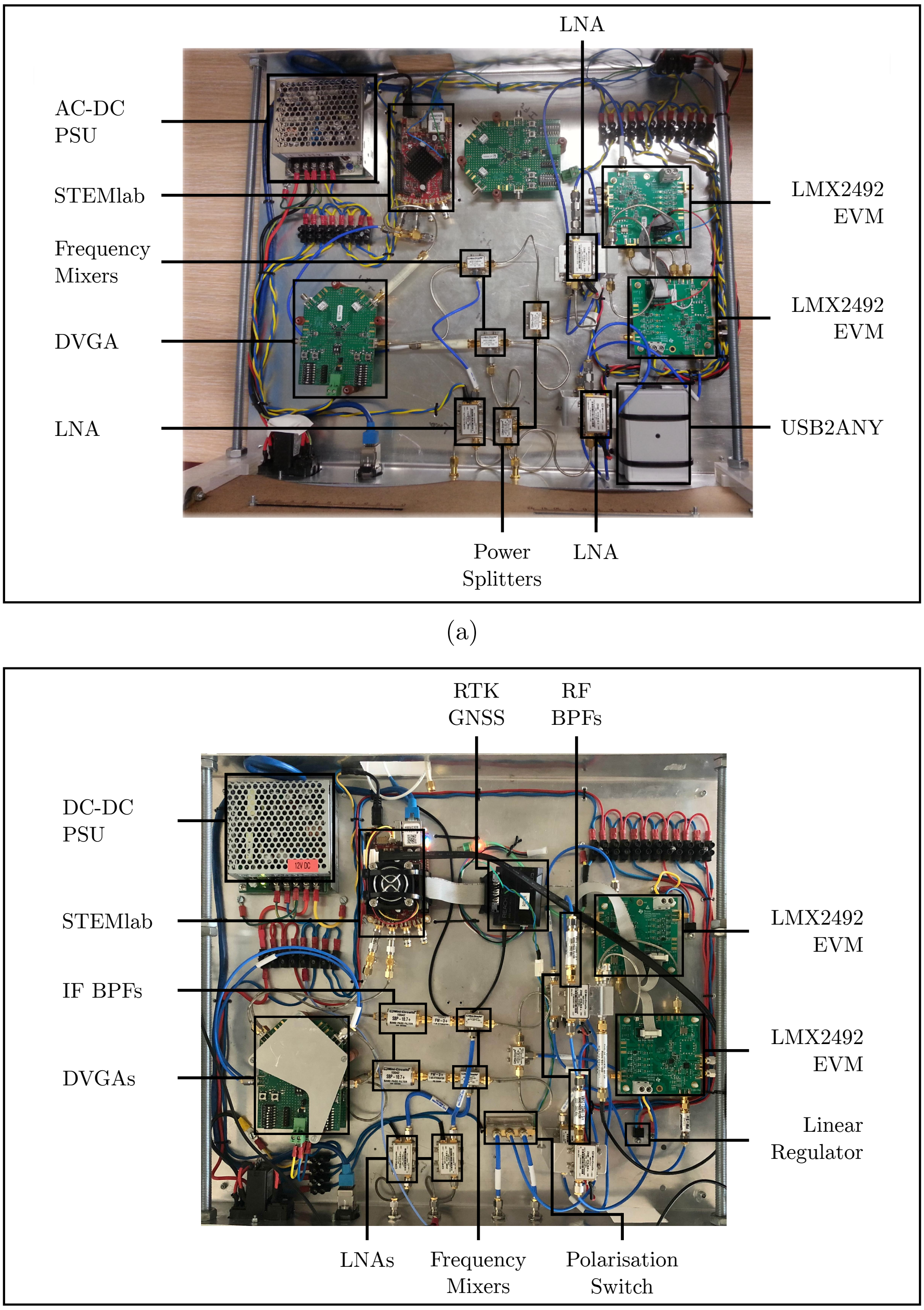

(a)

(b)

Figure 3.1: Comparison of the miloSAR's internals (a) before and (b) after the author's involvement. (a) was adapted from [9].

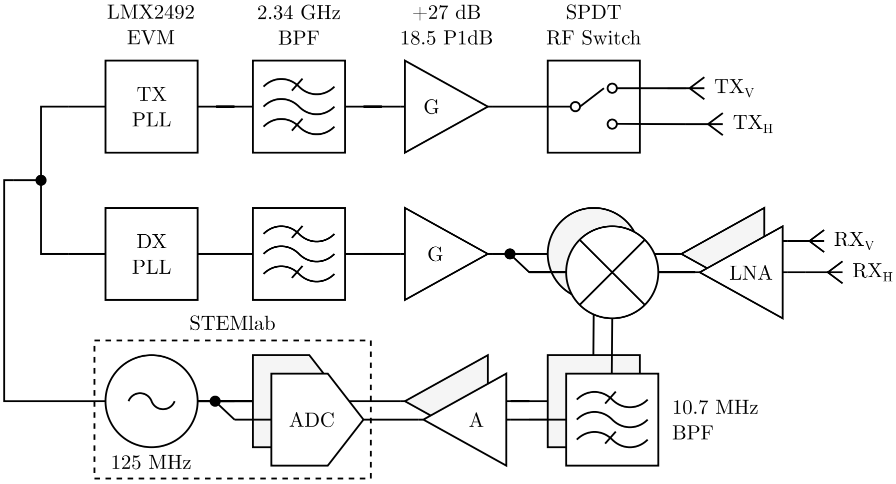

Figure 3.2: Block diagram of the miloSAR [12]. Fully polarimetric operation was enabled by the single-pole double-throw RF switch in the TX chain, in combination with the two RX channels.

3.2 STEMlab

A STEMlab 125-14 (previously known as Red Pitaya) serves as the system's control centre, digital receiver and reference clock source [64]. The STEMlab features a Xilinx Zynq 7010 System-On-Chip (SoC), which combines a dual-core Advanced RISC Machine (ARM) processor and an FPGA. Furthermore, it has two 14 bit ADC channels which capture samples at 125 MHz. This sample rate supports the implementation of an oversampled digital receiver, where digital polyphase filters can be used to reduce quantisation noise and increase each sample's Effective Number of Bits (ENOB) [3]. A simplified block diagram of the STEMlab's internals is presented in Figure 3.3.

3.2.1 Reference Clock

The STEMlab's internal Crystal Oscillator (XO) serves as the radar's master clock source. This oscillator produces a differential square wave at 125 MHz, which passes through the on-board LTC2145 ADC before entering the Zynq. From the FPGA, the differential clock is exposed to one of the STEMlab's Serial at Attachment (SATA) ports, from which it is split for distribution as the phase detector

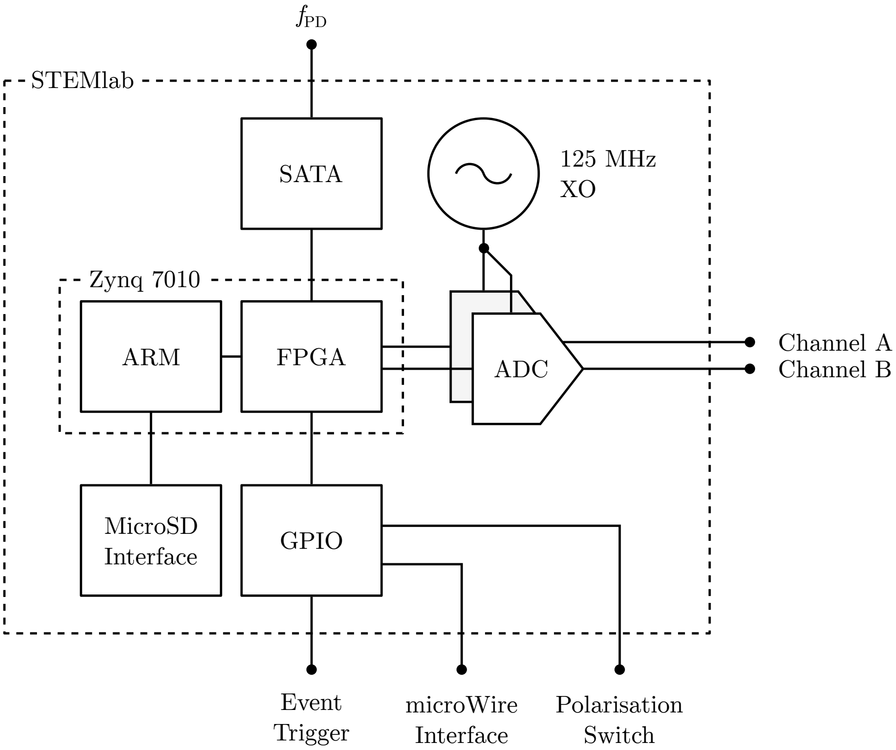

Figure 3.3: Simplified block diagram of the STEMlab's internals.

frequency (f_{PD}) for each fractional-N PLL synthesiser. The miloSAR's PLLs, ADCs and FPGA therefore all share the same reference clock, serving to syntonise signal generation, sampling and processing. The power spectrum of the 125 MHz reference signal is illustrated in Figure 3.4.

The power spectrum of the square wave reference signal in Figure 3.4 has already passed through a VLFX-105 Low-Pass Filter (LPF), intended to smooth the square wave by suppressing its odd harmonics. The VLFX-105 has a 3 dB cut-off frequency of 165 MHz, which leads to marginal attenuation of the reference signal. The reference signal's power level was measured using a Spectrum Analyser (SA) to be -0.5 dBm within a RBW of 1 kHz, which is sufficient to drive the phase detector circuitry of each PLL.

At an offset of 1.5 MHz the noise floor was measured to be -121.6 dBm/Hz. Undesirable spurii are clearly present at significant offsets from the carrier. The frequency offsets and magnitudes of the first ten spurs (relative to the carrier) are summarised in Table 3.1.

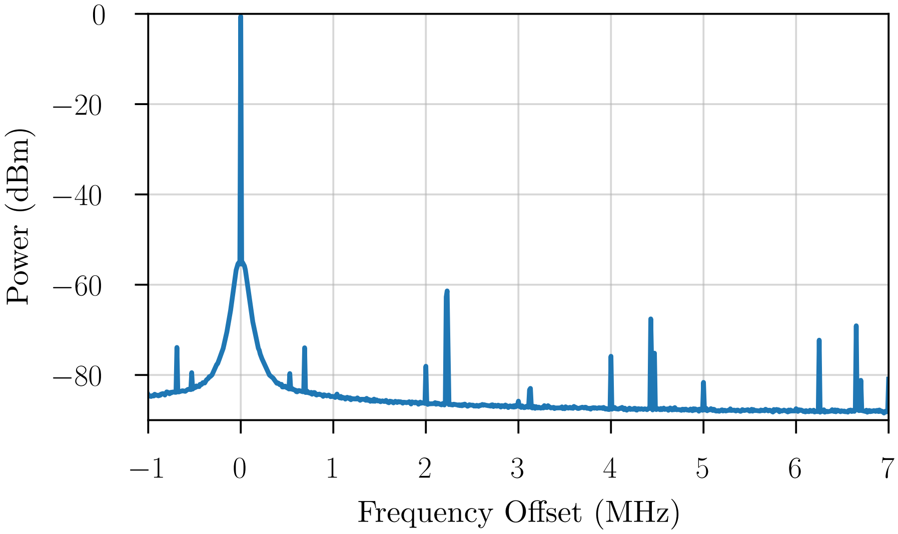

Figure 3.4: Power spectrum of the reference signal, measured with a Resolution Bandwidth (RBW) of 1 kHz. Spurious signals are clearly present at significant offsets from the 125 MHz carrier.

Table 3.1: First Ten Reference Signal Spurs

Offset (MHz)	0.53	0.69	2.00	2.23	3.13	4.00	4.43	4.47	5.00	6.25
Power (dBc)	−80	−74	−78	−62	−83	−76	−67	−75	−82	−72

3.2.2 Gateware

The default gateware that ships with the STEMlab is very useful for generic applications, but was not optimised for the miloSAR's requirements. The main limitation being an inability to sustain continuous sampling for an appreciable experiment period. This is partly due to the microSD card interface, which is only accessible via the ARM processor. Data processed in the FPGA must therefore be passed to the ARM, using shared memory mapping, for storage on the microSD card. Under the default gateware, a maximum continuous experiment length of 8.59 s could be achieved at the minimum supported sampling rate of 1.907 kHz. This was clearly unacceptable for SAR applications, and prompted the development of custom gateware for the FPGA, including a DDC, profile integrator and TCU. Using work done by Barris [65] as a foundation, a maximum storage Data Rate (DR) of 10 MB/s was achieved for indefinite recording periods.

Digital Down-Converter

Each STEMlab ADC channel delivers signed, 14 bit samples at 125 MHz. The DDC was responsible for translating a select, narrow region of each channel's sampled 62.5 MHz of bandwidth down to baseband. Specifically, the DDC was required to extract frequency components that fell within the 3 dB bandwidth of the receiver's IF BPF. This was achieved through multiplication with a complex sinusoid, at a configurable LO, followed by digital filtering. DR limitations, however, meant that only 3.125 MHz of the IF filter's 3.8 MHz of bandwidth could be extracted for storage.

Each complex LO is generated with an independent Xilinx DDS Intellectual Property (IP) core. The DDS frequency is specified with a 32 bit phase increment value, which provides a frequency resolution of 0.029 Hz. Furthermore, Taylor series corrected noise shaping and an output width of 19 bit meant that each DDS has a theoretical SFDR of 108 dB. Because each channel makes use of its own DDS, the LO applied to each channel can differ. Additionally, the phase of each DDS is purposefully reset at the beginning of each Pulse Repetition Interval (PRI) to avoid the introduction of an undesirable phase offset.

Each channel's 14 bit ADC samples are multiplied with the synthesised 19 bit sine and cosine LO components, to produce 33 bit I/Q output samples. The I/Q samples for both channels are then concatenated and fed into two Finite Impulse Response (FIR) LPF stages.

The main objective of the first filter stage was to decrease the effective sample rate through decimation, such that a reduced number of taps was required to implement a high-order LPF in the second stage. To this end, a poly-phase FIR filter with a Decimation Factor (DF) of 20 was configured using the Xilinx FIR compiler. This reduced the sample rate to $f_{\mathrm{PD}}/20 = 6.25\,\mathrm{MHz}$. Figure 3.5 illustrates the frequency response of the 145-tap first stage filter, featuring a cut-off frequency of 2.75 MHz and 120 dB of attenuation extending from 6 MHz. Additionally, the filter applied convergent rounding (opposed to simple Least-Significant Bit (LSB) truncation) to reduce the unwieldy bit width of each I/Q sample down to 16 bit, meaning that each complex sample was represented with 4 bytes. The use of convergent rounding avoided the introduction of a spurious DC term caused by LSB

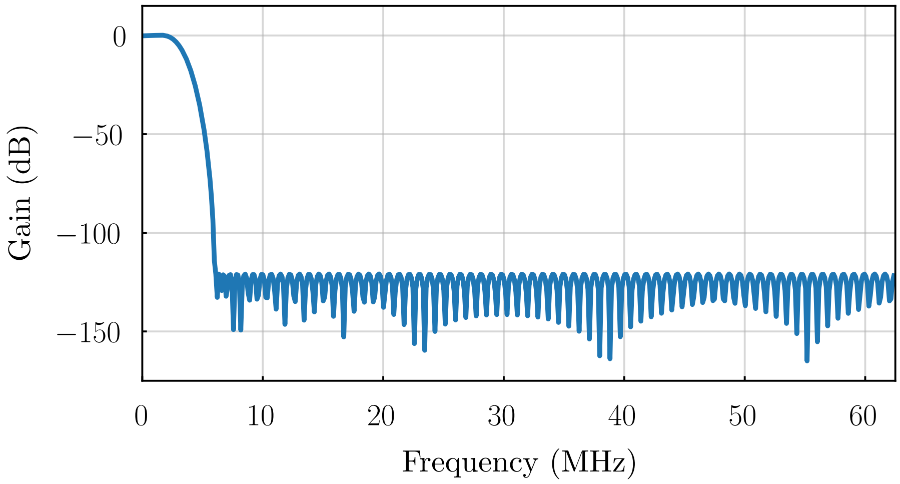

Figure 3.5: Frequency response of the first-stage 145-tap poly-phase FIR filter in the DDC, with 0.34 dB ripple over the 2 MHz passband.

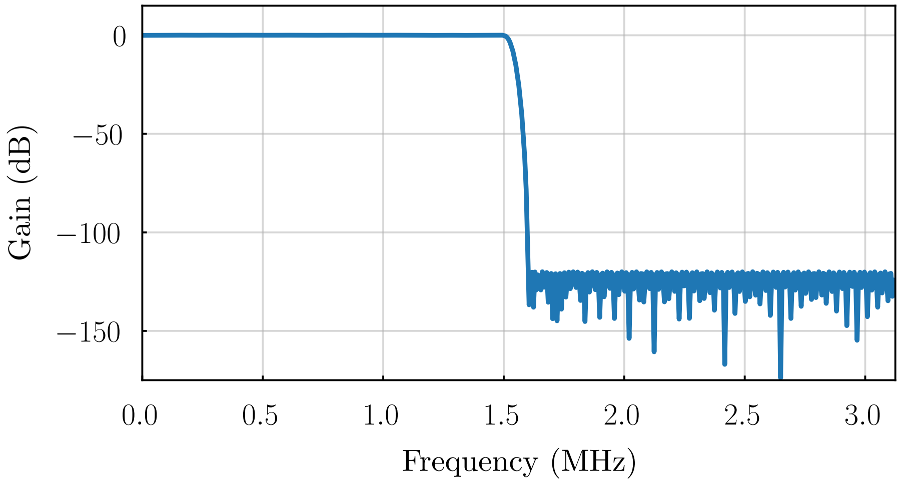

Figure 3.6: Frequency response of the second-stage 291-tap poly-phase FIR filter in the DDC, with a 1.5 MHz passband and 120 dB of attenuation in the stop-band.

truncation.

The second stage poly-phase FIR filter, presented in Figure 3.6, was designed for a flat passband and steep roll-off. The 291-tap filter features a 1.5 MHz passband and 120 dB of attenuation in the stop-band extending from 1.6 MHz. This stage also enforced a DF of 2, such that the receivers combined DF was 40 and the system's effective baseband sample rate was $f_\mathrm{s} = f_\mathrm{PD}/\mathrm{DF} = 3.125\,\mathrm{MHz}$.

At this sample rate, the storage DR required for 2 receiver channels (where each sample required 4 bytes) can be calculated as

$$\mathrm{DR} = 2\left(4\,\frac{f_{\mathrm{PD}}}{\mathrm{DF}}\right) = 25\,\mathrm{MB/s}. \tag{3.1}$$

This is 2.5 times greater than the maximum supported DR. As such, additional techniques were required to reduce the DR.

Profile Integrator

After the DDC, the baseband samples proceed to the profile integrator, which performs pre-summing and sample chopping. Pre-summing is the process of coherently adding consecutive profiles together, serving to improve SNR and provide a variable reduction in Pulse Repetition Frequency (PRF) and thus the DR. The samples captured within each PRI are loaded into a First-In First-Out (FIFO) buffer for temporary storage. A configurable number of subsequent profiles are then summed with the buffered samples. The effective PRF ($\mathrm{PRF_e}$) is then simply the original PRF, reduced by the pre-sum factor PF,

$$\mathrm{PRF_e} = \mathrm{PRF}/\mathrm{PF}. \tag{3.2}$$

Following pre-summing, the profiles are *chopped* such that only samples corresponding to the up-ramp portion of the filtered beat signal are selected for storage. This reduces the required storage DR once more. Conveniently, the sample chopper can be used to account for the group delay of the two FIR filter stages.

Combination of a 50 % chop factor (CF) and a PF of 2 was used to reduce the DR to an acceptable value,

$$\mathrm{DR} = 2\left(4\,\frac{f_{\mathrm{PD}}}{\mathrm{DF}}\right)\frac{\mathrm{CF}}{\mathrm{PF}} = 6.25\,\mathrm{MB/s}. \tag{3.3}$$

While alternative combinations of CF and PF will satisfy the DR constraint of 10 MB/s, these values were most commonly used in practice.

Timing Control Unit

The TCU was responsible for generating the system's reference PRF square wave, two polarisation control signals and an event trigger for start-stop control of peripherals.

The miloSAR is limited to PRF values which are integer divisors of the reference frequency. Generating the PRF square wave is therefore a matter of counting FPGA clock cycles and toggling a flag when appropriate. The number of clock cycles per PRI (C) is simply

$$C = f_{\mathrm{PD}}/\mathrm{PRF}, \qquad C \in \mathbb{N}. \tag{3.4}$$

In addition to setting the PRF, the selected value of C constrains the set of supported DFs, because each PRI must contain an integer number of samples (P) following decimation.

$$P = C/\mathrm{DF}, \qquad P \in \mathbb{N}. \tag{3.5}$$

The absorptive switch employed to vary the transmit polarisation makes use of two control signals to set its state. In addition to multiplexing between two signal inputs, the switch can engage an internal $50\,\Omega$ load. As such, the radar was developed to support four switch modes, namely: internal termination, RF1, RF2, and interleaved. Of these modes, only interleaved requires its state be varied during the radar measurement. The switching frequency for the interleaved mode must account for the selected pre-sum factor, and is therefore equal to $\mathrm{PRF}_{\mathrm{e}}$.

The final responsibility of the TCU is to generate the so called *event trigger*, which is simply a pulse that is synchronous with the first and last radar transmission. This signal is used to trigger an external GNSS module, which registers a timestamp used to synchronise positional and radar data in post processing.

3.3 Waveform Synthesis

A pair of LMX2492EVM [66] fractional-N PLL evaluation boards synthesise the radar's linear TX and DX FMCW waveforms at RF. The *average* output frequency

(f_{out}) produced by each fractional-N PLL is expressed as

$$f_{\text{out}} = f_{\text{PD}} \left(N_0 + \frac{F_{\text{n}}}{F_{\text{d}}} \right) /D, \tag{3.6}$$

where N_0 is the feedback divider's initial integer component, F_{n} and F_{d} are the numerator and denominator of the fractional component respectively, and D is the VCO divider [59]. It is important to note that the *instantaneous* frequency produced by the PLL is unknown, since the feedback divider is continuously modulated between integer values to produce an effective fractional value.

Linear frequency sweeps are generated by adjusting the fractional numerator during each phase detector cycle (k), according to

$$F_{\text{n}}(k) = F_{\text{n}_0} + kI, \quad k \in \{0, 1, ..., L-1\}, \tag{3.7}$$

where F_{n_0} is the initial fractional numerator, I is the change in numerator per phase detector cycle, and L is the number of cycles.

The evaluation board's 5 V tuning range limits its VCO to produce frequencies between 9.4 GHz and 10.1 GHz [66]. However, an integrated factor-of-four frequency divider (D) enabled the radar's operation at S-band, which reduced the available RF bandwidth to $\Delta F = 175\,\text{MHz}$, between 2.35 GHz and 2.525 GHz. Full use of this modulation bandwidth constrained the radar's centre frequency to $f_c = 2.4375\,\text{GHz}$.

When configured to produce frequency ramps, the LMX2492 forces its fractional denominator to its maximum value of $F_{\text{d}} = 2^{24} - 1$. As mentioned in the literature review, this ensures that the largest equivalent fraction is always used. With this, the majority of variables in Equation 3.6 are constrained, leaving the waveform design procedure to revolve largely around setting appropriate values of I and L. For convenience, Table 3.2 provides a summary of constrained parameters.

3.3.1 PLL Loop Bandwidth

PLL loop bandwidth plays an important role in achieving a linear transition between the frequency steps defined in Equation 3.7. For optimal linearity the loop

Table 3.2: Constrained PLL Parameters

Parameter	Variable	Value
Phase Detector Frequency	f_{PD}	125 MHz
Initial Integer Divider	N_0	75
Initial Fractional Numerator	F_{n_0}	3 355 443
Fractional Denominator	F_{d}	16 777 215
VCO Output Divider	D	4

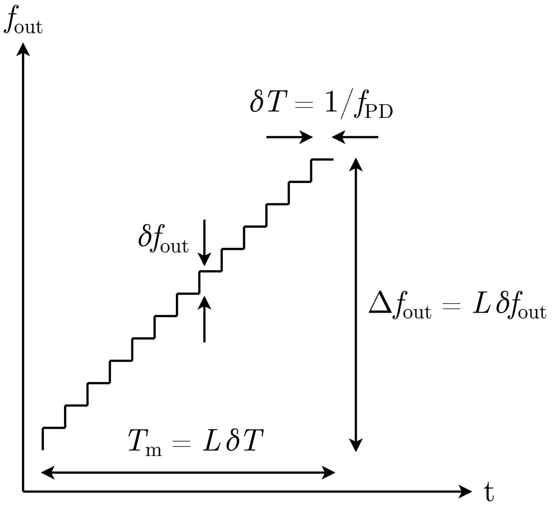

Figure 3.7: Example PLL frequency staircase function. Loop bandwidth is tuned to ensure a linear transition between the frequency steps.

bandwidth (f_{LB}) must fall between the following bounds:

$$\frac{1}{T_{\mathrm{m}}} \ll f_{\mathrm{LB}} < \frac{1}{\delta T}, \tag{3.8}$$

where T_{m} is the ramp's modulation period and δT is the interval between frequency steps [25]. Figure 3.7 presents an example frequency staircase function which illustrates the meaning of these parameters. Equation 3.8 ensures that the PLL is fast enough to follow the ideal linear frequency ramp, but not too fast as to settle at each frequency step [27]. Defining $\delta T = 1/f_{\mathrm{PD}}$ and $T_{\mathrm{m}} = L\,\delta T$, reveals that the upper bound is unrealistic and can be neglected, while the lower bound is waveform dependent.

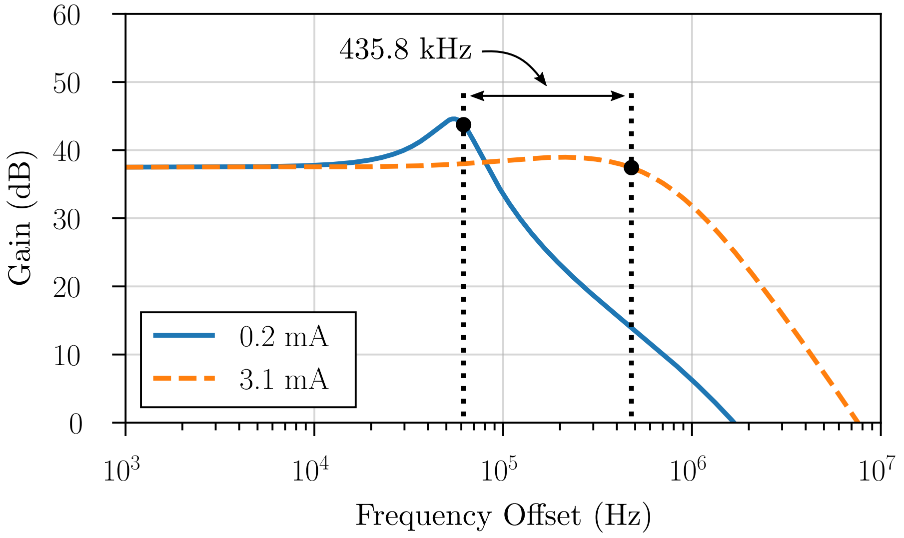

Figure 3.8: Bode plot of the LMX2492EVM closed-loop transfer function for varying CPG, where $N_{\text{int}} = 75$ and $K_{\text{VCO}} = 200\,\text{MHz/V}$. The resultant loop bandwidths are 42.0 kHz and 477.8 kHz for gains of 0.2 mA and 3.1 mA respectively.

Of further consideration, an increase in loop bandwidth permits low-offset spurs and noise (generated by the phase detector and charge pump) to pass through the PLL unfiltered [67]. To demonstrate this, the loop bandwidth can be adjusted using the PLL CPG [59], according to

$$f_{\text{LB}} \propto \sqrt{\frac{K_{\text{PD}}\,K_{\text{VCO}}}{N_{\text{int}}}}, \tag{3.9}$$

where K_{PD} is the CPG, K_{VCO} is the fixed nominal gain of the VCO and N_{int} is the instantaneous integer component of the feedback divider.

Figure 3.8 illustrates the simulated closed-loop response of the LMX2492EVM for CPG values of 0.2 mA and 3.1 mA, which correspond to loop bandwidths of 42.0 kHz and 477.8 kHz respectively. These were the minimum and maximum loop bandwidths that could be implemented in practice. Figure 3.9 presents measured 2375 MHz tones that correspond to these CPG values. As will be explained in Section 3.3.2, the choice of frequency in Figure 3.9 is deliberate, since only the reference signal's spurs appear in this figure. This can be confirmed through comparison of Figures 3.4 and 3.9.

When viewed in conjunction, Figures 3.8 and 3.9 show that both spurs and the

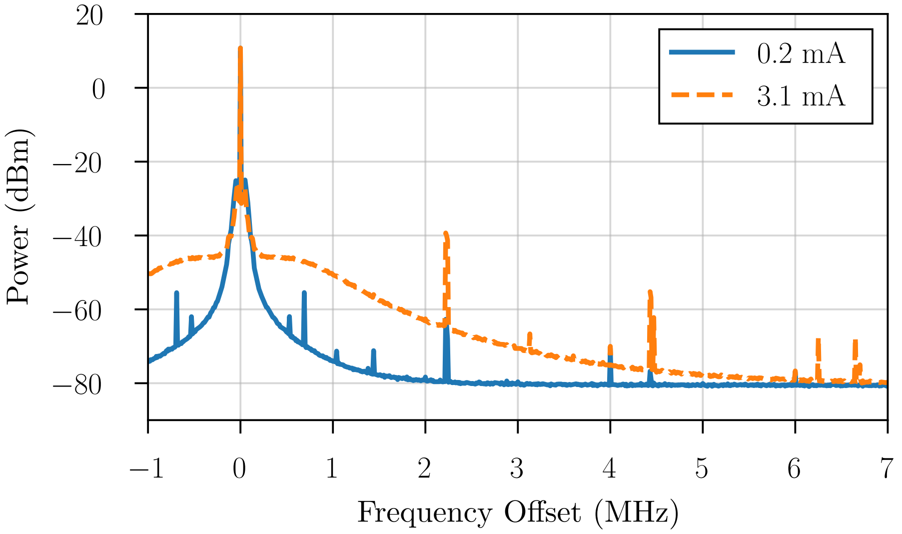

Figure 3.9: Power spectrum of a 2375 MHz tone, measured at synthesiser output with a RBW of 1 kHz. The radar's transmission power level is seen to be ≈ 10 dBm. Reducing the loop bandwidth clearly suppresses the phase noise skirt and reference signal spurs.

phase noise skirt can be greatly suppressed when the loop bandwidth is reduced. This concept will be revisited in Section 5.3, where loop bandwidth reduction is used to suppress other types of spurs.

3.3.2 Spurious Signals

Spurs produced by the fractional-N PLLs further complicate the radar's design. If the full frequency range of the LMX2492EVM is used (9.4 GHz to 10.1 GHz) then its VCO sweeps past 5 integer multiples of the phase detector frequency. These VCO frequencies, and the resultant (divided) output frequencies, are presented in Table 3.3.

At the tabulated VCO frequencies, Equation 2.2 predicts that the IBS carrier-offset is zero, i.e. IBS intersect with the carrier at these frequencies. It is important to note that while the VCO divider theoretically reduces the magnitude of any spur passing through it by $20\log_{10}(D)$, the spur's relative frequency offset from the carrier remains the same [59].

The sweeping nature of IBS can be illustrated by drawing focus to a single

Table 3.3: In-Band Integer Multiples of the 125 MHz Phase Detector Frequency

N	f_{VCO} (MHz)	f_{out} (MHz)
76	9500	2375.00
77	9625	2406.25
78	9750	2437.50
79	9875	2468.75
80	10 000	2500.00

intersection point at one of the tabulated frequencies. To this end, Figure 3.10 presents the measured PLL output spectrum, when configured to generate single tones at frequencies of 2375 MHz, 2375.25 MHz and 2375.5 MHz. These discrete frequencies can be considered instantaneous points within an arbitrary frequency sweep.

As an integer multiple of the phase detector frequency, the 2375 MHz tone is free of IBS and contains only modulated spurs from the reference clock, as discussed in Section 3.2.1. When the carrier frequency is increased to 2375.25 MHz, however, IBS labelled A and B become apparent. Increasing the carrier again to 2375.5 MHz, reveals that the offset of A and B increases and a third IBS (labelled C) appears. The offset of each IBS increases as the carrier frequency increases away from 2375 MHz. The offset of each IBS would decrease symmetrically had the intersection point been approached from a lower frequency. Thus, IBS sweep into and out of the PLL loop bandwidth as the carrier frequency moves past each integer multiple of the phase detector frequency.

Figure 3.11 extends the measurements of Figure 3.10 and illustrates the sweeping IBS over a greater range of carrier frequencies. This figure was generated by subtracting the mean of the measured spectra, such that the *constant* reference signal's spurs and carrier signal are removed. As a result, the spectral content at a carrier frequency of 2375 MHz is almost entirely eliminated.

The offset of IBS A in Figures 3.10 and 3.11 can be calculated by rearranging Equation 3.6 to find F_{n} for a given f_{out}, and applying the result to Equation 2.2. As an example, $f_{\text{out}} = 2376$ MHz requires $F_{\text{n}} = 17\,314\,087$, which results in $f_{\text{IBS}_A} = \pm 4$ MHz. This agrees with the measured spur offset seen in Figure 3.11. The offset

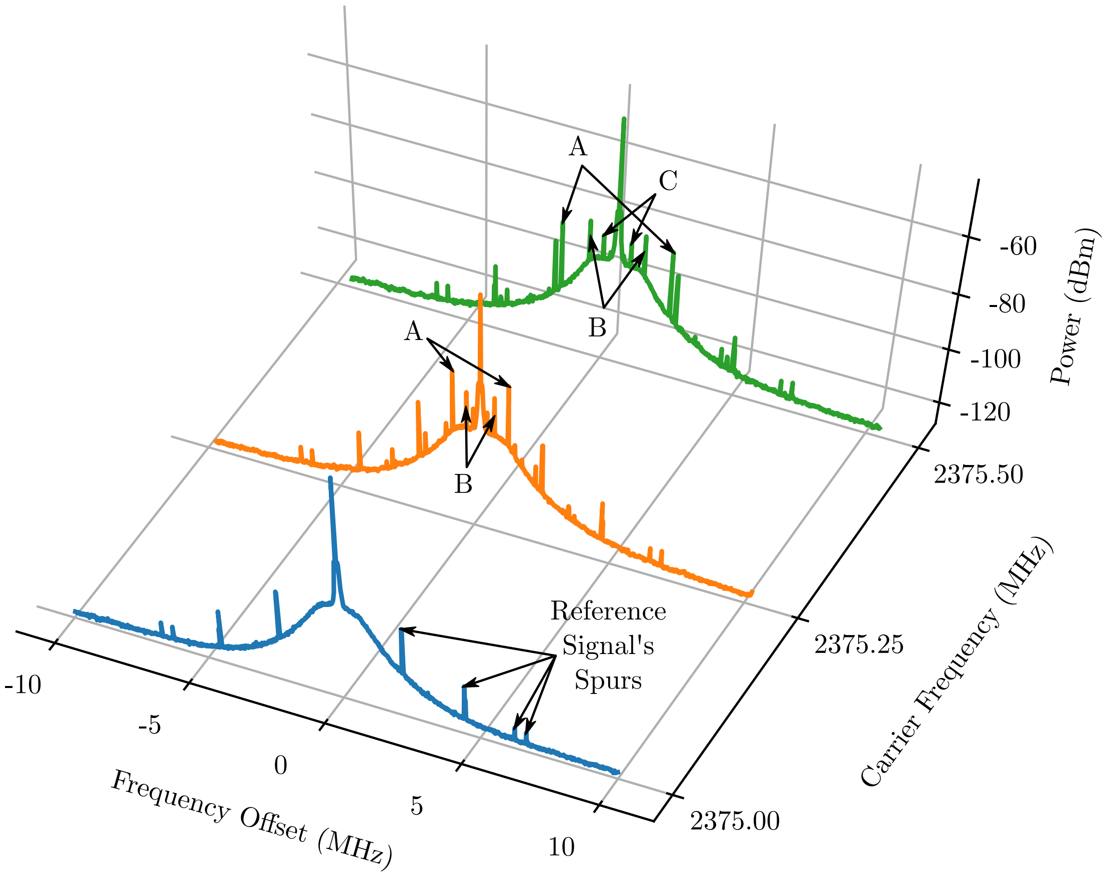

Figure 3.10: Measured PLL output spectra for carrier frequencies of 2375 MHz, 2375.25 MHz and 2375.5 MHz. $K_{\mathrm{PD}} = 477.8\,\mathrm{kHz}$. The offset of each IBS increases as the carrier frequency increases. The offset of the reference signal's spurs is fixed.

of IBS B is given by $f_{\mathrm{IBS}_A}/2$, while C appears at $f_{\mathrm{IBS}_A}/4$. Note that in reality F_{n} is always less than or equal to F_{d}, and that the integer component of the feedback divider increments each time that the value of F_{n} would exceed F_{d}. It is, however, mathematically equivalent to allow $F_{\mathrm{n}} > F_{\mathrm{d}}$, which serves to simplify calculations.

As explained in Section 2.3.3, PDH differ from IBS in that they are *direct* spurs and therefore do not pass through the VCO divider. Furthermore, PDH do not sweep, but rather appear at fixed frequencies through slow-time, as expressed in Equation 2.3. Evaluation of Equation 2.3 for values of $h = 19$ and 20 predicts PDH at frequencies of 2375 MHz and 2500 MHz, which both fall within the RF bandwidth. Figure 3.12 reveals the power spectra of the PDH measured at these

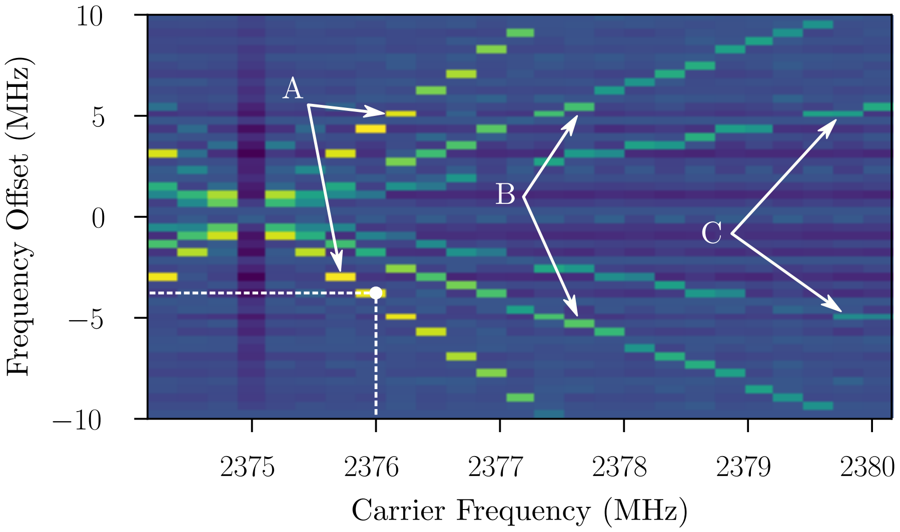

Figure 3.11: Visualisation of the IBS offset frequency as a function of carrier frequency.

frequencies.

Since the FMCW carrier is swept through slow-time, the frequency difference between the PDH and the sweeping carrier is swept as a function of slow-time. Therefore, both IBS and PDH are examples of spurs whose offset from the carrier sweeps through slow-time. The concepts of slow- and fast-time are clearly explained in Chapter 3 of [68]. To the best of the author's knowledge, the effect of IBS and PDH on the performance of FMCW radar, specifically heterodyne FMCW SAR, has not been addressed in the literature.

3.4 Analogue Dechirp

Dechirp (or *deramp*) is an analogue down-conversion procedure for frequency-swept waveforms. Under this technique, RX echoes are mixed with a reference DX waveform whose sweep-rate is matched to that transmitted. After appropriate filtering, each frequency ramp is transformed into a corresponding beat tone, whose frequency (f_b) depends on the instantaneous difference between the RX and DX waveforms.

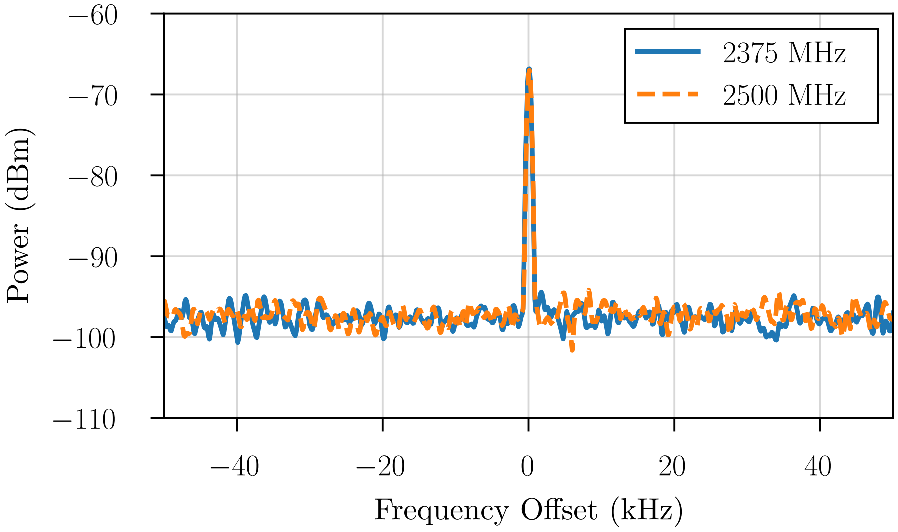

Figure 3.12: Measured spectrum of the PDH within the available RF bandwidth, over a span of 100 kHz. Both PDH appear at a power level of −67 dBm, when measured with a RBW of 500 Hz.

$$f_{\mathrm{b}} = \left(\frac{\Delta f_{\mathrm{out}}}{T_{\mathrm{m}}}\right)\frac{2R}{c} = \beta\frac{2R}{c}. \tag{3.10}$$

The miloSAR's dual synthesiser design strays from tradition in its utilisation of an independent DX waveform synthesiser to drive the mixer's LO port. Control over this DX waveform affords the system designer the ability to implement configurable time and/or frequency offsets between otherwise equivalent TX and DX waveforms. Either offset can be leveraged to introduce an IF, resulting in a heterodyne receiver architecture. A single cycle of the generic waveforms required to implement either offset are overlaid in Figure 3.13. This figure presents the ideal scenario, where the effects of PLL loop bandwidth on sweep linearity are not considered.

For a time offset, the TX and DX PLLs are configured to follow f_{TX_t} and f_{DX_t} respectively. Similarly, a frequency offset is implemented using f_{TX_f} and f_{DX_f}. Overlaying these waveforms in Figure 3.13 shows that they follow the same set of frequencies during the up-ramp. Note that the effective modulation bandwidth under either technique is identical. This is because the use of commercial PLL

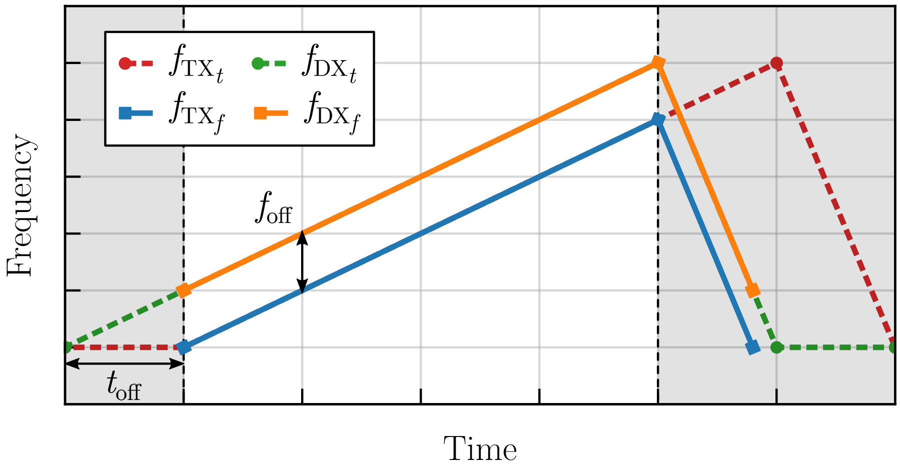

Figure 3.13: Illustrative spectrogram of the waveforms required to implement either a time or frequency offset. A single cycle of each waveform combination is provided. The regions of the waveforms which are not stored for processing have been greyed-out. The frequencies traversed during the up-ramp are seen to be the same under either offset.

evaluation modules limits both PLLs to the same range of output frequencies. As such, the introduction of either an explicit frequency offset (f_{off}) or time delay (t_{off}) will result in a reduction in the effective modulation bandwidth. This leads to a proportional reduction in range resolution, and limits the IF to a small percentage of the modulation bandwidth.

On initial inspection, the time- and frequency-offset approaches to heterodyning may appear to be trivially similar, however, a critical distinction can be made. The frequency-offset approach requires f_{off} to be measured, such that the beat spectrum can be down-converted without any residual phase error. On the other hand, the time-offset approach can be down-converted with a synthetic LO within the DDC. The reason for this will be exposed in the subsections that follow.

3.4.1 Frequency Offset

An explicit frequency offset (f_{off}) can be introduced between the TX and DX waveforms by manipulating the initial fractional numerator (F_{n_0}) programmed into each PLL. If ΔF_{n_0} is the difference in the initial fractional numerator between the two waveforms, then

$$f_{\mathrm{off}} = f_{\mathrm{PD}} \left(\frac{\Delta F_{\mathrm{n_0}}}{F_{\mathrm{d}}} \right) / D, \tag{3.11}$$

which can be found through simple manipulation of Equation 3.6. The resultant beat frequency f_{b} is given by

$$f_{\mathrm{b}} = \beta \tau + f_{\mathrm{off}}, \tag{3.12}$$

where β is chirp rate, and τ is round-trip propagation time.

The disadvantage of this approach to heterodyning is that the instantaneous value of $f_{\mathrm{off}}(t)$ is unknown. This is due to the averaging mechanism that fractional-N PLLs use to produce non-integer multiples of their phase detector frequency. Rapidly modulating the PLL feedback divisor between integer values introduces uncertainty in the *instantaneous* output frequency of each PLL. By extension, there is uncertainty in the instantaneous frequency difference between PLL output.

Down-conversion of the beat spectrum using the average value of f_{off} (as calculated using Equation 3.11) results in residual phase error through slow time, which manifests as a Doppler shift. This problem is now elaborated upon.

If ϕ_{TX_i} and ϕ_{DX_i} represent each waveform's unknown initial phase for the i-th PRI, then the relative phase between waveforms can be expressed as

$$C_i = \phi_{\mathrm{DX}_i} - \phi_{\mathrm{TX}_i}. \tag{3.13}$$

Under the condition that the synthesisers remain locked during operation, the respective phase increment between successive PRIs is given by the area under each spectrogram,

$$\phi_{\mathrm{DX}_{i+1}} = \phi_{\mathrm{DX}_i} + 2\pi (f_c + f_{\mathrm{off}}(t))\mathrm{PRI}, \tag{3.14}$$

$$\phi_{\mathrm{TX}_{i+1}} = \phi_{\mathrm{TX}_i} + 2\pi f_c \mathrm{PRI}. \tag{3.15}$$

Substitution of (3.14) and (3.15) into (3.13), results in an expression for the slow-time pulse-to-pulse phase increment,

$$C_{i+1} - C_i = 2\pi f_{\text{off}}(t)\text{PRI}. \tag{3.16}$$

Attempted demodulation of (3.16) using a synthetic LO (based on the expected value of f_{off}), will result in a residual slow-time phase error. In turn, this residual error will cause integration loss in any further processing that requires coherency.

It is possible to sample the true value of $f_{\text{off}}(t)$ for use as a digital LO, if portions of the TX and DX waveforms are coupled and mixed in a dedicated reference channel. This is the approach adopted by several systems that employ multiple VCOs [44,45], since it carries the additional benefit of partially cancelling the uncorrelated phase noise between independent VCOs. However, this approach is undesirable as it increases system cost and complexity.

Alternatively, $f_{\text{off}}(t)$ can be extracted from the instantaneous phase of the feed-through signal, which is expected to remain constant through slow-time. Once extracted, the fluctuations can be used to correct the slow-time phase of every range profile. Drawbacks of this approach include its reliance on accurate phase unwrapping and the additional bandwidth required to intentionally sample the feed-through signal.

3.4.2 Time Offset

The introduction of a time offset, between otherwise equivalent TX and DX waveforms, offers an attractive alternative to the explicit frequency offset approach,

$$f_{\text{b}} = \beta(\tau - t_{\text{off}}), \tag{3.17}$$

where t_{off} is a configurable time offset with respect to the TX waveform. A negative value of t_{off} describes a scenario in which the DX leads the TX waveform, which serves to increase the beat frequency of every target. Practically, this time offset is constrained to be in integer multiple (n) of the reference clock period,

$$t_{\text{off}} = \frac{n}{f_{\text{PD}}}. \tag{3.18}$$

The lack of an explicit frequency offset between the TX and DX signals leads to a convenient simplification for down-conversion: both waveforms have the same area under their spectrogram. As such, they experience the same phase increment over each PRI and their relative phase remains constant through slow-time,

$$C_{i+1} - C_i = 0. \tag{3.19}$$

In this way, the disadvantages associated with an explicit frequency offset are avoided and the beat spectrum can be digitally demodulated without precise knowledge of the instantaneous IF. This is a great advantage over the frequency-offset approach, since it eliminates the requirement for a reference channel. As such, fully polarimetric operation is achievable with the two available receiver channels. This constitutes the first step in answering research question two, as a reference channel is not required to ensure slow-time phase coherency.

3.5 Analogue Range Gate

According to the FMCW Equation (3.10), chirp rate (β) serves as a configurable scaling factor between range (R) and beat frequency (f_b). Appropriate design of β can therefore be used to set the bandwidth associated with a particular range extent. Higher chirp rates spread target responses over a wider IF bandwidth which may improve the effectiveness of a hypothetical analogue range gate with a fixed filter roll-off. However, increased chirp rates require higher sampling frequencies that result in greater DRs.

Each of the miloSAR's receiver channels contain a SBP-10.7+ BPF, which serves as an analogue range gate. This filter features a 3 dB bandwidth of 3.8 MHz and a lower-side 3 dB cut-off frequency of 8.5 MHz as illustrated in Figure 3.14.

As stated in Section 3.2.2, the miloSAR's DDC is capable of selecting and storing 3.125 MHz of IF bandwidth. When combined with the radar's ability to adjust its IF (using a variable time offset), the beat frequency that corresponds to zero range can be adjusted to meet the needs of different experimental geometries.

For maximal feed-through suppression, the beat frequency that corresponds to zero range should be mapped to one of the filter's null frequencies, with targets

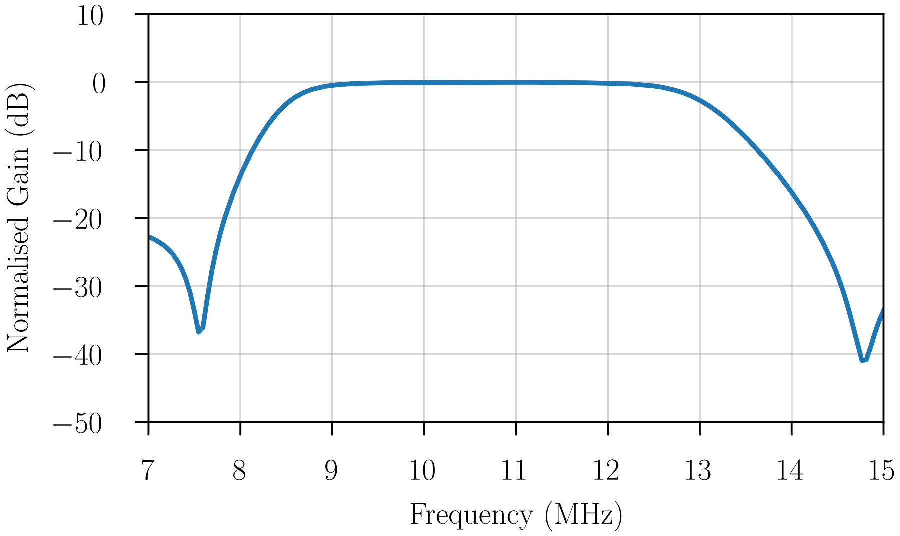

Figure 3.14: Frequency response of the SBP-10.7+ IF BPF, which serves as the miloSAR's analogue range gate.

appearing in the filter's passband. While either null could be used in principal, the one at 7.5 MHz offers a steeper roll-off and is therefore preferred. The degree to which this filter is able to suppress feed-through, however, is dependent on the geometry of the scene and the bandwidth and chirp rate constraints.

For ground-based scenarios in which targets appear at ranges between say 10 m and 200 m, the radar's chirp rate can be increased such that this range extent corresponds to the available 3.125 MHz of bandwidth. The presence of near range targets, however, restricts the zero-range beat frequency to values higher than say 8 MHz to avoid significantly attenuation.

Alternatively, airborne experiments benefit from the vertical displacement of the radar with respect to the first target of interest. Zero range can therefore be mapped to the null at 7.5 MHz, with the nadir return at 8.5 MHz. Responses from targets extending from 8.5 MHz onward can then be extracted using the DDC, while the feed-through response is discarded. This means that the bandwidth corresponding to the empty range between platform and ground is not stored.

This section has explained how the combination of a DDC and a configurable IF allows the miloSAR to be configured for operation in varying experimental conditions, such that the efficacy of the analogue range gate is optimised.

3.6 System Characterisation

This section presents the results of system characterisation measurements that were conducted during the miloSAR's development. These measurements validate the system's fundamental functionality and provide a baseline against which future experiments can be compared. The results of these measurements led to the identification of spur chirp interference.

3.6.1 Power Measurement

Fast Fourier Transform (FFT) based measurement of absolute signal power is prone to numerous error sources, namely: spectral leakage, coherent power gain, scalloping loss, processing gain and Equivalent Noise Bandwidth (ENBW) [69]. The procedure described by Heinzel *et al.* [70] was used to account for these phenomenon when scaling the Power Spectrum (PS) and Power Spectral Density (PSD) plots generated by the miloSAR.

To test the radar's power measurement accuracy, a signal generator was configured to produce a 10 MHz tone at 10 dBm which was measured by both the STEMlab and an available SA for comparison. For this experiment, the STEMlab's secondary channel was terminated with a 50 Ω load. Figure 3.15 illustrates the power spectra measured in this configuration. The SA and STEMlab show clear agreement, differing only by 0.14 dB at 10 MHz. This negligible offset was attributed to the difference in RBW and ENBW between the devices. The spurs visible on either side of the 10 MHz tone were unintentionally produced by the signal generator.

3.6.2 ADC Channel Cross-Talk

Cross-talk between the radar's ADC channels was determined to be 57.7 dB, as measured directly from Figure 3.15. This is almost 3 dB better than the nominal value of 55 dB, as quoted in the STEMlab documentation [71]. The difference between quoted and measured values was attributed to the STEMlab's front-end gain setting. The nominal value is based on the high voltage gain setting, while the miloSAR uses the low voltage option.

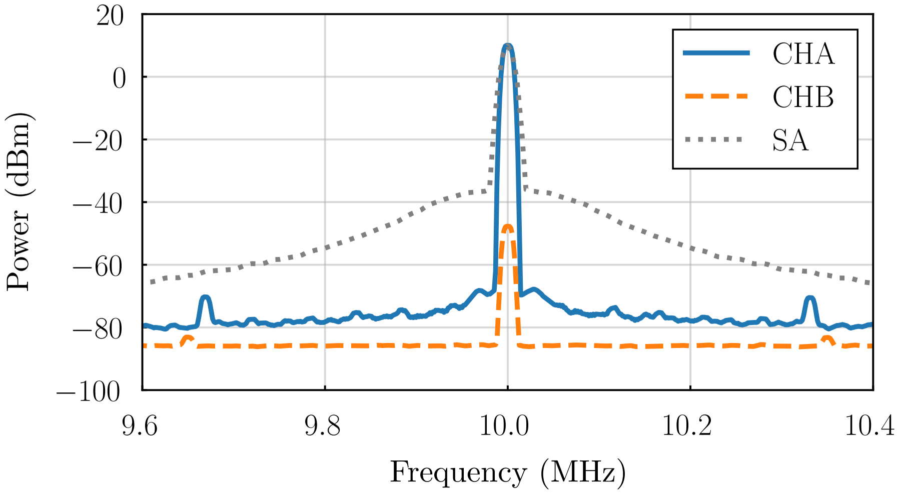

Figure 3.15: Power spectrum of the 10 MHz signal generator tone, as measured by the STEMlab and SA. Traces CHA and CHB represent the spectra for STEMlab receiver channels A and B respectively. Non-coherent average of 1000 profiles.

3.6.3 System Noise Floor

The noise floor of the STEMlab was measured by 50 Ω terminating all of its DAC and ADC ports. The PSD plot in Figure 3.16 reveals a measured noise floor of −131.9 dBm/Hz under these conditions.

After reconnecting the STEMlab's ADCs to the receive chain and terminating all antenna ports, the radar's noise floor was measured at −118.5 dBm/Hz over the IF band, as seen in Figure 3.17.

This noise floor value was found to be dominantly generated by the cascaded DVGAs in the receive chain. To prove this, the previous measurement was repeated with the cascaded DVGA input ports terminated. Figure 3.18 illustrates that average noise power density measured over the band is approximately −119 dBm/Hz under these conditions.

Comparing Figures 3.17 and 3.18 illuminates the presence of a tone at 8.21 MHz in the former. This signal is due to leakage within the system, and is assessed in the section that follows.

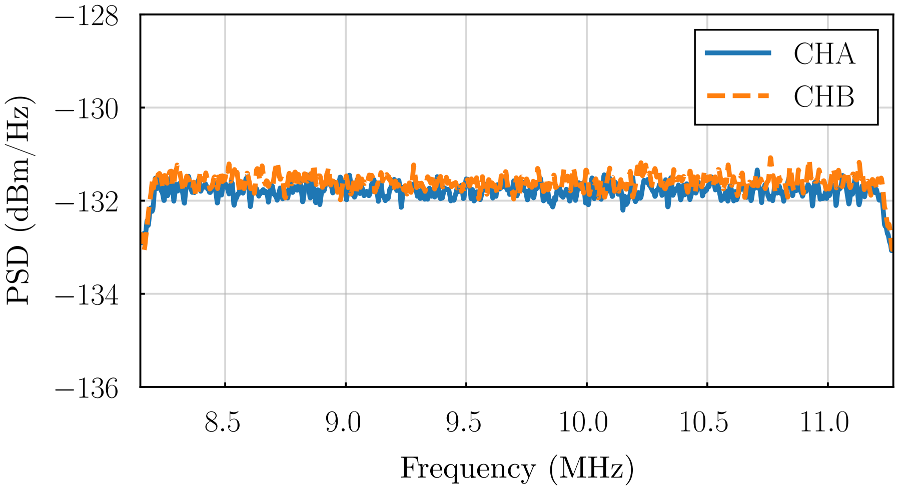

Figure 3.16: Noise spectral density of the STEMlab, measured when all ADC and DAC ports are terminated with 50 Ω loads. The average density over the band was measured as −131.9 dBm/Hz. Non-coherent average of 1000 profiles.

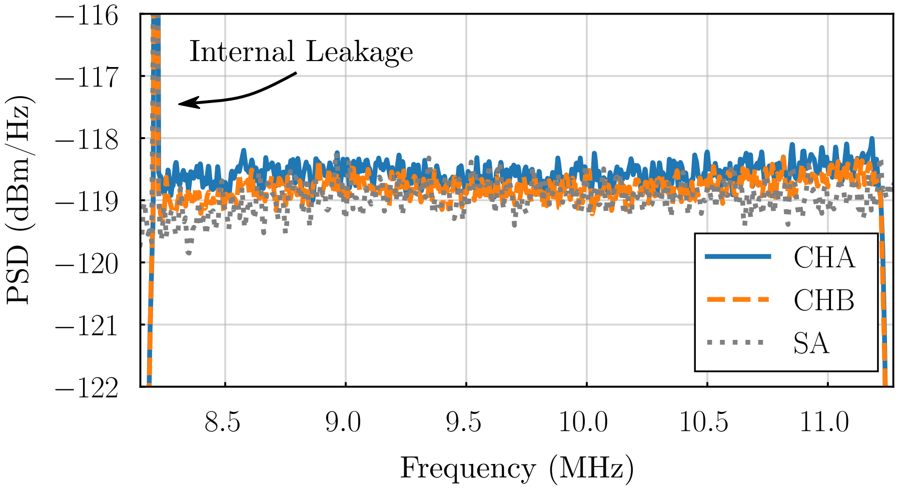

Figure 3.17: Noise power density measured by STEMlab and SA when all antenna ports were terminated. The STEMlab and SA differ by approximately 0.5 dB. The signal visible at 8.21 MHz is internal leakage. Non-coherent average of 1000 profiles.

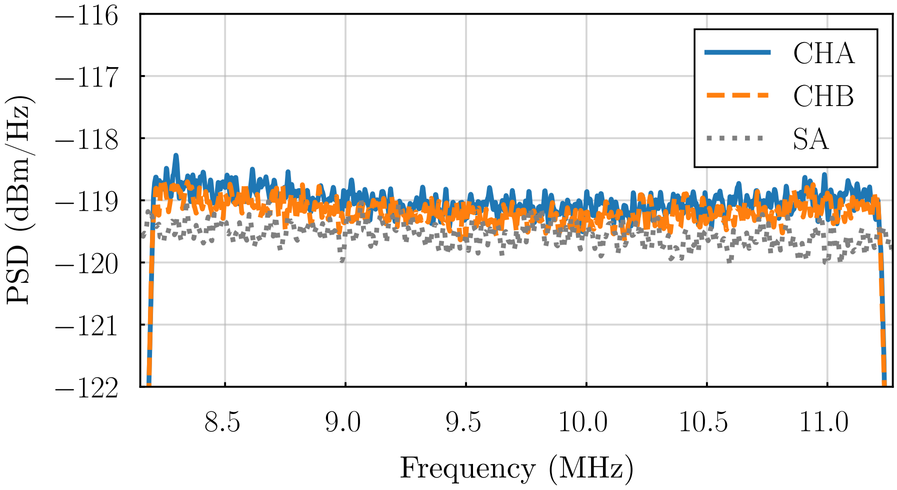

Figure 3.18: Noise spectral density at the cascaded DVGA output, when inputs are 50 Ω terminated. The average density measured by the STEMlab over the band is −119 dBm/Hz, differing from the SA by approximately 0.5 dB. Non-coherent average of 1000 profiles.

3.6.4 Internal Leakage

Zero-range interferers manifest within the system as a result of reflections and internal component leakage. Figure 3.19 presents the PS measured when the internal polarisation switch and all antenna ports were terminated. In this figure, both channels report a value of −67.8 dBm for the leakage signal.

3.6.5 Measurement Precision

The precision with which the miloSAR can measure target amplitude and phase through slow-time was tested using a reel of HUBER+SUHNER 50 Ω coaxial cable as a stationary target.

Figure 3.20 illustrates the absolute value of the range bin corresponding to the loop-back cable over 32 s, once its mean has been removed. A linear regression line has been fit through the data for reference, revealing that the mean value drifts by less than 5 mV over the measurement period.

It was concluded that the magnitude value is perturbed by Additive White Gaussian (AWG) noise, after assessing its uniform PSD and normal Probability Density Function (PDF), as seen in Figure 3.21.

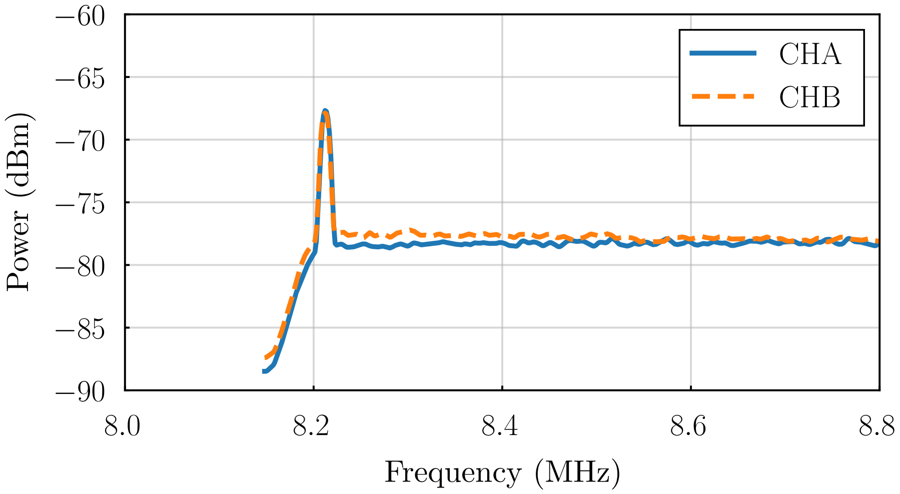

Figure 3.19: Power spectrum of the internal leakages signal measured with the STEMlab, with all TX and RX ports terminated. Non-coherent average of 1000 profiles.

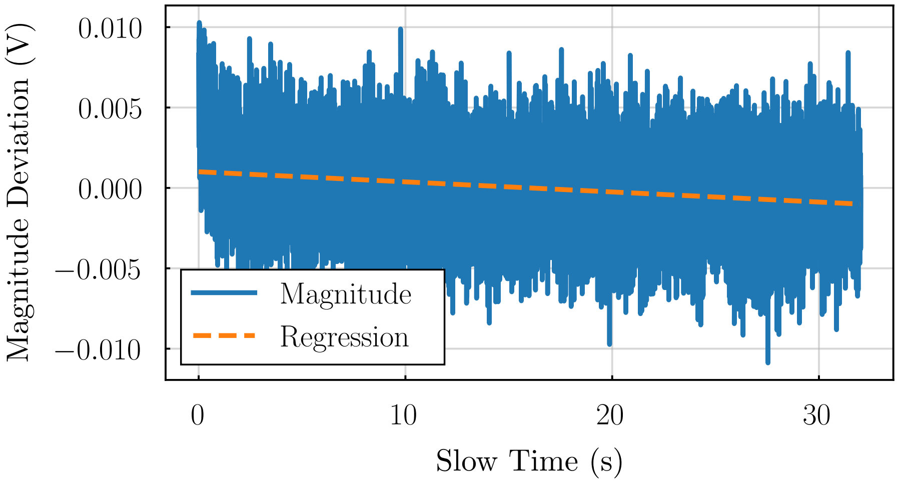

Figure 3.20: Deviation in the magnitude of the loop-back cable's range bin from its mean value over 32 s of slow-time.

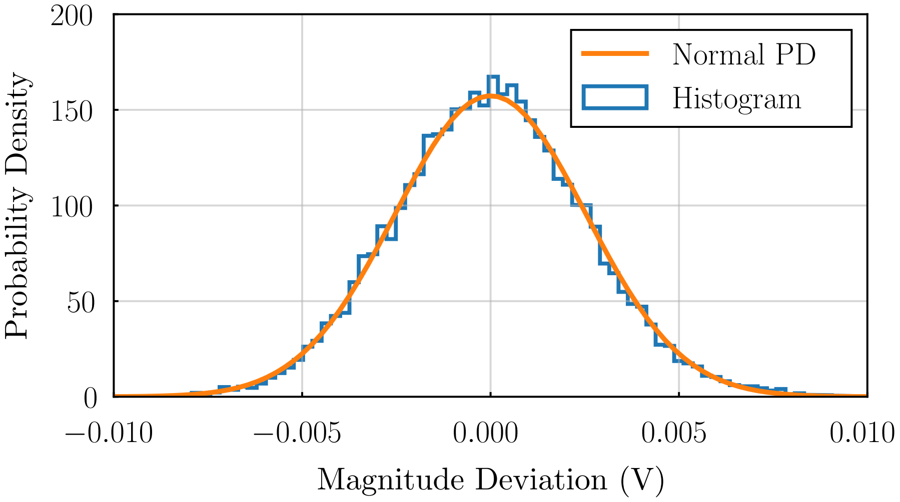

Figure 3.21: Histogram of magnitude deviation values, normalised to provide a discrete probability density function. On top of this, a normal distribution function has been fit to the data, and shows excellent agreement with the normalised histogram. The Gaussian curve is described by a mean of $\mu = 0$ and standard deviation of $\sigma = 2.5\,\text{mV}$. Note that the bin width is 246 µV, such that that the integrated area is unity.

The instantaneous phase of the same range bin is plotted through slow-time in Figure 3.22. Here, the phase deviation is presented relative to the first sample. An initial non-linear deviation is clearly visible, after which the drift is dominantly linear.

This initial non-linearity (which can be observed in both magnitude and phase) was attributed to system dynamics, and resembles the step response of a damped first-order system. The settling time required to reach *steady state* drift is approximately 1 s. While the first second's worth of samples could simply be discarded during processing, the associated integration loss is now shown to be negligible.

Richards [72] showed that coherent integration loss L_{int}, i.e. the ratio of integrated power when phase noise is present to the power when it is not, is given by

$$L_{\text{int}} = 10 \log_{10} \left(\frac{1 + e^{-\sigma^2}(N-1)}{N} \right), \tag{3.20}$$

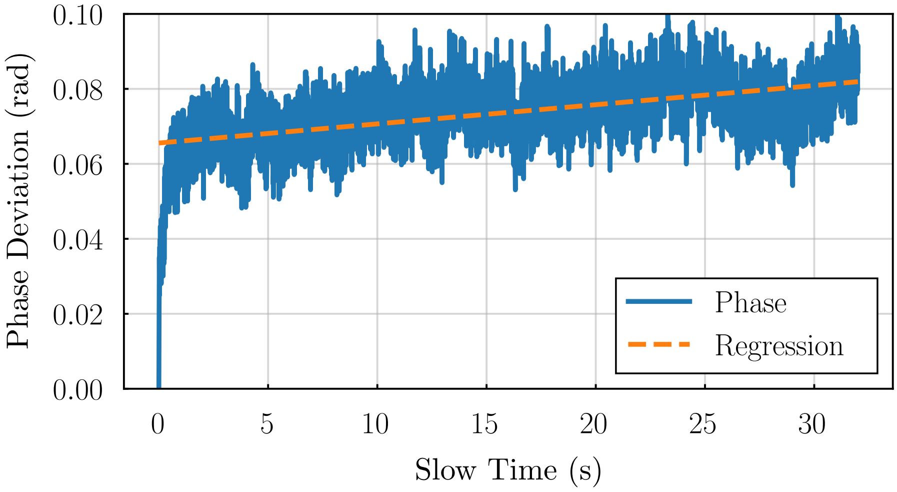

Figure 3.22: Instantaneous phase of the loop-back cable response, observed over 32 s. A linear regression line is provided for reference. Over the observed period, the total drift is approximately 0.08 rad. This data is well represented by a Gaussian distribution of mean $\mu = 0.073$ rad and standard deviation $\sigma = 0.008$ rad.

where σ^2 is noise variance and N is the number of slow-time phase samples. The exact integration loss can however, be calculated directly from the phase samples ϕ_n as follows,

$$L_{\text{int}} = 20 \log_{10} \left(\frac{1}{N} \left| \sum_{i=1}^{N} e^{i\phi_n} \right| \right). \tag{3.21}$$

Evaluation of Equations 3.20 and 3.21 agree that the total phase drift presented in Figure 3.22 induces a coherent integration loss of 290e−6 dB. This negligible loss clearly does not necessitate the elimination of the first second's worth of samples.

This section showed that the miloSAR is capable of precise magnitude and phase measurement over an extended period, a vital requirement for SAR applications. Furthermore, the negligible phase drift demonstrated that the time-offset approach to heterodyning allows the radar to operate coherently without a reference channel, which serves as an answer to the second research question.

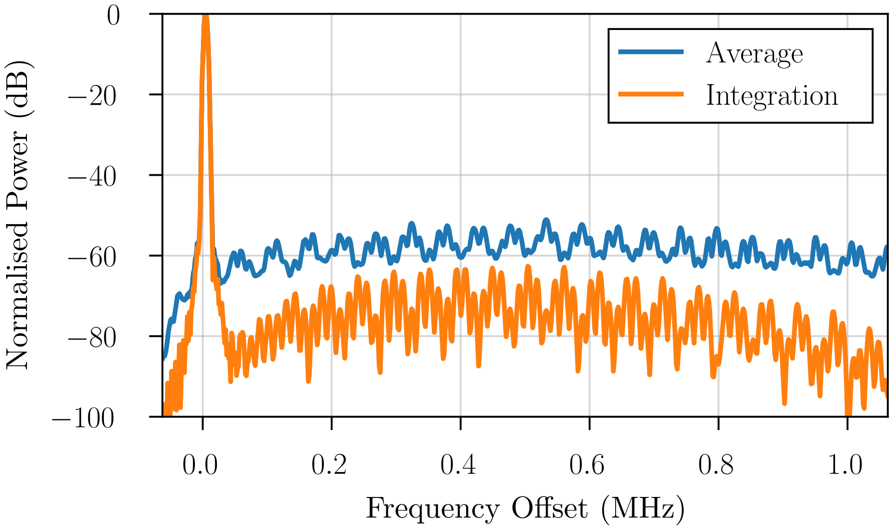

Figure 3.23: Non-coherent average and coherent integration of 1000 range profiles. An SNR improvement of 30 dB was expected, but did not materialise.

3.6.6 Coherent Integration

Having verified that the radar measures target phase precisely, its ability to integrate range profiles coherently was of interest. To test this, a target was emulated by connecting a short cable and adequate attenuation between a pair of TX and RX ports. The target response was intentionally placed in the middle of the IF bandwidth for visual clarity and to avoid any filter effects at the edges.

Figure 3.23 presents the resultant range profile, where traces of both the non-coherent average and coherent integration of 1000 profiles are provided. The traces were normalised by the peak value of the non-coherent average. As explained in the previous section, negligible coherent integration loss is experienced by the peak at 10 MHz.

However, coherent integration of 1000 profiles should theoretically result in a 30 dB improvement to SNR. Clearly, no such improvement materialises in Figure 3.23, since the side-band level of the integration trace does not lower as expected. Instead, a ripple-like pattern is seen to manifest throughout the integration trace's side-band. It is important to note that this Figure 3.23 was generated with the maximum charge pump gain value, such that loop bandwidth was maximised. Furthermore, note that the first ±100 kHz offset contains comparably lower ripple levels that larger offset values.

It will be shown in Chapter 4 that the ripple pattern seen in Figure 3.23 is a result of swept-offset spurs, termed *spur chirps*. The remainder of this chapter, however, is dedicated to illustrating the impact of these spurs on SAR performance, should their origin and presence be unknown to the radar designer.

3.7 Baseline Performance

This section presents the results of a car-borne measurement campaign which was carried out in October 2018, before the problem of spur chirps was fully understood. These results serve as a baseline upon which the improvements presented in later chapters can be compared. Furthermore, the results may be useful to other radar designers who have noticed unexplained artefacts in their recorded data and use fractional-N PLLs for waveform synthesis.

3.7.1 UCT Field

The first set of experiments took place on the University of Cape Town (UCT) rugby fields, under the configuration shown in Figure 3.24.

The radar was mounted to the top of a car, 2 m Above Ground Level (AGL), and was driven along the path shown in the figure, from the green to the red marker. Three small reflectors were placed in the centre of the field, offset from each other by 10 m in the along-range and cross-range dimensions. A triangular trihedral, 45° dihedral and a sphere were mounted on pedestals to provide co- and cross-polarisation responses. These reflectors can be seen in Figure 3.25.

The car travelled at an average velocity of 5.75 m/s for the 15 s long experiment, as measured using the RTK GNSS. Figure 3.26 presents the resultant Range-Time-Intensity (RTI) plot, where point targets are seen to manifest as hyperbolic curves. The plot is an Red, Green, Blue (RGB) composite image where the red channel maps to Vertical Transmit, Vertical Receive (VV), the green channel represents Vertical Transmit, Horizontal Receive (VH), and the blue channel is the difference (VV - VH). As a result, targets which produced an odd number of bounces (vertical poles, sphere, and trihedral) are dominantly red, while

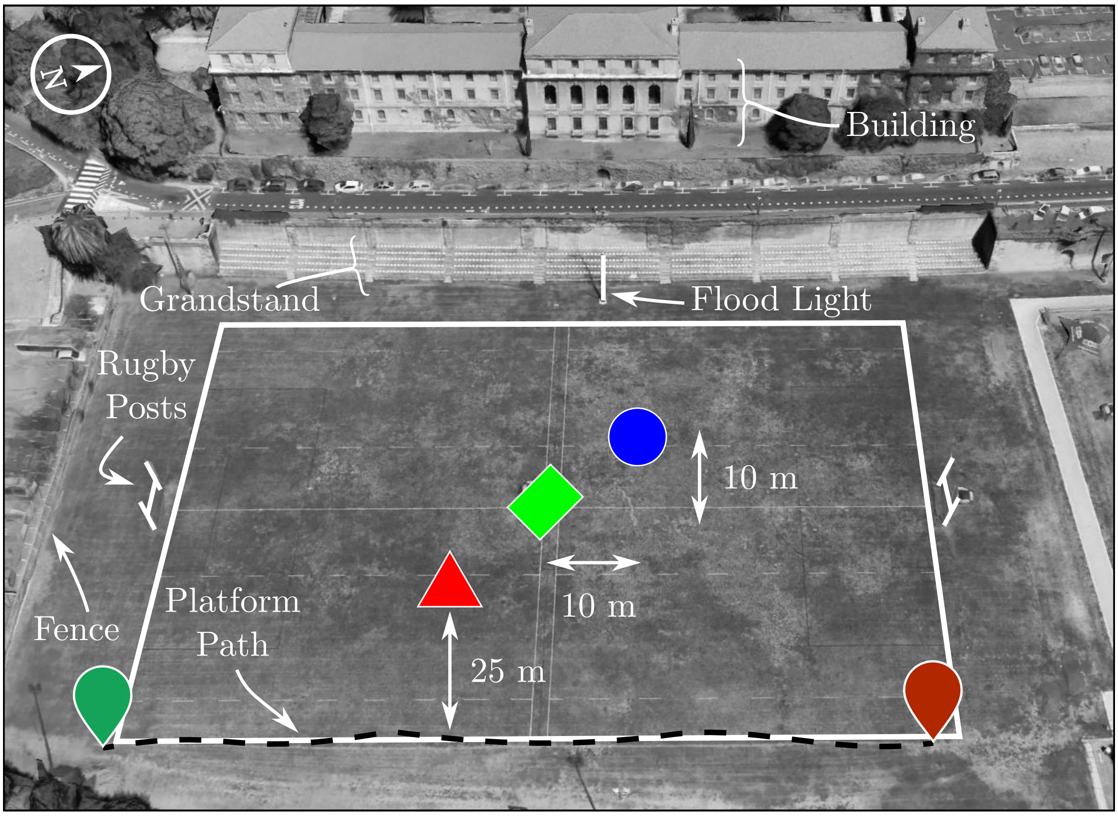

Figure 3.24: Geometry of the experimental field-based SAR setup. The red triangle represents the location of the triangular trihedral, the green rectangle represents the 45° dihedral, and the blue circle represents the sphere. Note the presence of the fence, rugby posts and flood light.

even-bounce signals (45° dihedral) are dominantly green. The sphere's response is not visible in this plot, owing to its low Radar Cross Section (RCS) value. This plot served as validation that the radar was capable of polarimetric measurements. Note that the ripples revealed in Figure 3.23 are not visible in this plot since no coherent integration has taken place.

The effect of the ripples can, however, be observed in the associated average RDM of Figure 3.27. An average RDM is formed by non-coherently adding several RDMs generated from subsets of the complete data set. The formation of each RDM requires a Fourier transform through slow time, which appears to compress the interference into specific frequency bins throughout range. This produces the vertical interference lines seen in Figure 3.27. As is to be expected, all target

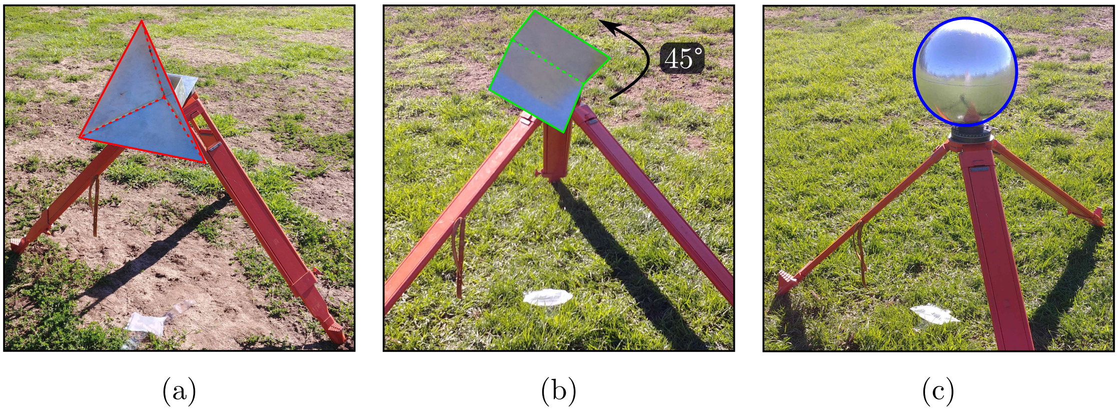

Figure 3.25: (a) Triangular trihedral, (b) dihedral at 45°, and (c) sphere reflectors on pedestals for the field-based SAR measurements. The reflectors have been colour coded to match the symbols seen in Figure 3.24.

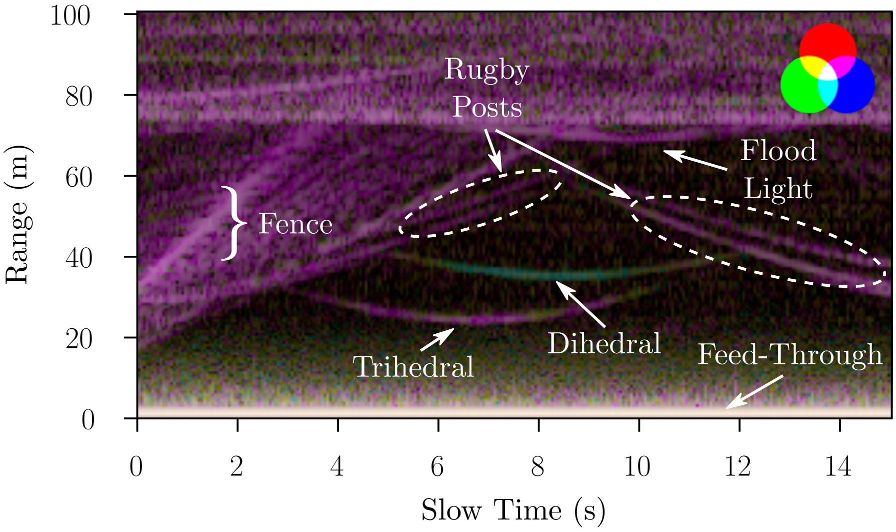

Figure 3.26: RTI plot corresponding to the field-based SAR measurements. The majority of signal content is seen to correspond with the VV channel, with the exception of the dihedral reflector. The feed-through signal is seen throughout slow-time at zero range. A colour wheel has been provided to illustrate how the colours mix together.

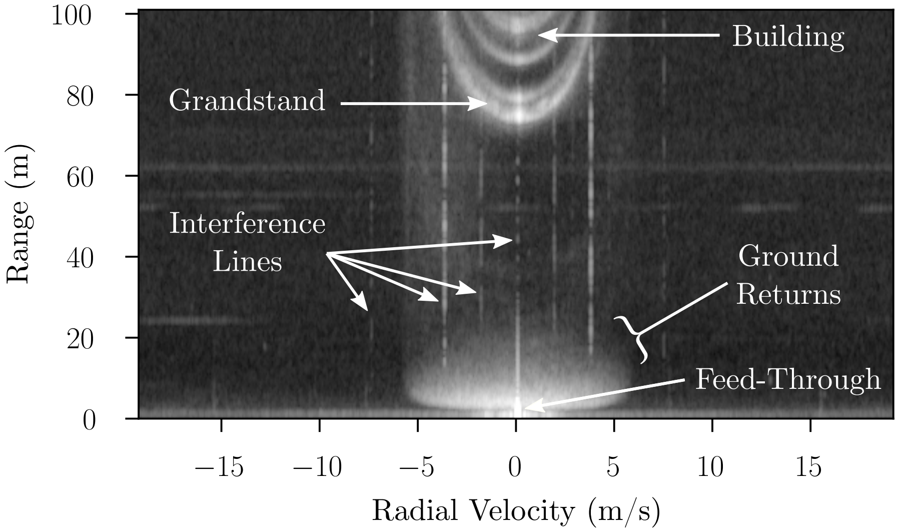

Figure 3.27: RDM corresponding to the field-based SAR measurements.

information can be seen to fall within ±5.75 m/s.

The formation of SAR imagery requires compression of targets in the azimuth domain, which inherently involves integration. As a result, the ripple-like pattern is seen to manifest along the range domain in the processed SAR image of Figure 3.28. This image was formed using a range-Doppler SAR processor known as G2 [73]. The same RGB colour mapping as Figure 3.26 has been applied, once again revealing the cross-polar response of the 45° dihedral. Azimuth integration gain improved the SNR to a point that the sphere reflector is faintly visible in the image. Furthermore, all reflectors are correctly offset from one another by 10 m in range and azimuth. The rugby posts on the northern edge of the field are not present in the image, however, despite being visible in the RTI of Figure 3.26. This is because the experiment stopped before the minimum of each post's associated hyperbolic curve was reached.

3.7.2 Rondebosch Common

With confidence in the system's ability to produce SAR images, the radar and experimental setup was moved to the Rondebosch Common for further captures. The southern edge of the Rondebosch Common provided a 470 m-long, flat and straight road that proved ideal for measurements. An average velocity of 5.3 m/s

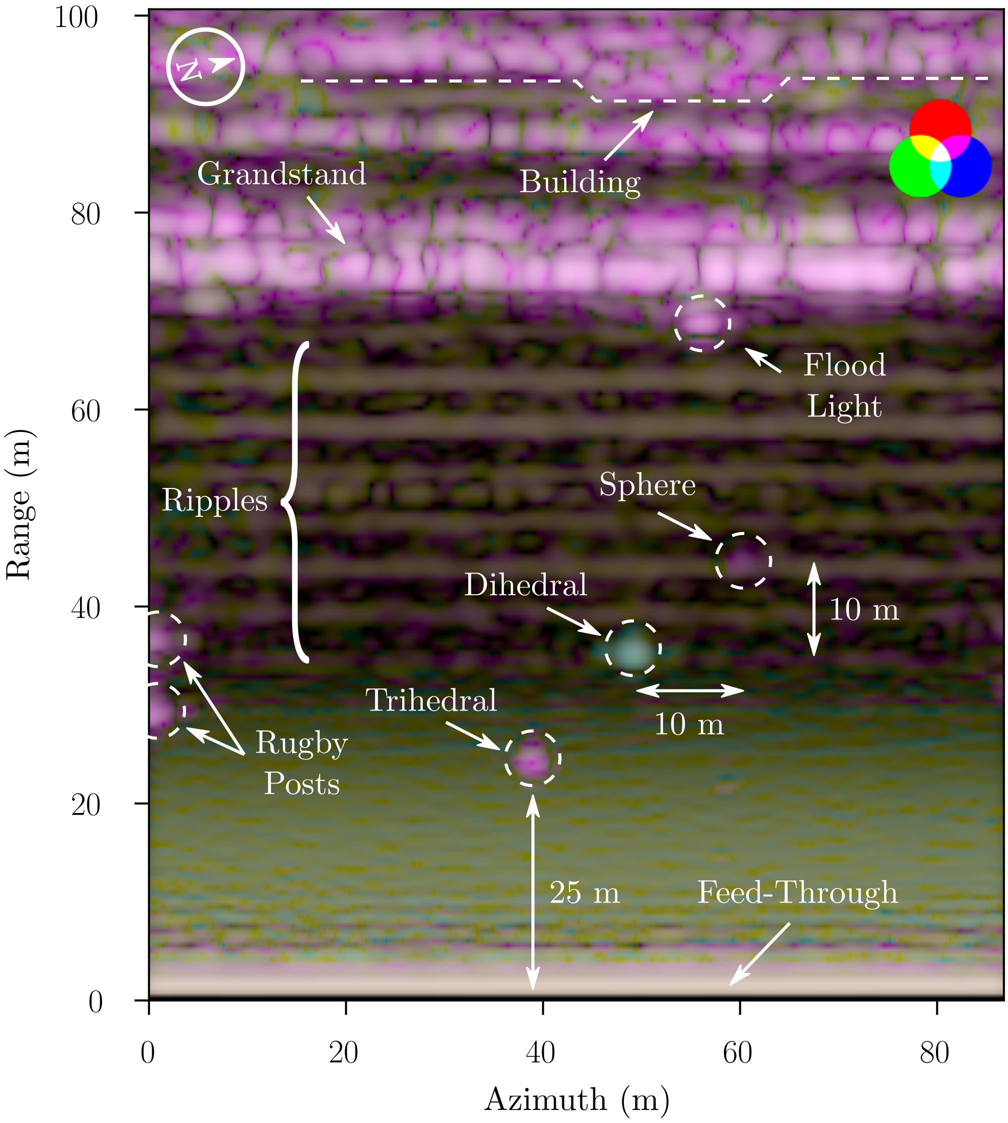

Figure 3.28: Processed polarimetric SAR image captured on the UCT rugby fields. In this image, the red channel maps to VV, the green channel represents VH, and the blue channel is the difference (VV - VH) between the two.

was maintained for these experiments, as measured using the RTK GNSS. Figure 3.29 presents an optical satellite image and the resultant SAR image over the same region of interest.

Comparison of these images demonstrates that the radar is capable of accurate detection of large trees and their associated foliage. Using the same polarisation encoding for RGB channels as before results in pink-red vertical tree trunks, while foliage is green.

Rippling interference is seen to extend throughout range, significantly deteriorating image quality and SFDR. This interference is clearly unacceptable and will be addressed in the next chapter.

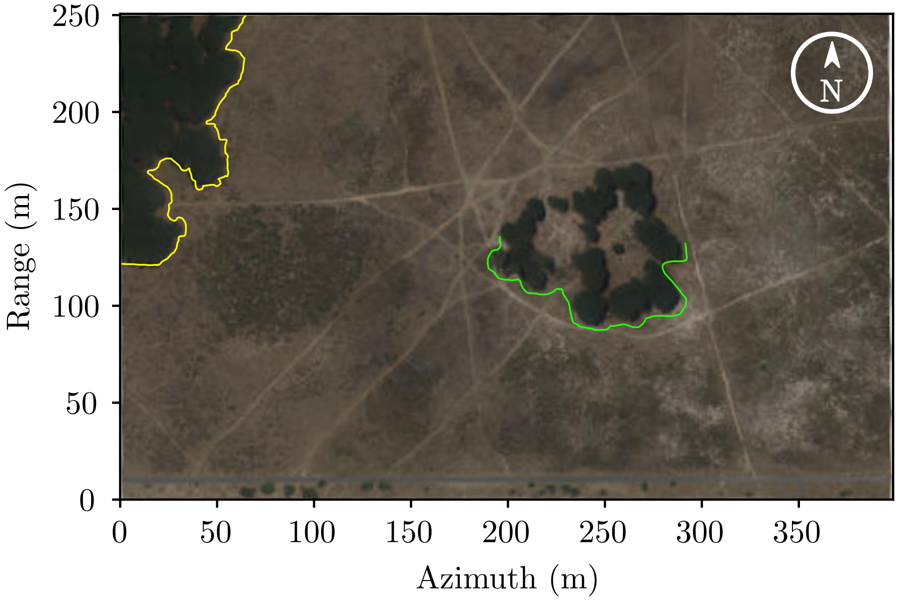

(a)

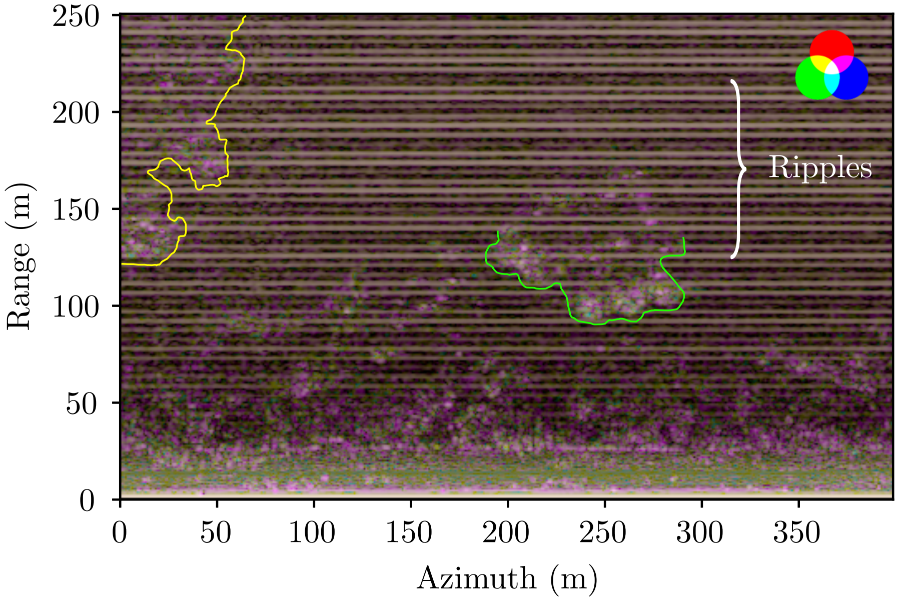

(b)

Figure 3.29: (a) Satellite image of the Rondebosch Common, retrieved from Google Earth, and (b) SAR image of the same region. The leading edge of two vegetation rich areas have been highlighted to ease comparison. While significant features can be distinguished, the SAR image is highly contaminated with ripples that extend throughout range.

3.8 Conclusions

This chapter has provided the reader with a firm background on the system's functionality and initial shortcomings, from which the following conclusions can be drawn.

The reference clock signal produced by the STEMlab was shown to exhibit a myriad of low-offset spurs that pass through the PLL loop bandwidth. These spurs are of little concern, however, because their phase varies randomly through slow-time meaning that coherent integration serves to eliminate them. Despite this, an integer-N PLL with a narrow loop bandwidth could be introduced in the future to filter out these low-offset spurs.

Implementation of custom FPGA gateware enabled the implementation of a DDC, profile pre-summer and sample chopper. In turn, this enabled the STEMlab to sustain continuous recordings at DRs less than 10 MB/s; a crucial step in the development of the SAR.

Adjustment of CPG was demonstrated to be a viable method of varying the PLL loop bandwidth. Reduction of the loop bandwidth was shown to suppress the phase noise skirt and spurs from the reference signal.

Time-offset heterodyning was shown to avoid the need for a reference channel, while enabling a variable IF. Under this configuration, the system was demonstrated to measure phase with high precision. Together these properties have answered the second research question. The time-offset approach also allowed both receiver channels to be utilised, which enabled fully polarimetric operation. Furthermore, when combined with a DDC and an analogue range gate, the variable IF was explained to enable effective feed-through suppression in varying operational conditions.

The offset of both IBS and PDH was shown to be a function of the carrier frequency, which presents a unique challenge for FMCW radars. The following chapter explores how these spurs are responsible the spurious content that was found to exist in the sideband of each target response. This same content was demonstrated to contaminate SAR imagery with ripples extending through range. The resultant reduction in image quality and SFDR was seen to be unacceptable and is thus investigated in the following chapter.

Chapter 4

Analysis of Spur Chirps

This chapter presents an investigation into the spurious content that contaminated the SAR imagery in Chapter 3. Specifically, the impact of swept-offset spurs and their manifestation at important points throughout the processing chain is explored, from the RF waveforms, to the beat signal, range profile, RDM and finally the resultant SAR imagery. As such, this chapter addresses the third research question and represents an original contribution to the literature: the identification, simulation and measurement of *spur chirps*. The objective of this work is to understand the properties of these spurs, such that guidelines for their avoidance and methods for their suppression may be developed. Aspects of this chapter are based upon the following publication:

D. A. Jordan, M. R. Inggs and M. Y. Abdul Gaffar, "Integer boundary spur considerations for fractional-N PLL based FMCW radar," *Electron. Lett.*, vol. 56, no. 14, pp. 729–732, Jul. 2020, doi: 10.1049/el.2020.0764.

4.1 The Origin of Spur Chirps

The offset of both IBS and PDH was shown in Section 3.3.2 to sweep with respect to the carrier during the course of FMCW waveform generation. This section expands on that introduction and provides the background necessary to understand how these swept-offset spurs give rise to spur chirps in the beat signal during analogue dechirp. Later, it will be shown that these spur chirps manifest as the undesirable

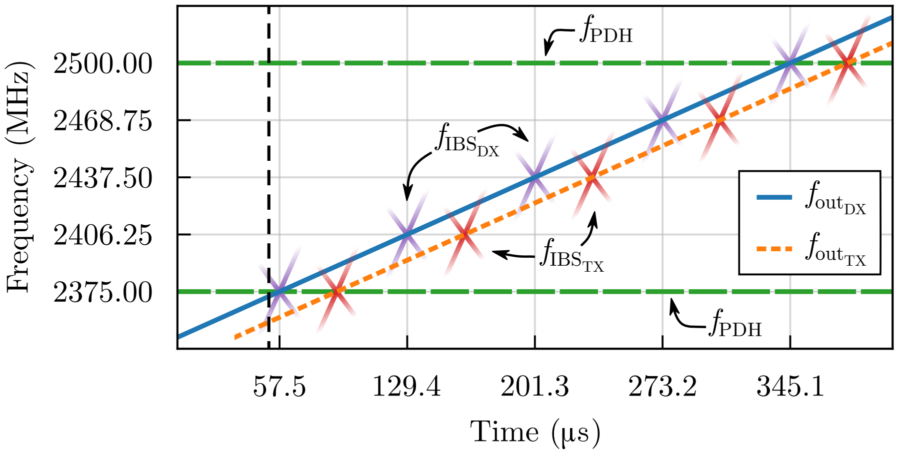

Figure 4.1: Representative spectrogram of TX and DX waveforms, including IBS and PDH. For clarity, only a single IBS ($n = 1$) is displayed. Grid ticks have been selected to coincide with integer multiples of the phase detector frequency. The IBS magnitude decreases as a function of the carrier offset. Note that the bandwidth of the PLL loop filter has been exaggerated in order to properly visualise the IBS.

ripple phenomena that was observed in the baseline performance measurements of Section 3.7. Equations 2.3 and 2.2 are repeated here for the reader's convenience.

$$f_{\mathrm{PDH}} = h f_{\mathrm{PD}}, \qquad h = 2, 3, ..., m \tag{2.3 repeated}$$

$$f_{\mathrm{IBS}} = f_{\mathrm{PD}} \left[n \frac{F_{\mathrm{n}}}{F_{\mathrm{d}}} - \mathrm{NINT}\left(n \frac{F_{\mathrm{n}}}{F_{\mathrm{d}}} \right) \right]. \tag{2.2 repeated}$$

Figure 4.1 presents a representative spectrogram of the TX and DX waveforms produced by the miloSAR. In addition to the desired carrier component (f_{out}), five regions of sweeping IBS (f_{IBS}) and two constant PDH frequencies (f_{PDH}) are associated with each waveform. Note that the PDH associated with each waveform overlap one another, and that only those IBS described by $n = 1$ in Equation 2.2 are illustrated.

The IBS are seen to produce a series of Xs in the spectrogram, which intersect with the carrier at the frequencies that were specified in Table 3.3. The X-like shape is a result of the upper and lower sideband of the IBS sweeping into and out of the PLL loop filter at several points along the FMCW ramp. As the offset of the IBS increases beyond the loop filter's cut-off frequency, the spur is suppressed.

PDH, on the other hand, are unaffected by the loop filter.

The TX and DX waveforms in Figure 4.1 are referred to throughout this chapter. They share an F_n increment value of $I = 1867$ over the $L = 50\,322$ phase detector cycles of their up-ramp. These values supplement the constrained PLL parameters that were presented in Table 3.2. The up-ramp chirp rate (β), modulation period (T_m), modulation bandwidth (Δf_out) and modulation resolution (δf_out) can be calculated as follows:

$$\beta = \frac{I f_\mathrm{PD}^2}{F_\mathrm{d} D} = 434.69\,\mathrm{GHz/s}, \tag{4.1}$$

$$T_\mathrm{m} = \frac{L}{f_\mathrm{PD}} = 402.576\,\mathrm{\mu s}, \tag{4.2}$$

$$\Delta f_\mathrm{out} = \beta T_\mathrm{m} = 174.99\,\mathrm{MHz}, \text{ and} \tag{4.3}$$

$$\delta f_\mathrm{out} = \frac{\Delta f_\mathrm{out}}{L} = 3477.55\,\mathrm{Hz}. \tag{4.4}$$

Furthermore, the waveforms are offset from one another by $L_\mathrm{off} = 2361$ phase detector cycles, which corresponds to a time offset of $t_\mathrm{off} = L_\mathrm{off}/f_\mathrm{PD} = 18.888\,\mathrm{\mu s}$ and a resultant frequency offset of $f_\mathrm{off} = \beta t_\mathrm{off} = 8.21\,\mathrm{MHz}$, which places the feedthrough signal at the lower edge of the analogue range gate.

Should the waveforms in Figure 4.1 be mixed with one another, the spurious signals associated with each waveform mix with the counterpart waveform's carrier. This is best demonstrated through assessment of the beat signal produced at a single point in fast-time. The instantaneous waveform parameters for one such point in fast-time are presented in Table 4.1, which corresponds to the black vertical dashed line in Figure 4.1.

After configuring the TX and DX PLLs according to their corresponding parameters in Table 4.1, their output spectra were measured, as presented in Figure 4.2(a). For comparison, the waveforms have been overlaid and are plotted against their offset from their respective carrier frequency. Only a single sideband is displayed, since the waveforms are symmetrical about the carrier. In this figure, the frequency offset is plotted with respect to $f_\mathrm{off} = f_{\mathrm{out}_\mathrm{DX}} - f_{\mathrm{out}_\mathrm{TX}} = 8.21\,\mathrm{MHz}$.

Note that in Figure 4.2(a), the TX waveform is more than 8.39 MHz away from the 2375 MHz IBS intersection point, while the DX waveform is only 180.663 kHz

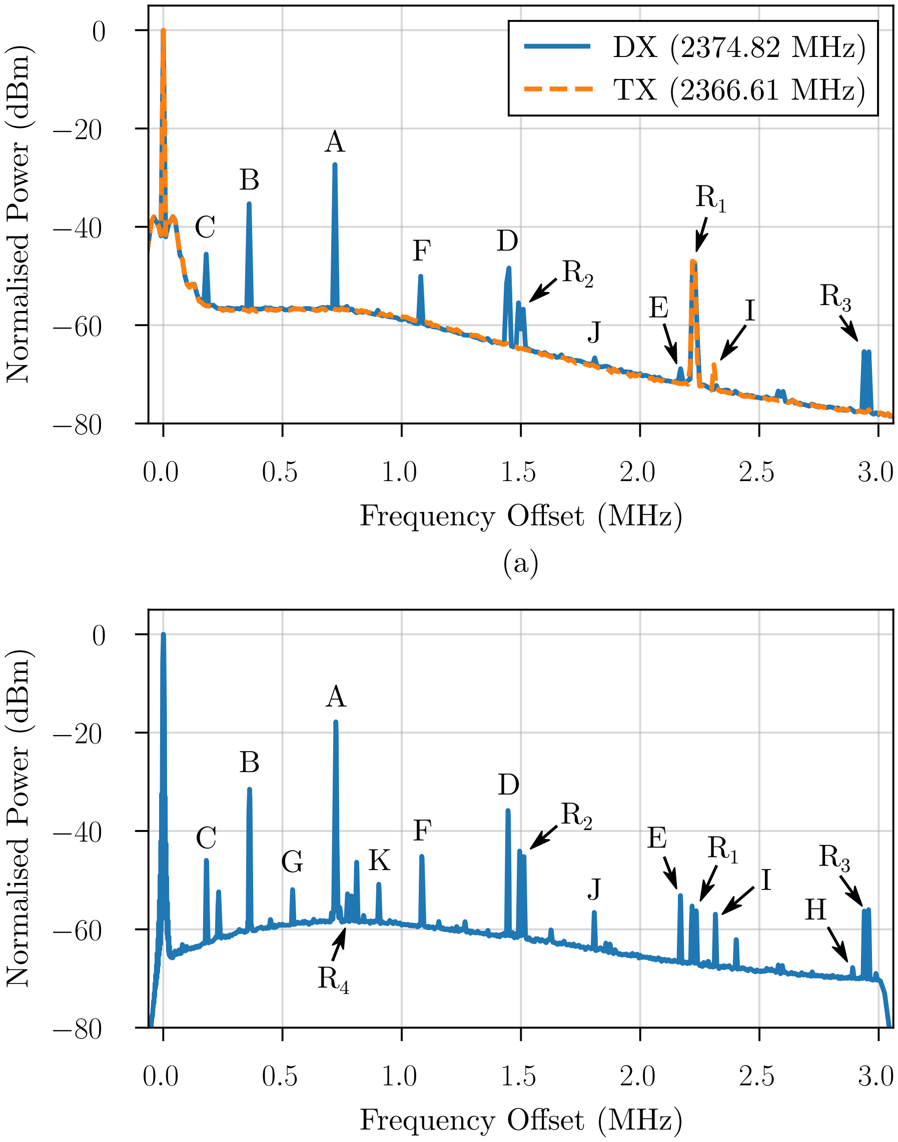

(a)

(b)

Figure 4.2: (a) Overlaid output spectra of the TX and DX waveforms that correspond to a single point in the frequency sweep. (b) Spectrum of the beat signal produced after dechirping the signals in (a). The beat signal carrier is located at 8.21 MHz, which is why spectral content near 0 Hz offset is attenuated by the analogue range gate. IBS have been labelled A–K.

Table 4.1: Instantaneous Waveform Parameters

Parameter	TX	DX	Unit
N_0	75	75	–
k	4776	7137	–
F_{n}	12 272 235	16 680 222	–
f_{out}	2366.61	2374.82	MHz
f_{VCO}	9466.44	9499.28	MHz
f_{LB}	477.8	477.8	kHz

away. Prior to the VCO divider, these offsets correspond to 33.56 MHz and 722.654 kHz respectively. As a result, only a single IBS (labelled I) appears in the TX waveform, while the DX waveform exhibits IBS labelled A–F. It can be deduced that $n = 1$ is not the only IBS present in Figure 4.2(a). The offset frequency of each IBS can be accurately predicted after modification of Equation 2.3 to include a divisor d:

$$f_{\mathrm{IBS}} = f_{\mathrm{PD}} \left[n\frac{F_{\mathrm{n}}}{F_{\mathrm{d}}} - \mathrm{NINT}\left(n\frac{F_{\mathrm{n}}}{F_{\mathrm{d}}} \right) \right] / d, \qquad d = 1, 2, 4. \tag{4.5}$$

It is hypothesised that d accounts for non-linearities produced by the VCO frequency divider, due to its inherently non-linear operation. Further work is required to test this hypothesis and to determine whether or not the values of d can be found *a priori*. Note that the values of $d = 1, 2, 4$ were determined empirically.

Table 4.2 presents the result of evaluating Equation 4.5 with the parameters in Table 4.1 for values of $n = 1, 2, ..., 5$. With the exception of $n = d = 4$, combinations of n and d that result in duplicated spurs (e.g. A*) have been excluded from the table for brevity. Table 4.2 predicts that only one IBS associated with the TX waveform will fall within the displayed RF bandwidth, confirming the observation in Figure 4.2(a).

Figure 4.2(a) further reveals that the DX waveform contains additional spurs (R_2 and R_3) that do not appear in the TX waveform. These additional spurs are generated in the same way that IBS are: intermodulation between f_{VCO} and the nearest multiple of f_{PD}, owing to substrate coupling and non-linearities in the

Table 4.2: Calculated In-Band IBS Offset Frequencies

n	d	ID	$f_{\mathrm{IBS_{TX}}}$ (MHz)	ID	$f_{\mathrm{IBS_{DX}}}$ (MHz)
1	1	–	±33.56	A	±0.72
1	2	–	±16.78	B	±0.36
1	4	–	±8.39	C	±0.18
2	1	–	±57.87	D	±1.45
3	1	–	±24.31	E	±2.17
3	2	–	±12.15	F	±1.08
3	4	–	±6.08	G	±0.54
4	1	–	±9.26	H	±2.89
4	4	I	±2.31	A*	±0.72
5	2	–	±21.41	J	±1.81
5	4	–	±10.71	K	±0.9

phase detector. They differ, however, in that they are caused by the reference signal's spurs. Stated previously, the DX waveform is 722.654 kHz away from the closest IBS intersection point, prior to the VCO divider, which matches the frequency offset measured between the reference signal's spurs (e.g. between R_2 and R_1). It can be deduced that these additional spurs sweep through fast-time in the same way that IBS do, and are therefore also spur chirps. It will be shown in Section 4.4, however, that these spurs do not present the same threat as IBS, since they are non-coherent through slow time.

Figure 4.2(b) presents the spectrum of the resultant beat signal after the RX and DX waveforms were mixed and filtered under the standard dechirp procedure. For this measurement, a short loop-back cable ($\approx$ 60 cm) was connected in series with a 50 dB attenuator between a single set of TX and RX antenna ports. This experimental configuration enabled emulation of the feed-through signal, following suppression by inter-antenna isolation. For the purposes of this analysis, the time offset due to the loop-back cable ($\approx$ 3 ns) was neglected. As such, Figure 4.2(b) can be considered the result of dechirping the tones of Figure 4.2(a).

Comparison of Figures 4.2(a) and 4.2(b) reveals that dechirp does not alter the spur offsets. Furthermore, the phase noise skirt near 0 Hz offset is suppressed in 4.2(b). This is the combined result of attenuation due to the IF BPF used as an analogue range gate, and the range correlation effect. Phase noise in the reference signal (shared by the TX and DX PLLs) is partially correlated in the RF waveforms and is therefore cancelled during mixing [74], according to

$$C = 4\sin^2(\pi f \tau_d). \tag{4.6}$$

This cancellation reveals the presence of predicted IBS that were previously masked by phase noise, namely G, K and H. The unlabelled spurs in Figure 4.2(b) are due to intermodulation during mixing.

The reader is reminded that Figure 4.2(b) reflects the state of the beat spectrum at only a single point in fast-time. Synthesis of the TX and DX FMCW waveforms, requires that the fractional numerator of each PLL be adjusted through fast-time. As a result, the carrier-offset of each waveform's IBS and PDH changes at every point along the waveform, while the nominal frequency difference between waveforms remains constant. In this way, the spurs in Figure 4.2(b) sweep over the IF bandwidth (possibly several times) during fast-time, producing undesirable *spur chirps* in the beat signal.

4.2 Manifestation in the Beat Signal

The manifestation of spur chirps in the beat signal is now revealed through simulated dechirp of the complete TX and DX waveforms in Figure 4.1.

The time period between each of the five IBS intersection points (ΔT_{int}), and the time offset to the first IBS intersection point (T_{int_0}) were calculated as follows:

$$\Delta T_{\text{int}} = \frac{f_{\text{PD}}}{\beta D} = 71.9\,\mu\text{s}, \tag{4.7}$$

$$T_{\text{int}_0} = \Delta T_{\text{int}} \left(1 - \frac{F_{\text{n}_0}}{F_{\text{d}}}\right) = 57.5\,\mu\text{s}. \tag{4.8}$$

These values, along with the illustration in Figure 4.1, suggest that the 18.888 µs time offset between the TX and DX waveforms is large enough to ensure that the spur chirps produced by each waveform will be distinguishable in fast-

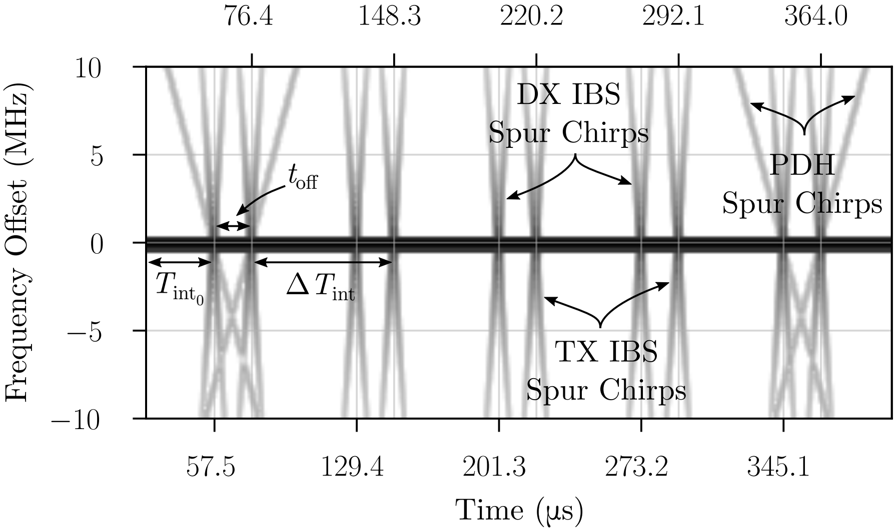

Figure 4.3: Spectrogram of the simulated beat signal plotted over an IF bandwidth of 20 MHz. Note that for homodyne systems, the intra-pair spacing t_{off} is greatly reduced. Spur chirps due to the PDH can be seen to intercept the first and fifth pairs of IBS spur chirps.

time. This is contrary to a typical homodyne scenario, where the time difference between waveforms would be far smaller and the spur chirps would mostly overlap in fast-time.

For the simulation, analytic representations of the TX and DX waveforms were passed through a PLL loop filter matched to that of the LMX2492EVM. Following mixing, no LPF was required to extract the beat signal, a benefit of using of analytic expressions. By avoiding a LPF, the spur chirps could be visualised over 20 MHz of IF bandwidth. Note that in practice, however, the maximum spur offset is determined by the radar's IF filter bandwidth, which is far smaller than the maximum IBS offset of $\pm f_{\text{PD}}/2$. For illustrative clarity, only IBS corresponding to $n = d = 1$ were simulated. The resultant spectrogram of the simulated beat signal is presented in Figure 4.3. Note that the y-axis in Figure 4.3 corresponds to an extension of the x-axis in Figure 4.2(b).

The reader is reminded that Figure 4.3 is the result of dechirping the TX and DX waveforms of Figure 4.1. The five pairs of IBS spur chirps and two PDH spur chirps seen in Figure 4.3 are the result of mixing the f_{out}, f_{IBS} and f_{PDH} signals of Figure 4.1.

The simulated spectrogram is compared with measurement in Figure 4.4. Figure 4.4(a) is a zoomed-in region of Figure 4.3 that corresponds to the measured IF bandwidth in Figure 4.4(b). The predicted spur chirps are observable in the measured data, but are partially masked by noise. Spur chirps attributed to the PDH are not visible in Figure 4.4 owing to the limited spectral resolution and aggressive chirp rate. This comparison reveals that IBS corresponding to $n = d = 1$ offer a fair approximation of the measured spur chirps in the beat signal.

The simulations and measurements presented in this section show that the feed-through signal is responsible for generating the largest set of spur chirps to manifest in the beat signal. While an analogue range gate serves to suppress the feed-through signal's carrier, its associated spur chirps pass through the filter unscathed. The preventative feed-through suppression techniques, presented in Section 2.1.1, would therefore be more effective than their curative counterparts at suppressing these spur chirps.

Having assessed the manifestation of spur chirps in the dechirped beat signal, the following section investigates their representation in the range domain.

4.3 Fresnel Ripples in the Range Domain

Following dechirp, the time-domain beat signal is transformed into the frequency domain through an FFT. This transform compresses each beat frequency into a sinc function, but also spreads each spur chirp throughout the IF bandwidth in the form of *Fresnel ripples* [75, 76].

Each IBS-induced spur chirp can be considered an FM waveform with saw-tooth modulation. Linear segments of the saw-tooth waveform are expressed as:

$$s(t) = \cos\left(\omega_0 t + \frac{\mu t^2}{2}\right), \qquad -\frac{T}{2} < t < \frac{T}{2}, \tag{4.9}$$

where $\omega_0 = 2\pi\beta t_{\text{off}}$, $\mu = 2\pi D\beta(n/d)$ and $T = 2\pi f_{\text{PD}}/\mu$.

Note that the radian modulation rate (μ) of the $n = d = 1$ spur chirp is a factor of D larger that β. This is because (as noted in Section 3.3.2) the VCO divider does not change the carrier offset of spurs and only reduces their magnitude.

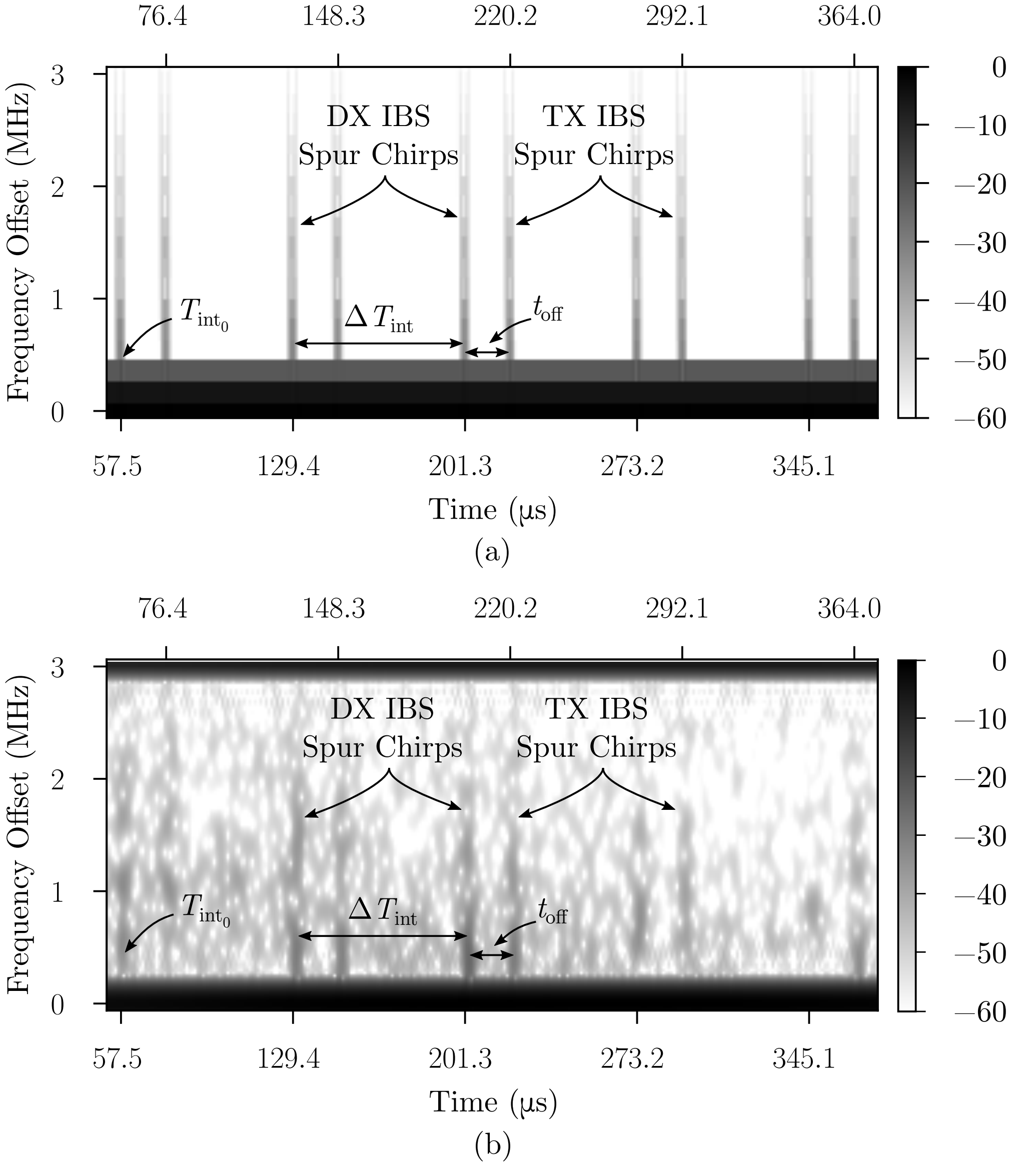

Figure 4.4: Spectrograms of the (a) simulated and (b) measured beat signal. Spectral resolution is limited owing to the small observation period available for each Short-Time Fourier Transform (STFT). Signal power has been normalised and is displayed over 60 dB of dynamic range. The spur chirps clearly manifest at the predicted time offsets and match the simulation.

A closed-form solution for the Fourier transform of $s(t)$ is given by [76]:

$$S(\omega) = \frac{1}{2}\sqrt{\frac{\pi}{\mu}} \exp\left[-j\left(\frac{(\omega-\omega_0)^2}{2\mu}\right)\right]\left[C(X_1) + jS(X_1) + C(X_2) + jS(X_2)\right], \tag{4.10}$$

where

$$X_1 = \frac{\frac{\mu T}{2} + (\omega - \omega_0)}{\sqrt{\pi\mu}}, \qquad X_2 = \frac{\frac{\mu T}{2} - (\omega - \omega_0)}{\sqrt{\pi\mu}} \tag{4.11}$$

and

$$C(X) = \int_0^X \cos\left(\frac{\pi y^2}{2}\right) \mathrm{d}y, \qquad S(X) = \int_0^X \sin\left(\frac{\pi y^2}{2}\right) \mathrm{d}y. \tag{4.12}$$

Note that Equation 4.10 describes only the positive half of the spectrum and was derived under the assumption that the chirp centre frequency is much larger that its bandwidth [76].

Equation 4.12 contains the Fresnel integrals, which describe the ripples that occur in the magnitude of $S(\omega)$:

$$|S(\omega)| = \frac{1}{2}\sqrt{\frac{\pi}{\mu}}\sqrt{\left[C(X_1) + jS(X_1) + C(X_2) + jS(X_2)\right]^2} \tag{4.13}$$

Equation 4.13 was evaluated for $n = d = 1$ to produce the spectrum presented in Figure 4.5. To reiterate, this figure illustrates only the positive half spectrum of a FM waveform, modelled after a single linear segment of the saw-tooth spur chirp waveform. As such, its only purpose is illustrate the presence of Fresnel ripples, since the derivation of a closed-form solution for the Fourier transform of a saw-tooth spur chirp waveform is beyond the scope of this thesis.

As seen is Figure 4.5, the chirp bandwidth is far greater than the IF, which defies the conditions under which Equation 4.10 is valid. This violation distorts the period of Fresnel ripple oscillations in the frequency domain, which was measured as $2\delta f_{\mathrm{VCO}}$. The true period of these oscillations is δf_{VCO}, as revealed in Figure 4.6 which presents the Fourier transform of the simulated and measured beat signals, from Figures 4.3 and 4.4 respectively.

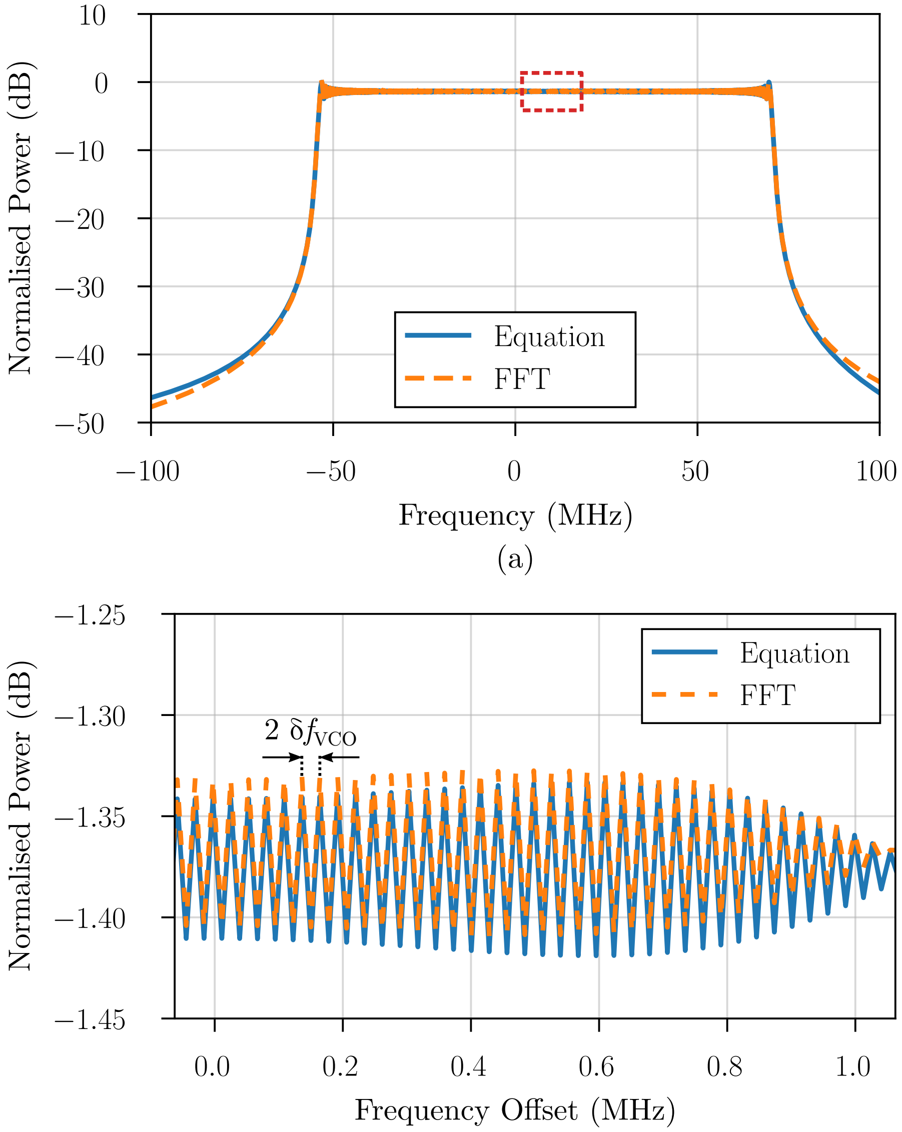

(a)

(b)

Figure 4.5: (a) Positive half spectrum of a single spur chirp centred at 8.21 MHz. (b) Fresnel ripples in the magnitude of the linear chirp's spectrum, plotted versus frequency relative to 8.21 MHz. The red dashed box in (a) corresponds to the region displayed in (b). In addition to Equation 4.13, the magnitude of the spectrum produced through an FFT of an equivalent chirp is provided for validation.

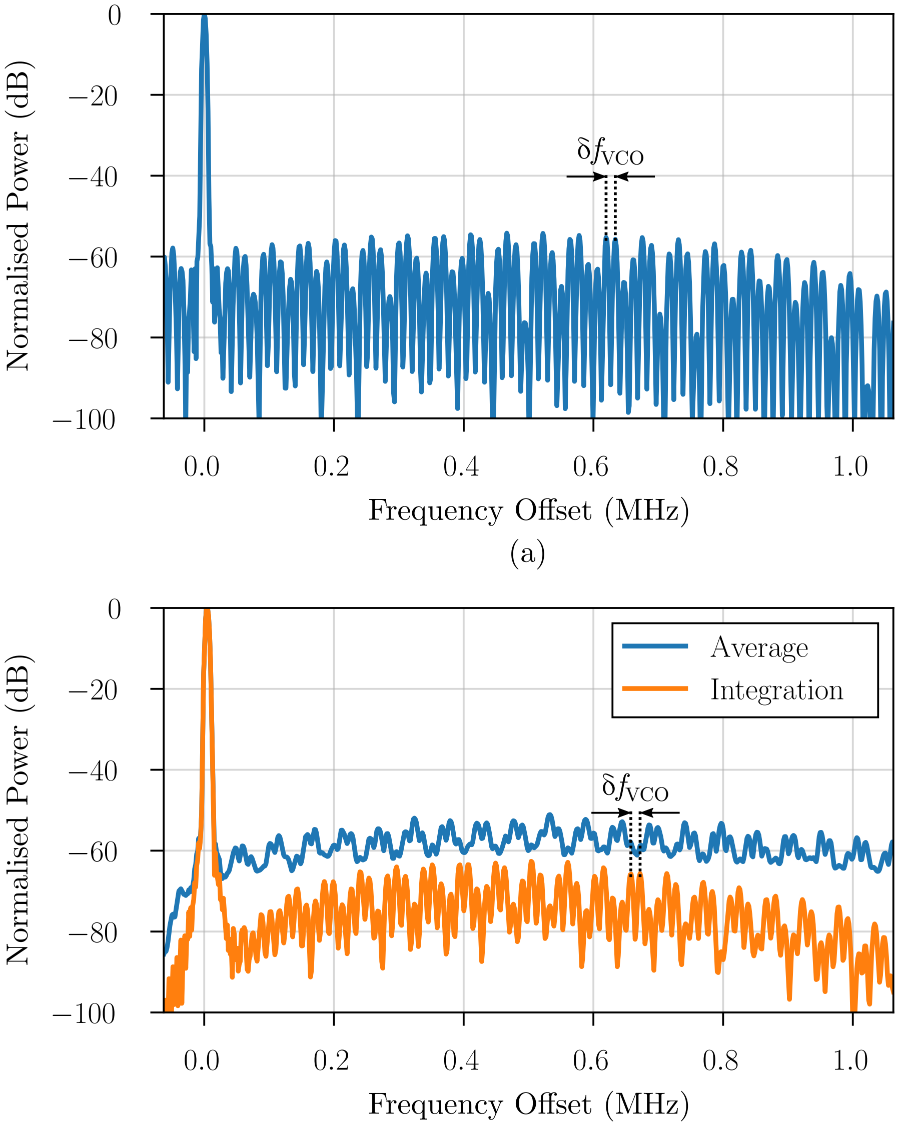

(a)

(b)

Figure 4.6: Spectrum of the (a) simulated and (b) measured beat signal, where Fresnel ripples are seen to oscillate with a period of δf_{VCO} over the IF bandwidth. The measured spectrum in (b) is the same as that which was presented in Section 3.6.6, and presents both the non-coherent average, and coherent integration of 1000 profiles. The discrepancy in spur power levels between (a) and (b) near 0 Hz offset is attributed to the lack of the analogue range gate in the simulation.

At this point, it is insightful to refer back to Figure 4.2(b), which presented the beat signal spectrum at a single point in fast-time and investigated the visible spurs. The results in Figure 4.6 can be interpreted as the superposition of the spurs in Figure 4.2(b) as they sweep over all frequency offsets.

As noted previously, the integration trace in Figure 4.6(b) shows that the spur chirps exhibit some degree of coherency over slow-time. This is investigated in the section that follows, where the manifestation of spur chirps in the Doppler domain is assessed.

4.4 Aliased Doppler Frequency

Equations 2.2 and 2.3 show that both f_{PDH} and f_{IBS} are functions of f_{PD}. During dechirp, these spurii mix with f_{out} (which is also a function of f_{PD}) to produce spur chirps. The aliased Doppler frequency of these dechirped spurs can be predicted, to produce a synthetic RDM. To illustrate this, the single point in fast-time that was analysed in Section 4.1 is now revisited.

It is important to remember that the analysis of a single point in fast time requires that each PLL generate a tone, offset relative to the other by $f_{\mathrm{off}} = 8.21\,\mathrm{MHz}$. The resultant beat frequency is not an integer multiple of the 1250 Hz PRF. As a result, the carrier does not appear at zero Doppler frequency, but is rather aliased to $f_{\mathrm{AD}}(8\,210\,516.093\,\mathrm{Hz}) = 516.093\,\mathrm{Hz}$, where:

$$f_{\mathrm{AD}}(f) = f - \mathrm{NINT}\left(\frac{f}{\mathrm{PRF}}\right)\mathrm{PRF}. \tag{4.14}$$

Similarly, the aliased Doppler frequency of every IBS in Table 4.2 can be calculated using Equation 4.14, but must be adjusted for the Doppler offset of the carrier. Table 4.3 presents the calculated aliased Doppler frequency for each IBS that appears in the IF bandwidth.

Figure 4.7(a) presents the calculated values of Table 4.3 in the form of a synthetic RDM, for comparison with a measured RDM in Figure 4.7(b).

Note the presence of reference signal's spurs $R_1 - R_4$ in Figure 4.7(b), which correspond to the offsets observed in Figure 4.2(b). Unlike IBS, the rate of change of phase of these spurs is not deterministic through slow-time. As such, the signal

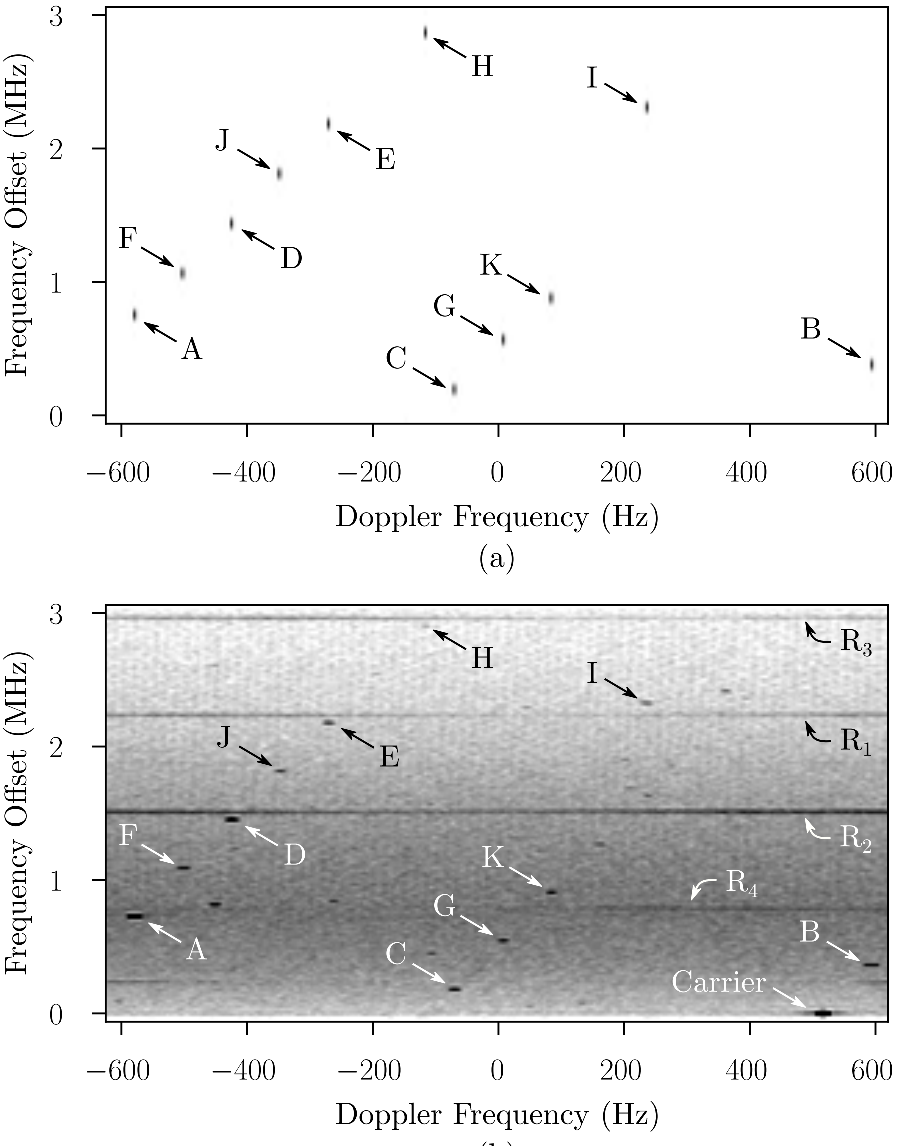

(a)

(b)

Figure 4.7: (a) Predicted and (b) measured positions of IBS in the RDM. The measured map clips the displayed signal power to values between −70 dBc and −95 dBc.

Table 4.3: Calculated Aliased Doppler Frequencies of In-Band IBS

ID	f_{IBS} (MHz)	$f_{\mathrm{AD}}(f_{\mathrm{IBS}} + f_{\mathrm{off}})$ (Hz)
A	0.72	-580
B	0.36	593
C	0.18	-70
D	1.45	-425
E	2.17	-271
F	1.08	-503
G	0.54	7
H	2.89	-117
I	2.31	235
J	1.81	-348
K	0.9	84

energy of these spurs is spread throughout Doppler, meaning that coherent integration through slow-time will cause their magnitude to reduce. The impact of these spurs can therefore be neglected in coherent integration applications, such as SAR.

The measured Doppler frequency of the carrier in Figure 4.7(b) agrees with the predicted value of 516.093 Hz to within ±0.012 Hz. Recall that a frequency-offset heterodyne configuration would experience this same Doppler offset, while a time-offset does not.

Figure 4.8 presents the measured RDM for a complete up-ramp (e.g. all points through fast-time), corresponding to the beat signal which was used to produce Figure 4.6(b). This map was formed by averaging several individual range-Doppler frames, each produced using 512 range profiles.

Figure 4.8 reveals that the spur chirps appear throughout the range at fixed Doppler frequencies, forming vertical interference lines. The Doppler frequency at which each spur appears, however, could not be accurately predicted.

While this form of interference could be detrimental for a number of radar applications, its impact on SAR image quality is investigated in the section that follows.

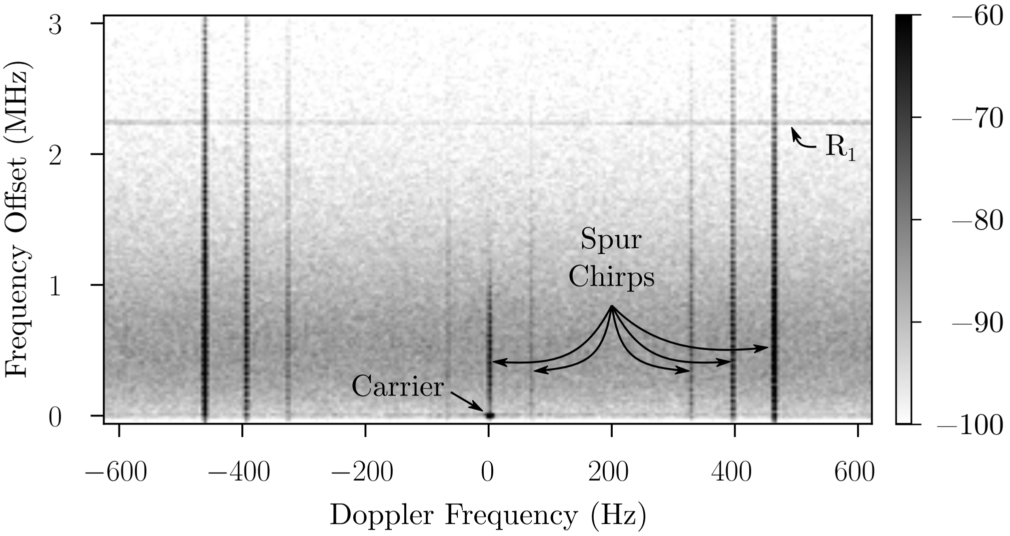

Figure 4.8: Averaged RDM, constructed from several range-Doppler frames of 512 profiles. A dynamic range of −60 dBc to −100 dBc has been presented.

4.5 Effect on SAR Imagery

In an ideal SAR scenario, each stationary point target traces a range-dependent hyperbolic curve in the range-Doppler domain through slow-time. This is exploited during azimuth compression, where the deterministic phase history of each target is adjusted such that all target energy within the processed Doppler bandwidth can be coherently integrated. Unfortunately, the manifestation of spur chirps at zero Doppler means that the compressed response of each target becomes corrupted by spur chirps during this integration step. This section assesses the nature and extent of this interference through simulation.

The Flexible Extensible Radar Simulator (FERS) [77] was used to simulate a pseudo-monostatic FMCW radar whose waveform parameters match those used throughout this chapter. In this simulation, the radar maintained a constant velocity of $v = 30\,\mathrm{m/s}$ at an altitude of $h = 1\,\mathrm{m}$, while illuminating a single stationary point target at a ground range of $R_{\mathrm{g}} = 50\,\mathrm{m}$. This geometry is illustrated in Figure 4.9, where the green and red markers indicate the start and stop positions of the radar respectively.

The TX and RX antennas were modelled to have an isotropic radiation pattern and were separated by $R_{\mathrm{sep}} = 0.5\,\mathrm{m}$. Transmission at a power level of $P_{\mathrm{TX}} = 10\,\mathrm{dB}$

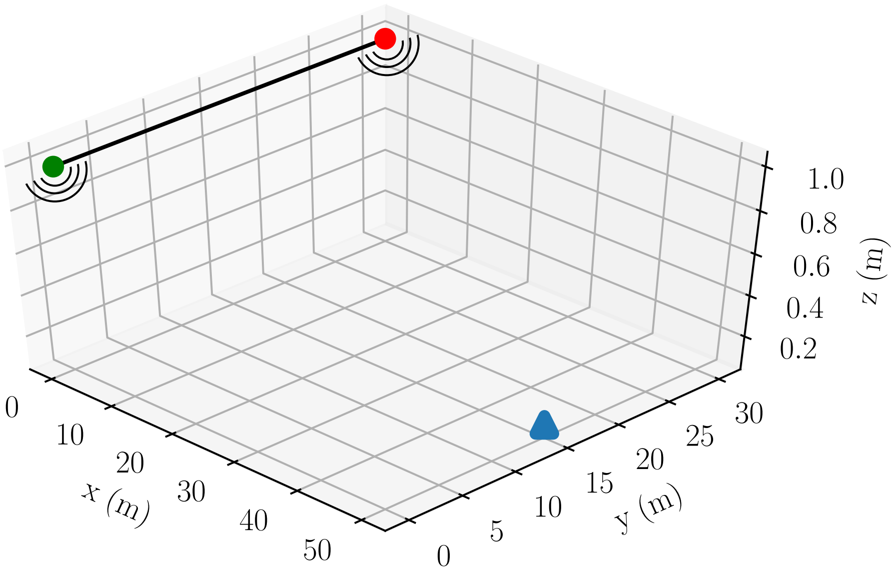

Figure 4.9: Geometry of the simulated SAR scene. The radar travels along the black line from the green to the red marker. The target is represented by the blue triangle.

therefore resulted in a feed-through signal power level of

$$P_{\mathrm{FT}} = P_{\mathrm{TX}} - 20\log_{10}\left(4\pi\frac{R_{\mathrm{sep}}}{\lambda}\right) + 30 = 5.83\,\mathrm{dBm}. \tag{4.15}$$

The system temperature was set at $T_{\mathrm{s}} = 5\,\mathrm{MK}$, which resulted in a noise power density of

$$P_\rho = 10\log_{10}(kT_{\mathrm{s}}) + 30 = -131.61\,\mathrm{dBm/Hz}. \tag{4.16}$$

This artificial value of T_{s} was specifically chosen such that the resultant noise power density matched that of the STEMlab, as was measured in Figure 3.16. This density can be multiplied by the receiver's ENBW of 4560 Hz to reveal the expected level of the noise floor:

$$P_{\mathrm{N}} = P_\rho + 10\log_{10}(4560) = -95\,\mathrm{dBm} \tag{4.17}$$

Figure 4.10 presents a simulated range profile, prior to the inclusion of any targets or spur chirps. This figure serves to validate the basic simulation config-

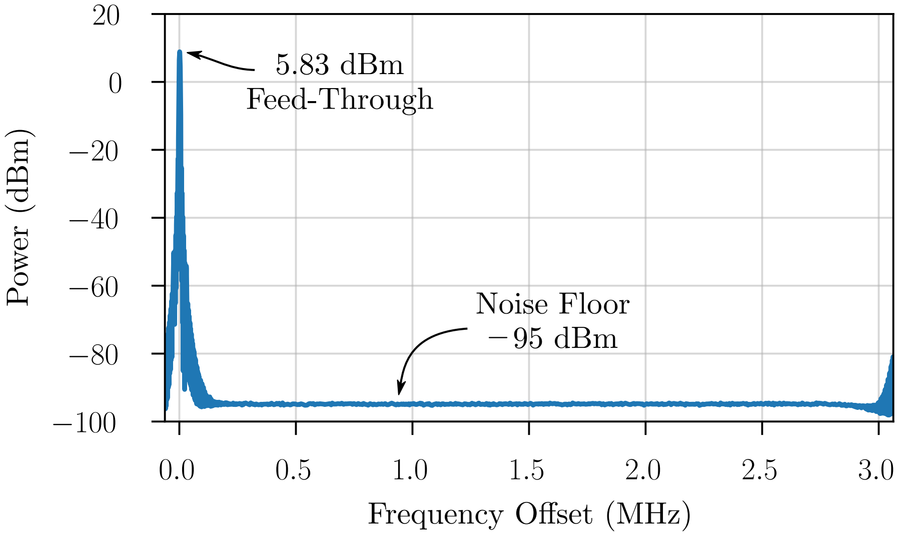

Figure 4.10: Simulated range profile, illustrating the feed-through signal power and noise floor level.

uration and confirms the predicted values for the feed-through signal power and noise floor level.

Following dechirp, a set of spur chirps were added to the beat signal at a level of $-47\,\mathrm{dB}$ relative to the feed-through signal. For simplicity, the spur chirps were simulated to manifest in only the zero Doppler bin. This is an acceptable simplification to make, since only the spectral content that falls within the processed Doppler bandwidth is of concern during azimuth compression. To achieve a desired azimuth resolution of $\delta_{\mathrm{az}} = 0.745\,\mathrm{m}$, a Doppler bandwidth of $B_{\mathrm{az}} = v/\delta_{\mathrm{az}} = 40\,\mathrm{Hz}$ was required. Referring back to Figure 4.8, it can be seen that only the zero-Doppler spur chirps fall within the processed bandwidth.

The stationary target was modelled as an isotropic point scatterer with an RCS of $50\,\mathrm{m}^2$. The power received from this target can be calculated as follows:

$$P_{\mathrm{RX}} = 10\log_{10}\left(\frac{P_{\mathrm{TX}}\lambda^2\sigma}{(4\pi)^3 R_{\mathrm{s}}^4}\right) + 30 = -62.15\,\mathrm{dBm}, \tag{4.18}$$

where $R_{\mathrm{s}} = \left(h^2 + R_{\mathrm{g}}^2\right)^{0.5}$ is the minimum slant range to the target. To find the target's resultant SNR, the processing gain afforded by azimuth compression must be accounted for. The number of pulses to be integrated through slow-time varies as a function of slant range according to:

$$N_{\mathrm{az}} = 2R_{\mathrm{s}} \tan\left[\arcsin\left(B_{\mathrm{az}}\frac{\lambda}{4v}\right)\right]\frac{\mathrm{PRF}}{v} = 171. \tag{4.19}$$

As such, the target's SNR after azimuth compression was predicted to be

$$\mathrm{SNR} = P_{\mathrm{RX}} - P_{\mathrm{N}} + 10\log_{10}(N_{\mathrm{az}}) = 55.18\,\mathrm{dB}. \tag{4.20}$$

The processed simulation results are presented in Figure 4.11, where each column contains a SAR image, azimuth slice, and range slice of the point target's response for different experimental conditions. The first column serves as a control: the ideal case in which no spur chirps were present in the beat signal, while the second column presents the case of spur chirps present at a level of $-47\,\mathrm{dB}$ relative to the feed-through signal. These images were processed using a range-Doppler SAR processor known as G2 [73].

Comparison of the results in these columns reveals the extent to which spur chirps corrupt SAR imagery. The Fresnel ripples (discussed in Section 4.3) appear as the horizontal interference lines seen in Figure 4.11(b) and the ripples throughout range in 4.11(f). Furthermore, the sidelobes of the azimuth slice in 4.11(d) are greatly increased owing to the integration of spur chirp signal energy in the ripples.

Three metrics were used to quantitatively analyse of the impact of the spur chirps, namely: PSLR, RMSE, and SSIM. PSLR quantifies the ability of a SAR to distinguish between closely spaced targets whose magnitude differ significantly. RMSE provides a measure of the *absolute* difference between resultant SAR images, and SSIM quantifies the *perceived* difference between images. The results of this analysis are presented in Table 4.4. Note that while the results of Figure 4.11 were simulated in the presence of system noise, the values presented in Table 4.4 were measured without this noise. This ensured that the performance metrics assessed only the signal response, and were not tainted by noise. However, the target's large SNR value of 55.18 dB meant that the difference caused by the presence of noise is largely negligible for this assessment.

The RMSE and SSIM values agree that the spur chirps cause a significant

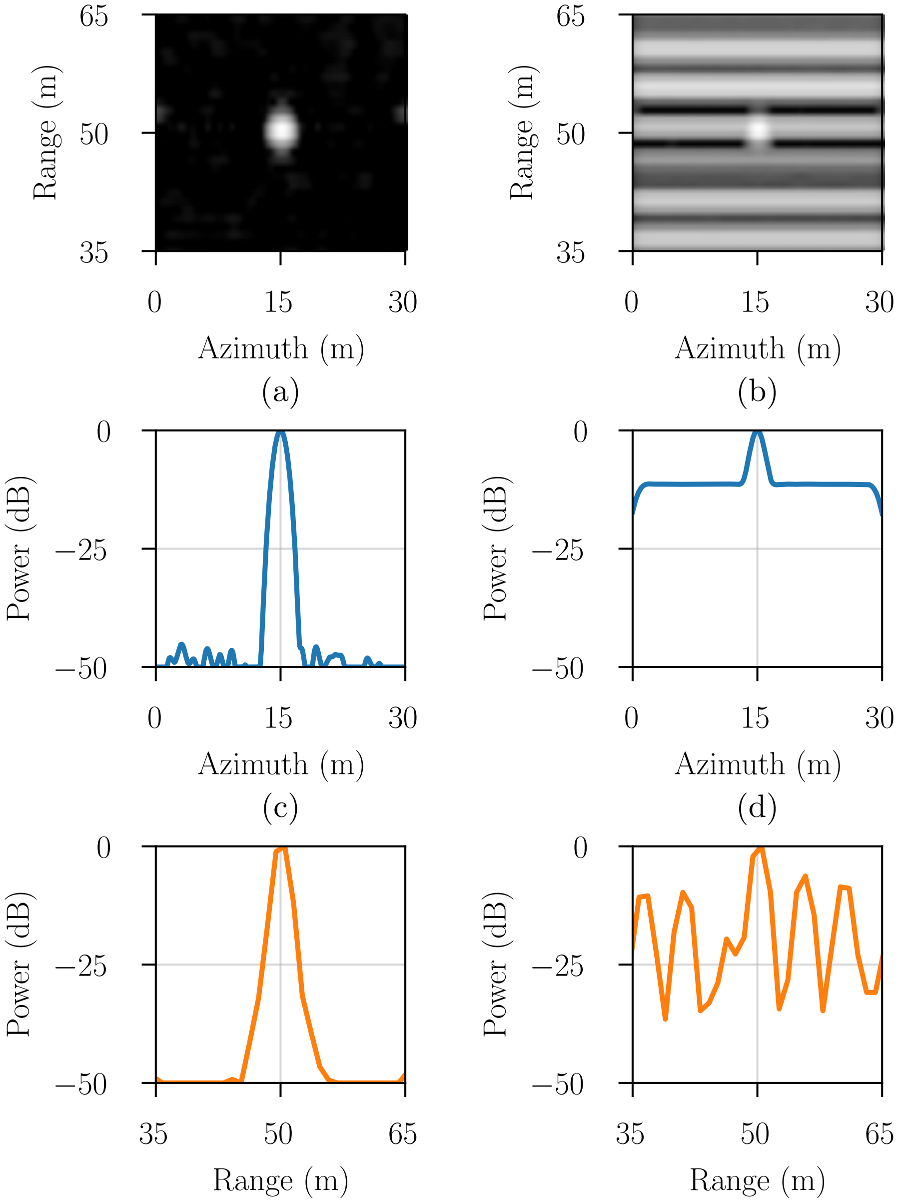

(a) (b)

(c) (d)

(e) (f)

Figure 4.11: SAR simulation results, illustrating the (a)–(b) processed SAR images, (c)–(d) azimuth slices, and (e)–(f) range slices through the simulated point target. The first column ((a), (c), (e)) serves as a control, where no spur chirps were present in the beat signal. Whereas the second column ((b), (d), (f)) contains spur chirps at a level of −47 dB relative to the feed-through signal.

Table 4.4: Assessment of PSLR, RMSE and SSIM

Performance Metric	Ideal Case	Spur Chirps	Unit
RMSE	0.00	28.61	dB
SSIM	1.00	0.02	–
PSLR (Azimuth)	47.01	11.31	dB
PSLR (Range)	47.22	4.98	dB

difference between the resultant SAR images on both an absolute and perceptual level. Furthermore, the PSLR values show that the interference manifests at a significant power level that greatly hinders the ability to distinguish the target's response from interference and other targets.

4.6 Conclusions

The work presented in this chapter has addressed the third research question by exploring the origin of spur chirps and their manifestation in the beat signal, range profile, RDM, and processed SAR image.

The precise location of spur chirps in beat signal was predicted, as demonstrated through comparison of simulated and measured data. The ability to precisely predict their position lends itself to suppression through zeroing in the time domain, as will be explored in the next chapter. While both IBS and PDH were identified as sources of spur chirps in the beat signal, it was found that IBS corresponding to $n = d = 1$ offer an acceptable approximation of their combined presence in measured data.

Spur chirps were found to manifest as Fresnel ripples in the range profile, which explained the *ripple-like* interference that was observed in the baseline measurements of Chapter 3. Analysis of the RDM revealed that these ripples appear over all range, but in specific Doppler frequency bins. As such, the spurs are sparsely represented in the range-Doppler domain, a property which is leveraged in the next chapter. Further work is required to predict the RDM frequency bins in which the interference will appear.

Simulations illustrated the devastating effect of spur chirps on processed SAR imagery, in terms of PSLR, RMSE and SSIM. This level of image degradation is unacceptable for practical applications and threatened the viability of the developed radar architecture. As such, the following chapter is dedicated to the suppression of spur chirps, using techniques based on the properties uncovered in this chapter.

Chapter 5

Avoidance and Suppression of Spur Chirps

In this chapter, mitigation of the impact of spur chirps is addressed from multiple viewpoints. First, a set of guidelines for avoiding IBS and PDH are laid out. Next, a number of mutual interference suppression techniques are identified as transferable to the problem at hand. Reduction of PLL loop bandwidth is then explored as a simple approach to IBS suppression. A novel suppression technique developed specifically for spur chirps termed RDSM is then put forward. Finally, simulations are used to compare the efficacy of time-domain zeroing, loop bandwidth reduction, and RDSM. Aspects of this chapter are based upon the following publication:

D. A. Jordan, M. R. Inggs and M. Y. Abdul Gaffar, "Suppression of spur chirps for fractional-N PLL-based heterodyne FMCW SAR," *IEEE Trans. Microw. Theory Techn.*, vol. 69, no. 1, pp. 409–417, Jan. 2021, doi: 10.1109/TMTT.2020.3030273.

5.1 Avoidance

This section contains guidelines for avoiding PDH and IBS: the root cause of spur chirps in fractional-N PLL based FMCW radars.

Firstly, PDH are avoided entirely if the radar's carrier frequency is limited to an integer multiple of $f_{\mathrm{PD}}/2$ and the modulation bandwidth is constrained to values less than $f_{\mathrm{PD}} - 2\Delta f_{\mathrm{IF}}$, where Δf_{IF} is the radar's IF bandwidth. These constraints simply confine the FMCW waveform to fall within the horizontal f_{PDH} seen in Figure 4.1. This approach to PDH avoidance is suitable for low-cost systems with moderate RF bandwidth requirements, considering that commercially available fractional-N PLLs support values of f_{PD} above 250 MHz [78, 79].

It can be shown that there are D IBS intersection points for every PDH [12]. Thus, IBS intersection points can be eliminated from the RF bandwidth if the use of an output divider is avoided. This is can be achieved through selection of a VCO which operates within the radar's desired frequency band. If no divider is employed, then the aforementioned conditions for avoiding PDH also serve to avoid IBS, for $n = d = 1$.

If the phase detector frequency and fractional numerator could be adjusted in unison during a frequency sweep, integer boundaries could be avoided entirely. PDH and IBS would therefore be eliminated with no restriction on the radar's centre frequency or bandwidth. Others have successfully employed this technique, where either an input frequency multiplier [80], or the reference frequency [53] was made programmable, enabling dynamic adjustment of the phase detector frequency. To the best of the author's knowledge, however, an implementation for swept-frequency applications has not been presented in the literature.

5.2 Transferable Suppression Techniques

Under certain conditions, the mutual interference of FMCW radars in automotive scenarios presents a similar problem to that of spur chirps. However, there are some inherent differences between these problems.

1. Spur chirps occur in every received beat signal.
2. Multiple sets of spur chirps may appear in each beat signal.
3. The time-offset, duration, sweep-rate and bandwidth of spur chirps in the beat signal are known *a priori*.
4. Spur chirps exhibit constant Doppler frequency through slow-time.

A number of techniques have recently been developed to address the problem of mutual interference. This is largely due to the increase in probability of mutual interference events as the use of radar for vehicle guidance, collision avoidance, and proximity-sensing applications is on the rise [81].

A subset of these suppression techniques is now considered for transfer to the problem of spur chirp interference. In general, these techniques are applicable but do not take advantage of the aforementioned differences, and thus do not provide an optimal solution.

5.2.1 Zeroing

Zeroing is likely the simplest approach to interference suppression, consisting of the multiplication between the beat signal and a *masking* function in the time-domain. The masking function is designed to set regions of interference to a value of zero, or taper towards and away from zero according to an inverse windowing function [82]. This way, zeroing leverages the sparsity of interference in the time-domain. In most applications, the location and duration of interference must be detected, however, these properties are known *a priori* for spur chirps.

The drawback of this technique is that each target response is convolved with the Fourier transform of the masking function. This convolution degrades target range resolution, increases sidelobe levels, and reduces SNR [83, 84]. As such, time-domain zeroing is often used as a baseline for comparison with alternative suppression techniques.

To illustrate the associated drawbacks, Figure 5.1(a) repeats the measured beat signal spectrogram from Figure 4.4(b), while Figures 5.1(b) and 5.1(c) present a boxcar masking function and its Fourier transform respectively. This masking function consists of ten zeroing regions, each 15 samples wide, which constitutes approximately 14.4 % of the total number of samples in the beat signal.

Convolution of each range profile with the function in Figure 5.1(c) is clearly undesirable. It will be seen in Section 5.5, that this convolution limits the achievable PSLR in the range domain. More sophisticated suppression techniques are presented in the Sections that follow.

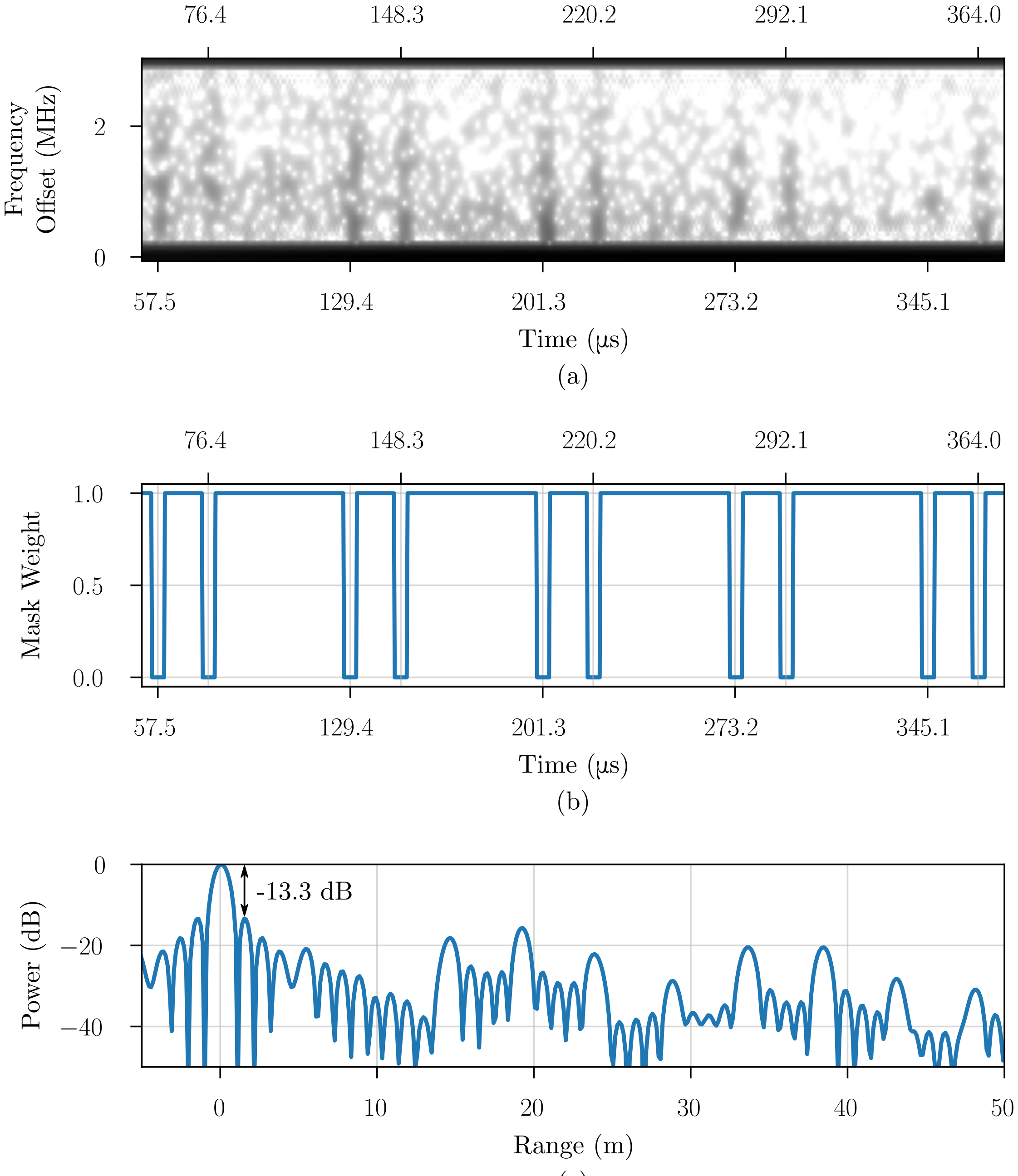

(a)

(b)

(c)

Figure 5.1: (a) Spectrogram of a measured beat signal with spur chirp interference, (b) masking function, and (c) Fourier transform of the mask. The first sidelobe was measured to appear 13.3 dB down from the mainlobe peak. Approximately 14.4 % of the total number of samples in this mask are zero valued.

5.2.2 Sparse Representation

Correas-Serrano *et al.* [85] have demonstrated the use of Orthogonal Matching Pursuit (OMP) to sparsely represent mutual interference in a reduced chirplet basis. The residual signal (following OMP) is free of interference and contains only target information. A challenge of this technique is the dictionary size. However, for the problem of spur chirps one would require a significantly smaller dictionary size since the bandwidth, time-offset, duration and modulation-rate are known *a priori*.

Alternatively, Uysal [86] has used Morphological Component Analysis (MCA) to separate both synchronous and asynchronous sources of interference. This approach is based on the sparse representation of target and interference signals in the Fourier and STFT domains respectively.

Both of the aforementioned techniques involve iterative optimisation, which is inherently computationally expensive. This is tolerable for automotive radar, since mutual interference events may occur relatively infrequently. However, since several spur chirps may manifest in every pulse, the suppression algorithm cannot be inhibitively slow.

5.2.3 Model-Based Interpolation

Neemat *et al.* [84] developed a signal model for reconstruction of contaminated portions of the beat signal in the STFT domain, using auto-regression to estimate linear prediction coefficients. Furthermore, they employed a phase matching procedure after signal reconstruction to avoid high sidelobes in the range and Doppler domains. While this technique relies largely on FFTs, the reconstruction and phase matching process required for each interferer may prove computationally intensive, making it inappropriate for the problem of spur chirps.

5.3 Loop Bandwidth Reduction

A number of authors have addressed the problem of IBS at a hardware level. Brennan *et al.*, suggested that substrate coupling (the root cause of IBS) can be cancelled using a coupled, anti-phase portion of the VCO signal [51]. Alternatively, Osmany *et al.* highlighted the importance of shielding both the VCO output and reference input [53]. Herzel *et al.* have shown that increased spatial separation and orthogonal bond-wires aids in the reduction of mutual inductance between VCO and charge pump [56]. A simpler method for the suppression of modulated spurs at a hardware level can be found, however, in the reduction of PLL loop bandwidth [87].

The PLL loop filter is implemented using discrete passive or active components. These components can be altered between design iterations, but are not easily changed once implemented. The loop bandwidth of existing implementations can, however, be adjusted using the charge pump gain in

$$f_{\mathrm{LB}} \propto \sqrt{\frac{K_{\mathrm{PD}}\, K_{\mathrm{VCO}}}{N_{\mathrm{int}}}}. \qquad \text{(3.9 repeated)}$$

The effect of the loop bandwidth reduction on synthesised RF waveforms has already been observed in Figure 3.9, where the loop filter was responsible for a dramatic reduction in the magnitude of the phase noise skirt and neighbouring spurs. However, all spurs in this figure were due to the reference signal. The mechanisms responsible for generating PDH and IBS mean that only the latter will be suppressed by the loop filter. By extension, only IBS-induced spur chirps are susceptible to this method of suppression.

To illustrate the efficacy of loop bandwidth reduction for spur chirp suppression, Figure 5.2 presents the closed-loop transfer function of the PLL loop filter and associated beat signal spectra for two CPG configurations. The beat signal spectra in Figure 5.2(b) are for the same single point in fast-time that was analysed in Section 4.1.

Figure 5.2(b) shows that reduction of the loop bandwidth is a highly effective method of phase noise and spurii suppression. The IBS labelled A was suppressed by 25 dB, matching the difference in filter gain seen in Figure 5.2(a) at an offset of 720 kHz.

A more important result for SAR applications is presented in Figure 5.3, which compares spectra of the beat signal following coherent integration of 1000 pulses. These spectra closely resemble the content that manifests in the zero Doppler range profile of the RDM. As a result, these spectra offer insight into the spur

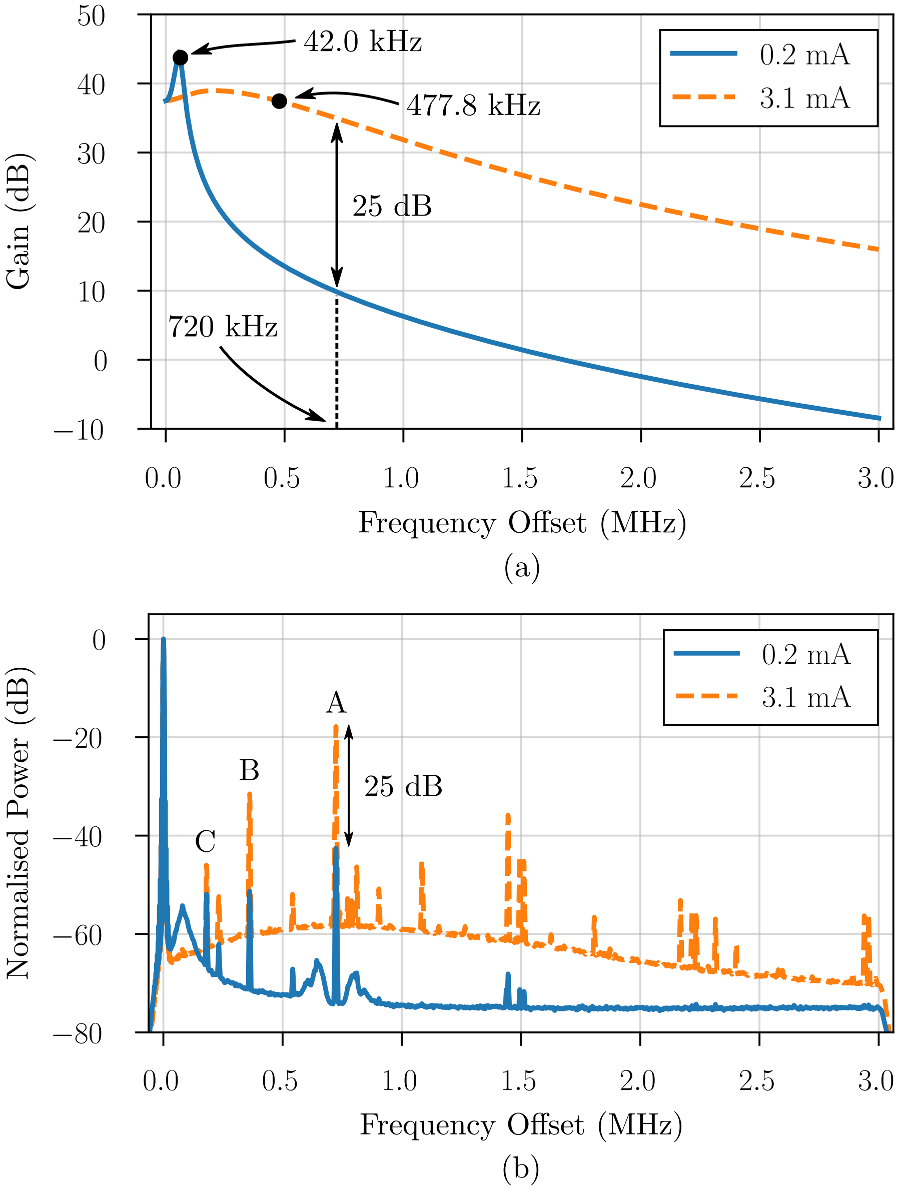

(a)

(b)

Figure 5.2: (a) Closed-loop transfer function of the PLL loop filter and (b) power spectrum of the beat signal for CPG values of 0.2 mA and 3.1 mA. These values correspond to loop bandwidths of 42.0 kHz and 477.8 kHz respectively. The loop filter has suppressed the IBS spur labelled A by 25 dB. The range correlation effect is suspected to account for a marginal disparity of ≈ 0.5 dB in this measurement.

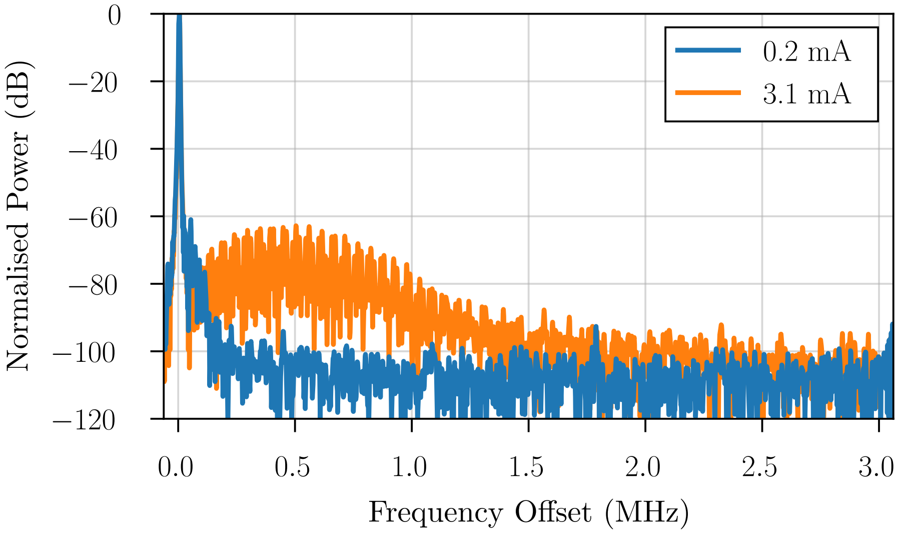

Figure 5.3: Spectra of the beat signal for CPG values of 0.2 mA and 3.1 mA following coherent integration of 1000 pulses. At an offset of 0.5 MHz there is approximately 40 dB difference between the profiles.

level expected in the processed SAR imagery.

At offsets greater than 0.25 MHz, the reduced loop bandwidth profile experiences a noise floor of −100 dB relative to the feed-through. This close-in spurious bandwidth is acceptable for airborne SAR applications, since it can be designed to fall within the empty region of range that corresponds to the platform height. Short-range ground based SAR, however, does not enjoy this advantage and the first 0.25 MHz may correspond to important targets of interest.

The efficacy of this technique must be carefully weighed-up against the inherent drawbacks of reducing the PLL loop bandwidth. Loop bandwidth has been described as the most critical design parameter of the PLL, owing to its impact on phase noise, spurs and settling time [59]. Adjustment thereof therefore carries some side-effects to be aware of. For example, loop bandwidth is inversely proportional to PLL settling time. Greater settling times decrease the radar's maximum waveform chirp rate and may degrade chirp linearity. The relationship between loop bandwidth and chirp linearity was discussed in Section 3.3.1. Furthermore, the corner frequency of the VCO high-pass transfer function is equal to the loop bandwidth. A reduction in bandwidth therefore passes more VCO noise at lower offsets and increases the radar's phase noise. In the specific case of dual fractional-

N PLL based FMCW radar, phase noise associated with the reference signal is the only source which is correlated between PLLs. This is therefore the only source of phase noise which experiences the range correlation effect [88], as was observed in Figure 4.2(b).

In FMCW radar applications, the implications of loop bandwidth reduction on PLL settling time, waveform modulation rate and chirp linearity may prove too detrimental. As such, alternative methods of spur chirp suppression are required. One such novel suppression technique is presented in the section that follows.

5.4 Range-Doppler Spur Masking

Contrary to the techniques discussed thus far, RDSM was developed specifically for the problem of spur chirp interference and takes advantage of its unique properties, as listed in Section 5.2. This led to the following set of prerequisites, which must be met for effective interference suppression.

1. Interference must exhibit constant Doppler frequency through slow-time.
2. Targets must exhibit varying Doppler frequency through slow-time.
3. Data captures should run as long as possible, such that targets transition through several range-Doppler bins.

While developed for spur chirps, these prerequisites can be met by alternative forms of interference. For example, automotive mutual interference scenarios in which the radars exhibit some degree of synchronicity [89]. Asynchronous mutual interference does not met the prerequisites, however, since it manifests as diagonal streaks in the range-Doppler domain [86].

The aim of RDSM is to separate target and interference signals in the range-Doppler domain, such that interference may be removed with minimal loss of target information. This is accomplished through a Fourier transform over all available slow-time samples. Provided the prerequisites are satisfied, this transform compresses the interference into a minimal number of frequency bins, while target information is spread throughout the range-Doppler domain. Long slow-time periods enable fine frequency resolution and therefore improve the achievable separation

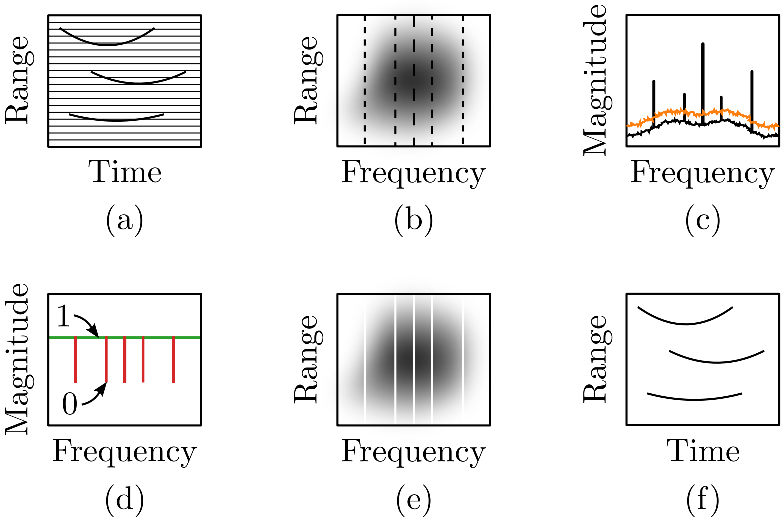

Figure 5.4: Illustrative output after each RDSM step. (a) The range-time domain is converted to (b) the range-Doppler domain using a slow-time Fourier transform. (c) The range dimension is collapsed through non-coherent averaging. (d) A mask is produced through statistics-based thresholding. (e) This mask is then applied to the RDM. (f) The result is converted back to the range-time domain through an inverse Fourier transform.

between interference and target signals. Frequency bins that contain interference are then easily identified through relative magnitude levels. Following identification, interference is eliminated through multiplication with a range-Doppler masking function. RDSM can therefore be considered a variation of the zeroing technique from Section 5.2.1. Application of a masking function in range-Doppler domain, however, offers a great advantage over the time-domain: the number of zero-valued bins constitutes a small percentage of the total number of bins. As a result, the Fourier transform of the masking function is far more amicable and exhibits reduced sidelobe levels. This is an automatic benefit for any application in which the number of slow-time samples exceeds the number of fast-time samples in the radar data cube, such as SAR. Of further benefit, a single masking function is applied to the entire data set, meaning that RDSM offers a computational advantage over the reviewed sparse representation and model-based interpolation techniques that involve iterative optimisation methods. Having gained an intuitive understanding of RDSM, its key steps are now explored in detail.

Illustrated in Figure 5.4(a), RDSM begins in the range-time domain where Fresnel ripples extend throughout each range profile as horizontal interference lines. Owing to the low magnitude level of the interference, these horizontal lines may not be visible in measured data, such as that presented in Figure 3.26. The three hyperbolic curves in this figure correspond to hypothetical targets in a SAR measurement.

The first step in the algorithm is to perform a Fourier transform over the entire slow-time axis. This produces an RDM, as presented in Figure 5.4(b). Assuming the RDSM prerequisites have been satisfied, the interference is concentrated into a limited set of frequency bins, while the target energy is spread over multiple range-Doppler bins. Compression of the interference greatly increases its magnitude with respect to all other signals in the map, due to noise, clutter and targets.

Next, non-coherent averaging is used to collapse the range dimension of the RDM. This results in a single Doppler profile with reduced signal variance, as illustrated by Figure 5.4(c). A process modelled after Constant False Alarm Rate (CFAR) detection then compares relative magnitude levels to determine which frequency bins are corrupted by interference. Frequency bins whose magnitude exceeds the CFAR threshold are selected for zeroing. A window of W data cells and G guard cells on either side of the cell under test are used to set the CFAR threshold (T),

$$T = \bar{z} + \alpha\sigma_z \tag{5.1}$$

where z is the set of $2W$ data cells after linear detection, $\bar{z}$ is the mean value, σ_z is the standard deviation, and α is a tuning parameter.

A one-dimensional frequency mask is then generated by assigning a weighting of zero to those frequency bins whose magnitude exceeds T, while all other frequency bins are assigned a weighting of unity. If desired, the mask can be modified to taper towards zero according to a windowing function. This one-dimensional mask, as presented in Figure 5.4(d), is then extended to match the original range dimension, such that the resultant two-dimensional mask can be multiplied with the original RDM to suppress interference. The masked RDM of Figure 5.4(e) can then be transformed back to the range-time domain, as seen in Figure 5.4(f), for any remaining processing steps.

Figure 5.5(a) presents a region of the averaged Doppler spectrum and associated CFAR threshold, while Figures 5.5(b) and 5.5(c) show the resultant masking function and its Fourier transform respectively. The threshold was generated using values of $W = G = 5$ and $\alpha = 10$, which were determined heuristically. This 2 s long data set contains 2500 slow-time samples and was in fact generated for the RDM in Figure 4.8. Only 34 of the 2500 samples were zeroed to form this mask, constituting 1.36 %.

The Fourier transform of RDSM masking function in Figure 5.5(c) can be compared with its counterpart for time-domain zeroing from Figure 5.1(c) because they were both developed for the same measured data from Chapter 4. While approximately 14.4 % of the samples in the time-domain masking function were zero valued and the first sidelobe of its transform appeared 13.3 dB down from its mainlobe peak, its RDSM counterpart measured comparative values of 1.36 % and 37.3 dB respectively. This comparison suggests that RDSM may prove more effective than zeroing, even for a relatively low total number of slow-time samples. The next section presents simulations that compare some of the discussed suppression techniques.

5.5 Quantitative Comparison of Techniques

This section presents simulations that quantitatively compare zeroing, loop bandwidth reduction and RDSM for the suppression of spur chirps in the same low-altitude SAR scenario that was presented in Section 4.5.

To recap, FERS [77] was used to simulate a pseudo-monostatic radar that maintained a constant velocity of 30 m/s while illuminating a single stationary point target at a minimum ground range of 50 m. A set of spur chirps were added to the beat signal at a level of −47 dB relative to the feed-through peak, in only the zero Doppler bin. Under the simulated conditions, 40 Hz of Doppler bandwidth was processed to achieve an azimuth resolution of 0.745 m.

In this Section, the masking function used to assess time-domain zeroing, along with its associated Fourier transform, are identical to those presented in Figures 5.1(b) and 5.1(c) respectively, because the simulated waveform parame-

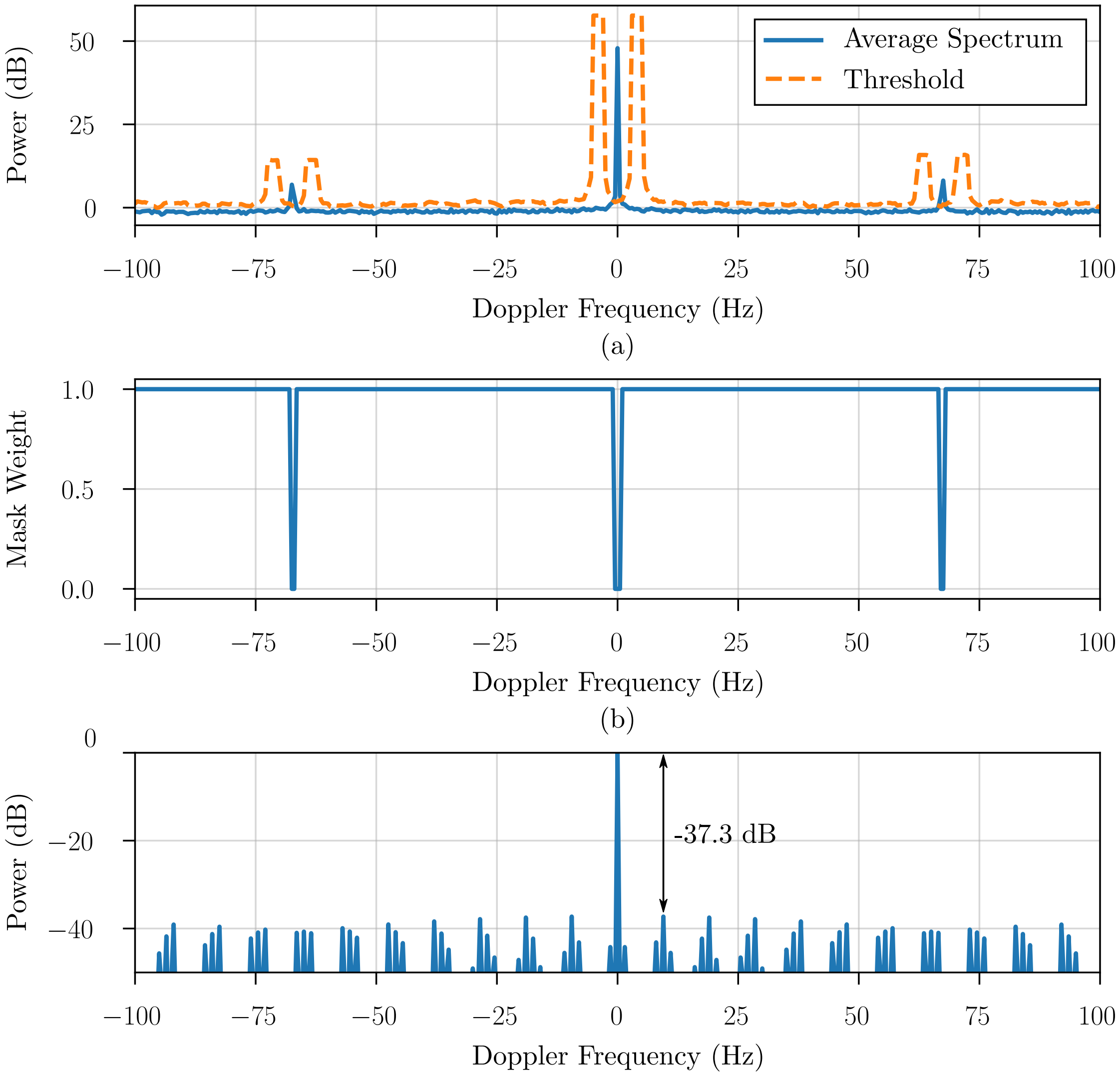

(a)

(b)

(c)

Figure 5.5: (a) Zoomed-in region of the averaged Doppler spectrum and associated CFAR threshold T, (b) associated RDSM masking function and (c) Fourier transform of the masking function.

ters match those of the miloSAR. Similarly, the PLL loop filter transfer functions presented in Figure 5.2(a) are used in this section to assess loop bandwidth reduction. On the other hand, the RDSM masking function varies as a function of the number of available slow-time samples. As such, the efficacy of RDSM was assessed for two different slow-time periods.

Available compute resources limited the extent of slow-time to a maximum of 2 s, which in turn limited the theoretical 3 dB frequency resolution of the RDSM masking function to $0.89/2 = 0.445$ Hz. As a result, RDSM discards only $0.445/40 = 1\,\%$ of the processed Doppler bandwidth for the case of 2 s of slow-time, since spur chirp interference was only present in a single Doppler bin.

Figure 5.6 presents the processed simulation results over a dynamic range of 50 dB relative to the point target's peak value. Each column consists of a zoomed-in region of the SAR image and slices through the target's response in the azimuth and range dimensions. The first column (Figure 5.6(a), 5.6(g) and 5.6(m)) serves as a baseline, where no form of spur chirp suppression was applied. Time-domain zeroing was implemented to produce the results in the second column. The simulated PLL loop bandwidth was minimised for the third column. The fourth and fifth columns present the results of RDSM for slow-time periods of 1 s and 2 s respectively. The final column serves as the ideal case in which no form of suppression was applied, and no spur chirps were introduced into the beat signal.

Comparison of the processed SAR images in Figures 5.6(a)–(f) reveals that none of the implemented techniques were able to completely eliminate the spur chirps. Fresnel ripples are still visible in the SAR images after the application of time domain zeroing and loop bandwidth reduction, but have been removed from those corresponding to RDSM. The azimuth slices in Figures 5.6(g)–(l) reveal that zeroing and RDSM exhibit the lowest sidelobe levels. Furthermore, the performance of RDSM in the azimuth slice is seen to improve from Figure 5.6(j) to 5.6(k) as the number of available slow-time samples was doubled. However, the true advantage of RDSM is evident in the range slices of Figures 5.6(m)–(r), where the sidelobe levels following RDSM are seen to approximate those of the ideal case. Table 5.1 presents the calculated PSLR, RMSE and SSIM values for each suppression technique relative to the ideal case, to enable quantitative analysis of the simulation results.

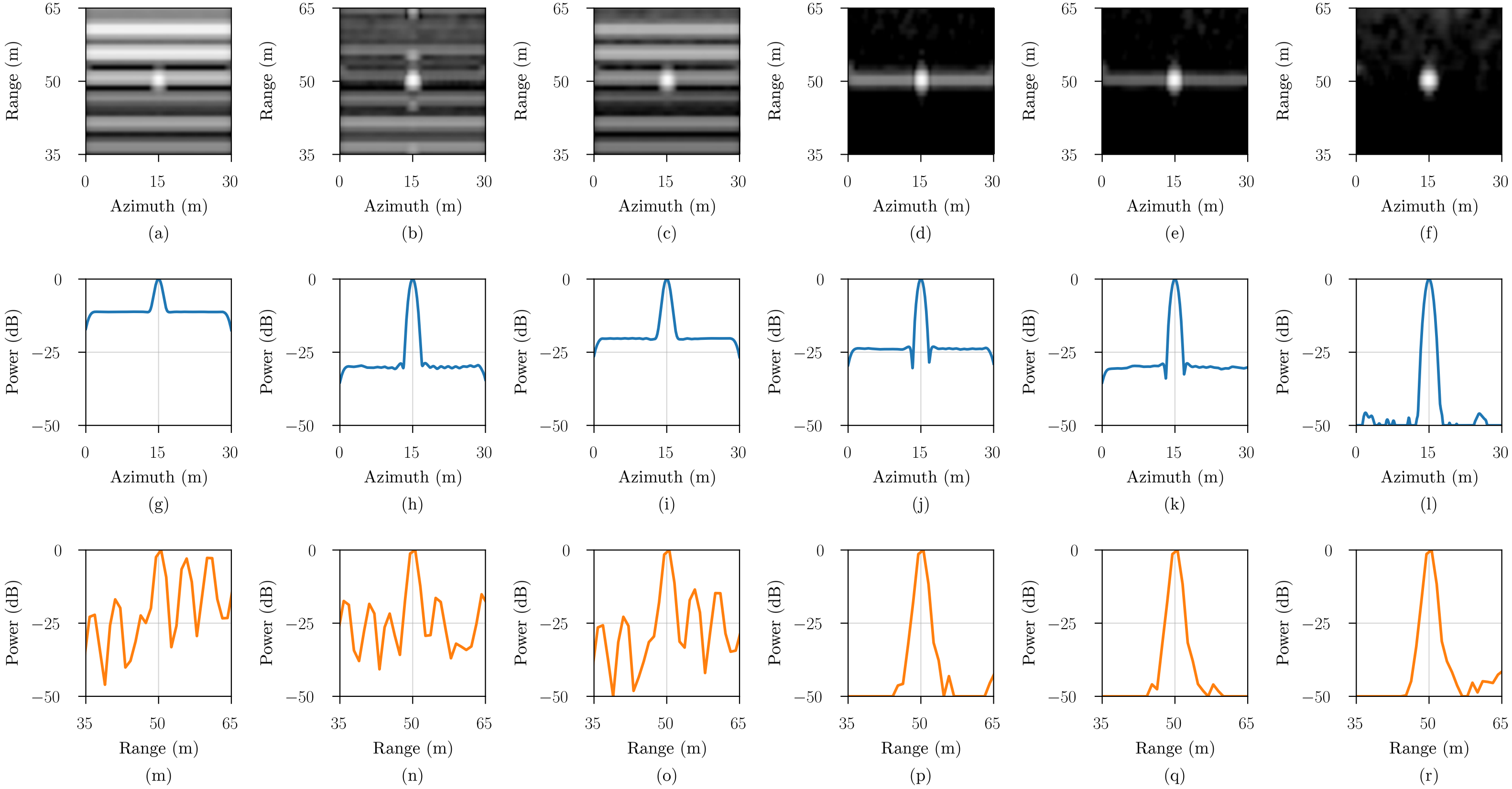

Figure 5.6: Comparison of spur chirp suppression techniques applied to simulated SAR data, presenting the (a)–(f) processed SAR images, (g)–(l) azimuth slices, and (m)–(r) range slices through the peak of the point target. No form of suppression was applied for the results in the first column ((a), (g), (m)). The second column ((b), (h), (n)) presents the results of time-domain zeroing. Loop bandwidth reduction was used to produce the results in the third column ((c), (i), (o)). RDSM was performed for the fourth and fifth columns, for slow-time periods of 1 s and 2 s respectively. The final column ((f), (l), (r)) serves as the control, in which no form of suppression was applied, and no spur chirps were introduced into the beat signal.

Table 5.1: Assessment of Zeroing, Loop Bandwidth Reduction and RDSM

Performance Metric	Spur Chirps	Zeroing	f_{LB}	RDSM (1 s)	RDSM (2 s)	Ideal Case	Unit
RMSE	27.82	18.38	20.27	6.93	5.12	0.00	dB
SSIM	0.01	0.03	0.02	0.35	0.37	1.00	–
PSLR [Azimuth]	11.15	28.76	20.19	23.09	28.82	45.56	dB
PSLR [Range]	4.20	12.76	14.77	44.44	44.49	44.86	dB

Achieving the lowest RMSE and highest SSIM values, the SAR images formed after RDSM were found to be the most similar to the idea case, in terms of both absolute value and perceive difference. Zeroing and RDSM produced the greatest PSLR values in the azimuth slice, where RDSM was seen to improved with an increase in available slow-time samples. Finally, RDSM demonstrated a significant advantage over the alternative techniques in the range slice PSLR, almost matching the ideal case. As such, the tabulated values agree with the qualitative observations: RDSM performed better than zeroing and loop bandwidth reduction in all performance metrics.

It must be noted that the efficacy of loop bandwidth reduction inherently improves as a function of range, while the other suppression techniques are range independent. As such, this simulated short-range scenario does not reveal the full potential of loop bandwidth reduction. Of further interest, this simulation introduced only those spur chirps characterised by $n = d = 1$, and where only present in the zero Doppler bin. These parameters clearly do not capture the full extent of reality, but provide a useful foundation to compare the suppression techniques. In the following Section, these suppression techniques are applied to SAR data measured using the miloSAR.

5.6 Application to Measured SAR Data

During the course of the miloSAR's development, a myriad of system configurations and operational parameters were implemented and assessed. As such, the miloSAR has been used in numerous SAR measurement and testing campaigns.

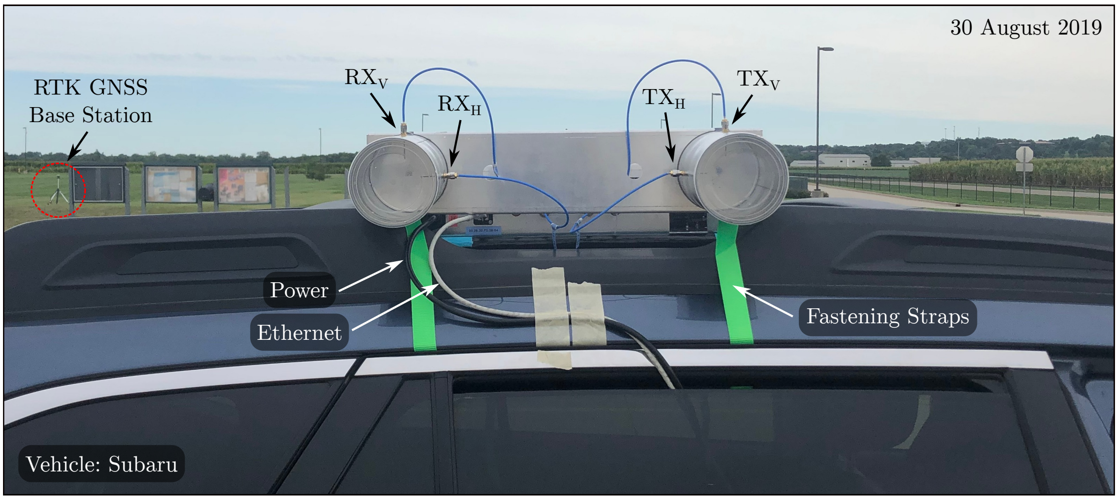

Figure 5.7: miloSAR strapped to the roof of a Subaru. The base station of the RTK GNSS system is visible in the background.

This section presents measurements captured during two specific campaigns which allow the efficacy of zeroing, loop bandwidth reduction and RDSM to be demonstrated and compared.

5.6.1 Iowa, United States of America

Between July and September of 2019, the miloSAR was deployed on seven occasions to capture over 120 car-borne SAR measurements. For these experiments, the radar was strapped to the top of a Subaru at a height of 1.7 m AGL, as seen in Figure 5.7.

All of the experiments conducted during this time period made use of the reduced loop bandwidth configuration, i.e. 42 kHz. As such, a 'before versus after' comparison can not be made between the 'standard' and reduced loop bandwidth configurations. Rather, Figure 5.8 presents a representative result for one such experiment. An optical satellite image of the area (taken from Google Earth) is given in Figure 5.8(a), while Figure 5.8(b) shows the resultant SAR image. Figures 5.8(c) and 5.8(d) both present images taken from the vehicle during the capture.

To produce this SAR image, the vehicle travelled northward along the road at a mean velocity of 14 m/s, with the radar pointing right. Four data channels were

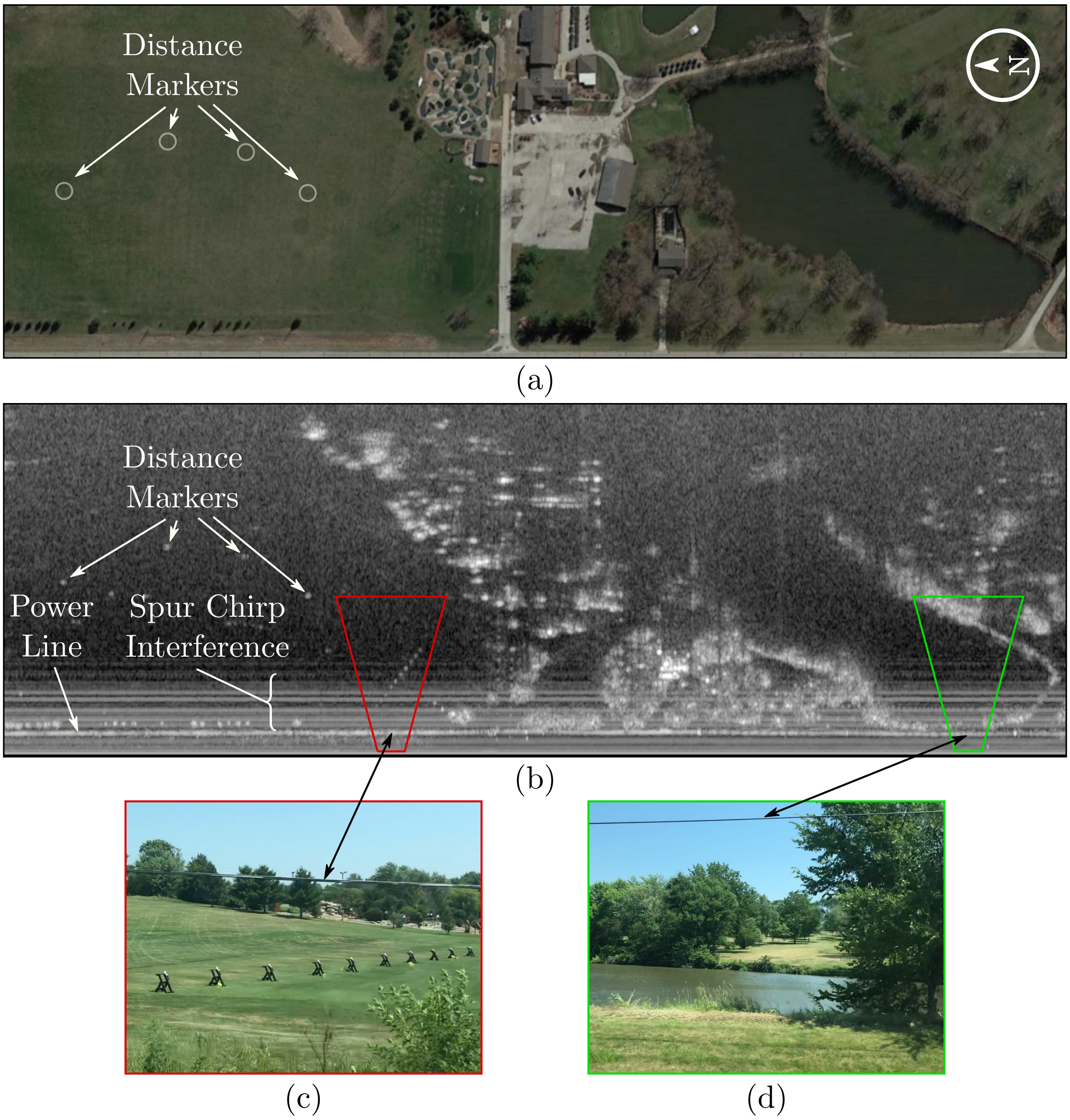

Figure 5.8: (a) Optical satellite image and (b) processed SAR image of a driving range and lake region in Pleasant Hill, Iowa. This SAR image spans an area of 600 m by 200 m, and presents 100 dB of dynamic range. (c) Photo revealing an arrangement of 10 golf bag racks and a power line that runs horizontally in front of the radar. (d) Secondary photo that corresponds to the lake region, where the power line is also visible.

captured (fully-polarimetric operation), processed into independent images, and then non-coherently averaged to form the image in Figure 5.8(b). This reduces the variance of speckle noise and improves image SNR.

Spur chirp interference is visible in the near range of the SAR image, extending up to approximately 50 m down range. This is in line with what was observed in the simulations of the preceding Section. Under the implemented experimental configuration, 42 kHz of loop bandwidth corresponded to a range of 17 m, which means that the impact of spur chirps can be observed at roughly three times the corner frequency of the PLL loop filter. This does not present a problem for airborne measurements where the platform altitude would typically exceed the corrupted near range. An alternative suppression technique is therefore required for near range applications. Somewhat ironically, the following section presents airborne SAR measurements that demonstrate how zeroing and RDSM compare.

5.6.2 Oudtshoorn, South Africa

The miloSAR was deployed in Oudtshoorn, South Africa for a two-day airborne SAR measurement campaign in November, 2018. Four flights enabled a total of 30 data takes, using the wide loop bandwidth setting of 477.8 kHz. For this campaign, the radar was mounted within an Ikarus C42: the two-seater, microlight aircraft seen in Figure 5.9(a).

The waveform parameters utilised during this campaign vary from those used for the simulations and measurements in preceding Sections. For these captures, a fractional numerator increment value of $I = 1060$ was used over $L = 88666$ phase detector cycles, resulting in values of $\Delta T_{\mathrm{int}} = 126.62\,\mu\mathrm{s}$ and $T_{\mathrm{int}_0} = 101.3\,\mu\mathrm{s}$. These values map to the measured spur chirp positions seen in Figure 5.10.

As evidenced by Figure 5.10, the use of a wide loop bandwidth means that these data sets contain the full extent of spur chirp interference. This is an advantage from a research point of view, since both time domain zeroing and RDSM could be applied for comparison of the resultant SAR imagery.

All measurements lasted 60 s and utilised a PRF of 1 kHz, which resulted in 60 000 slow-time pulses per data set. Figure 5.11 illustrates how this extent of slow-time is a significant benefit to RDSM, presenting the averaged RDMs produced before and after RDSM had been implemented to the data in Figure 5.10. The utilised threshold parameters of $W = G = 5$ and $\alpha = 10$ were determined

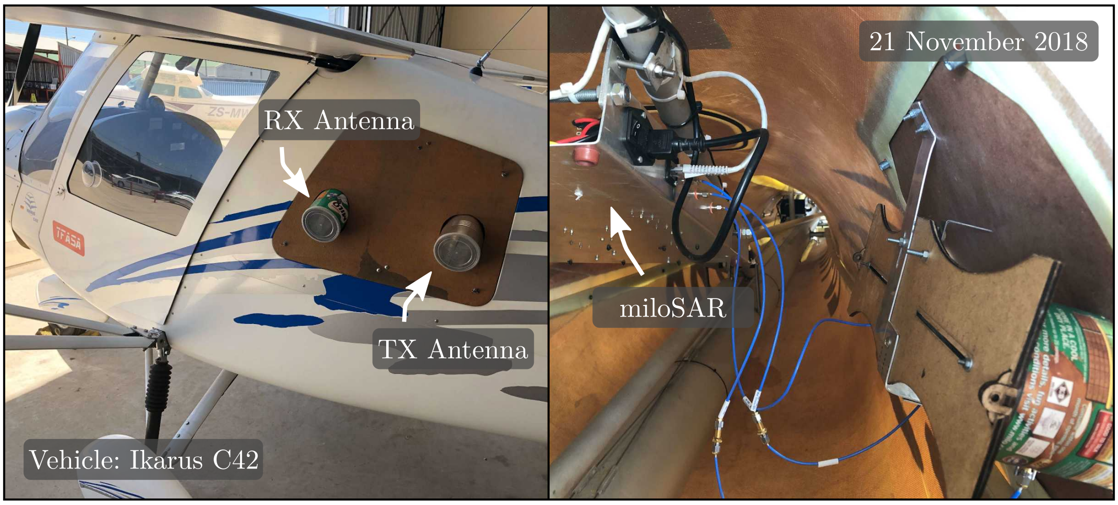

(a) (b)

Figure 5.9: (a) Exterior of the retrofitted Ikarus C42. (b) The internals of the plane's fuselage. Modifications to the baggage hatch supported the cylindrical antennas, with the remaining radar subsystems directly behind them.

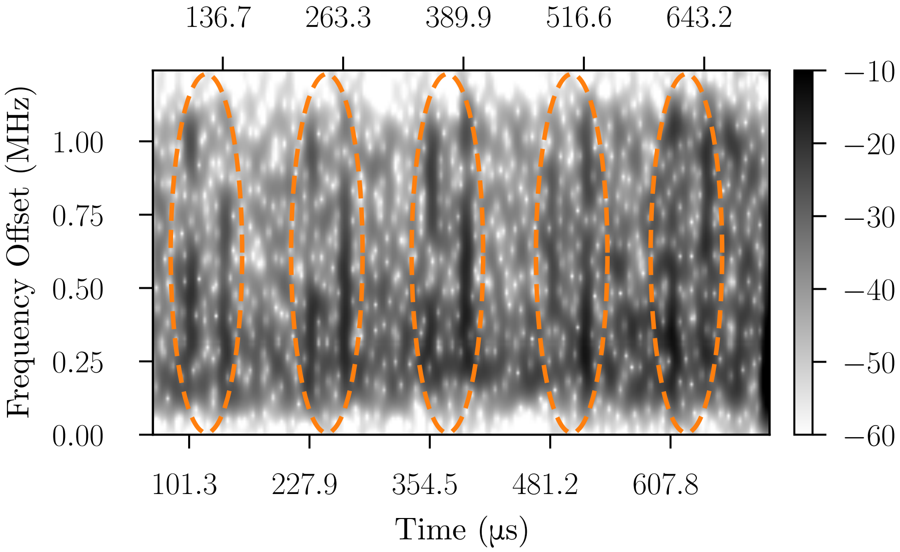

Figure 5.10: Beat signal spectrogram measured during the campaign. The presence of five pairs of spur chirps has been highlighted with dashed ellipses. Axis ticks have been chosen to align with the location of spur chirps.

heuristically.

It is not immediately evident that any part of Figure 5.11(b) has been masked,

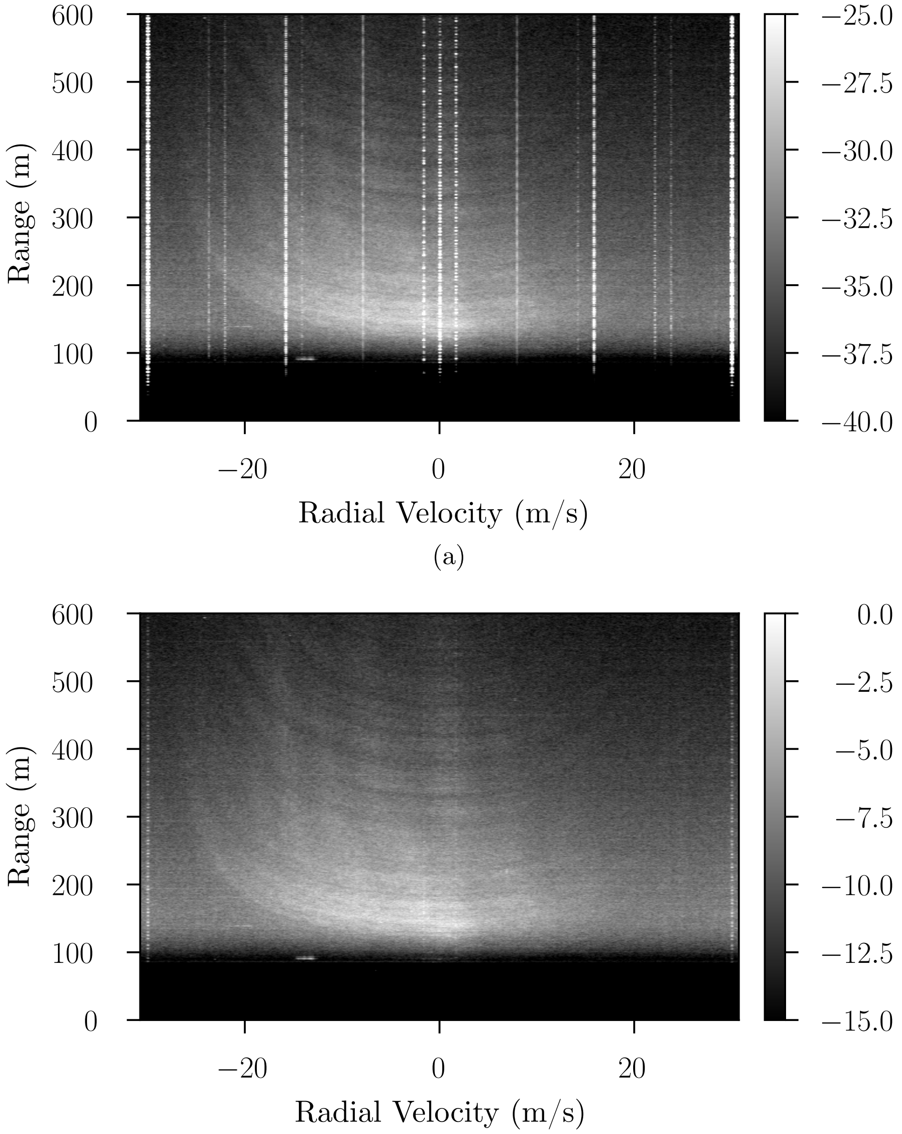

(a)

(b)

Figure 5.11: Comparison between averaged RDMs (a) before and (b) after RDSM. Both plots are normalised and present 15 dB of dynamic range but are offset by 25 dB to account for the integration gain experienced by the interference. The interference has been removed in (b), where only target energy (spread throughout the RDM) remains. The coherent processing interval for these images was limited to 512 pulses, and as such these figures are not equivalent to those in Figure 5.4.

as the masked regions would appear as black vertical lines. This is the benefit of the high resolution of the mask with respect to the averaged RDM. The frequency resolution of the mask is $0.89/60 = 14.8\,\text{mHz}$, while the frequency resolution of Figure 5.11(b) is $0.89/0.512 = 1.73\,\text{Hz}$, since each RDM was generated from 512 pulses. As a result, only 0.15 % of the total available Doppler bins were masked. Since the procedure used to generate these averaged RDM shares commonality with Fourier-based image formation, no masked regions are expected in the final SAR image either.

The efficacy of zeroing and RDSM in eliminating the effects of spur chirp interference from SAR imagery is now assessed through the application of both techniques to the same measured data set. Figure 5.12 presents the resultant SAR images without any form of suppression, with those produced after zeroing and RDSM. A satellite image of the same region (taken from Google Earth) is also provided for reference. A mean altitude of 106 m and velocity of 29 m/s were maintained during the 60 s experiment, enabling an area of 500 m by 1746 m to be captured.

It is clear that both the zeroing and RDSM techniques are able to eliminate horizontal interference lines caused by the spur chirps. However, the application of zeroing has resulted in an undesirable distortion of the resultant SAR image. As was shown in the simulations of Section 5.5, this distortion is due to the high sidelobes associated with the Fourier transform of the masking function. The effect of these sidelobes is most pronounced in the scene's brightest target, which has been enclosed by a dashed rectangle in Figures 5.12(b) and 5.12(c). A vertical line (enclosed by a dashed ellipse) is seen to extend away from the target over all range in Figure 5.12(b). This vertical line is absent, however, from both Figures 5.12(a) and 5.12(c), since it is due to sidelobes in the range dimension.

To assess the difference in sidelobe levels, the regions enclosed by the dashed rectangles in Figures 5.12(b) and 5.12(c) are repeated in Figures 5.13(a) and 5.13(b) respectively. Azimuth and range slices through the peak of the target are presented in each column.

At first glance, the azimuth slices in Figures 5.13(c) and 5.13(d) appear to be fairly similar. However, there are points in these profiles that differ significantly. At the points labelled A and B, the RDSM profile exhibits content approximately

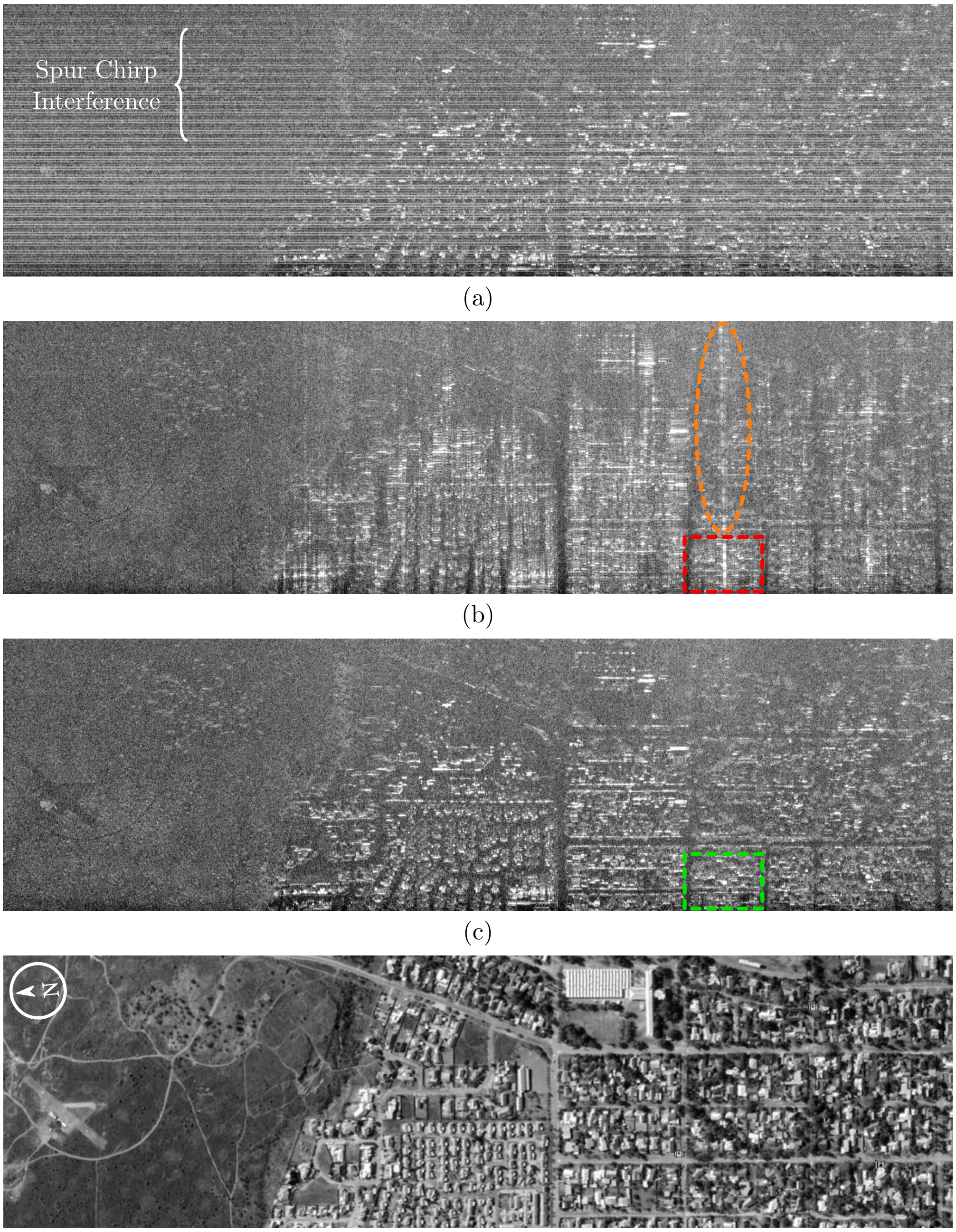

(a)

(b)

(c)

(d)

Figure 5.12: (a) SAR image without suppression, (b) SAR image after zeroing, (c) SAR image after RDSM, and (d) reference optical satellite image taken from Google Earth. All SAR images are presented over 80 dB of dynamic range, and are the non-coherent average of VV and VH channels. The aircraft flew southwards, with the radar pointing east.

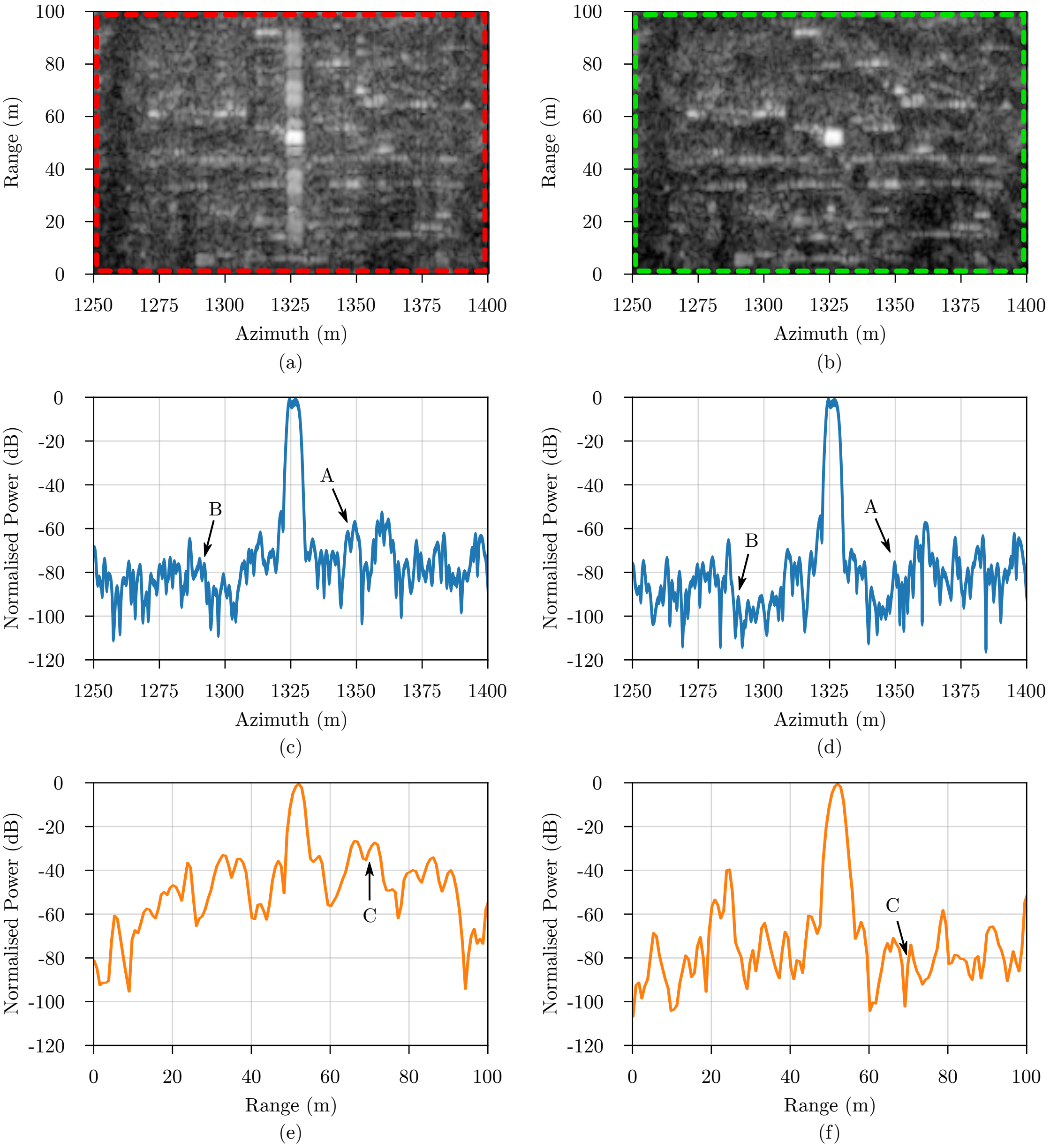

(a) (b) (c) (d) (e) (f)

Figure 5.13: Analysis of the brightest target response of Figure 5.12. (a) SAR image after zeroing and (b) SAR image after RDSM. Azimuth and range slices through the target peak are presented in (c)–(d) and (e)–(f) respectively.

20 dB lower than that in the zeroing profile. This is attributed to the high selectivity of the RDSM masking function. The range slices also reveal a significant difference in sidelobe levels surrounding the target. At a range of 70 m (label C) the profiles differ by more than 45 dB. These results agree with the simulations of Section 5.5 where RDSM was found to outperform zeroing in both azimuth and range slice sidelobe levels.

5.7 Conclusions

This chapter explored several techniques that were designed to either avoid or mitigate the impact of spur chirp interference. A subset of these techniques were applied to both simulated and measured SAR data sets for comparison.

The presented avoidance guidelines place undesirable constraints on the operational parameters on the radar. As a result, these guidelines are expected to be overlooked in practice, in favour of suppression techniques. The implementation of a variable PLL reference frequency for FMCW applications is left for future work.

A set of mutual interference suppression techniques were identified as transferable to the problem of spur chirps. These transferable techniques do not, however, leverage the unique properties of spur chirps and are thus not optimised for the problem at hand. The implementation of OMP, MCA and model based interpolation are left for future work.

Loop bandwidth reduction through adjustment of CPG was found to be an effective method of spur chirp suppression. However, it came at the cost of increased PLL settling time and VCO-induced phase noise. Furthermore, this technique was found to be ineffective in near range which corresponds to the PLL loop filter bandwidth. As such, loop bandwidth reduction is reserved for airborne applications, where the near range is devoid of targets and is typically discarded.

A novel spur chirp suppression technique, termed RDSM, was put forward. This technique leverages the sparsity of spur chirp interference in the range-Doppler domain, where the interference can be filtered out at high resolution.

The efficacy of zeroing, loop bandwidth reduction and RDSM was assessed using simulated and measured SAR data, where RDSM was found to outperform the other techniques in terms of RMSE, SSIM and PSLR in the azimuth and range domains.

Chapter 6

Conclusion

The work presented in this text has proved the hypothesis to be true: low-cost heterodyne FMCW SAR can be implemented using a pair of time-offset fractional-N PLLs, with the caveat that additional processing steps are required to suppress the spur chirps that effect the performance of such a system.

6.1 Research Questions

All of the research questions that were posed in Chapter 1 have been answered in the course of the text. A summary of these answers is provided below.

1. Why use a pair of fractional-N PLLs to implement a heterodyne FMCW SAR?

   The literature review presented in Chapter 2 revealed that fractional-N PLLs offer a low-cost solution to the linear frequency requirements of FMCW radar. These devices support direct waveform synthesis at RF, which eliminates the need for typical up-conversion components, reducing hardware costs and complexity. Furthermore, a pair of these inexpensive devices can be used to implement a heterodyne receiver architecture with a variable IF, using either a relative time or frequency offset. A heterodyne receiver with a variable IF enables effective analogue range gate based feed-through suppression in varying experimental conditions and enables the recovery of wasted bandwidth in SAR applications.

2. Can such a radar operate coherently without a reference channel?

   System characterisation tests presented in Chapter 3 demonstrated that a time-offset based heterodyne receiver architecture is capable of precise phase measurement over an extended period of time, without the need for a reference channel. This is in contrast to the more conventional frequency offset approach, which requires a reference channel to account for uncertainty in the instantaneous frequency difference between fractional-N PLLs. This represented a major benefit for the miloSAR, as both of the available receiver channels could be used for fully polarimetric operation.

3. Do the notorious spurious signals generated by fractional-N PLLs affect the images produced by this SAR?

   Chapter 4 presented an investigation into the manifestation of IBS and PDH as spur chirps in data measured by the miloSAR. The beat signal spur chirps were found to generate Fresnel ripples in the range profile that appeared in select Doppler frequency bins in the RDM. Azimuth compression during SAR processing was found to intensify the presence of spur chirp interference in the resultant imagery. Simulations revealed that spur chirps can cause significant degradation of SAR image quality, measured in terms of PSLR, RMSE and SSIM with respect to an ideal case.

4. If these spurious signals do present a problem, how can they be suppressed effectively?

   Guidelines for avoiding and techniques for suppressing spur chirp interference were put forward in Chapter 5. Several suppression techniques from the problem of mutual interference were identified as transferable, of which time-domain zeroing was selected for implementation. Time-domain zeroing, PLL loop bandwidth reduction through CPG adjustment, and the novel RDSM technique were compared using simulated and measured SAR data sets. This comparison revealed that RDSM outperformed the alternatives and provides an effective method of spur chirp suppression for SAR applications. As such, the development of RDSM is responsible for ensuring the viability of the miloSAR as a low-cost FMCW SAR.

6.2 Original Contributions

The following set of original contributions are a result of answering the aforementioned the research questions.

1. Implementation of the only fully-polarimetric heterodyne FMCW SAR to employ a pair of time-offset fractional-N PLLs.
2. Identification, simulation and measurement of the *spur chirps* which affect this system.
3. Presentation of guidelines for the avoidance of spur chirps.
4. Identification of existing, transferable techniques for the suppression of spur chirps.
5. Demonstration of spur chirp suppression through PLL loop bandwidth reduction.
6. Presentation of RDSM: a novel spur chirp suppression technique.
7. A comparison between time-domain zeroing, loop bandwidth reduction and RDSM for the suppression of spur chirps, using simulated and measured SAR data.

6.3 Future Work

Scope exists for future work in fractional-N PLL based heterodyne FMCW SAR in the following areas.

- It would be interesting to determine if the power cancellation techniques reviewed in Chapter 2 would be effective in eliminating spurs generated by the fractional-N PLLs, before dechirp occurs. It is hypothesised that the efficacy of this approach would depend on the cancellation bandwidth, which would be required to well exceed the PLL loop bandwidth.

- The sparse representation and model based interpolation techniques reviewed in Chapter 5 could be implemented to suppress spur chirp interference. Analysis of the efficacy and computational expense of these techniques would be enlightening.

- The impact of spur chirps on fractional-N PLL based homodyne FMCW SAR systems could be investigated. While a DX fractional-N PLL would no longer be necessary, spur chirp interference is expected to still present a problem. This could, however, be generalised by assessing the impact of spur chirps as a function of the time-offset.

- The SAR image quality of a time-offset fractional-N PLL based heterodyne FMCW SAR (coupled with RDSM) could be compared with an equivalent system that employs time-offset DDSs. The miloSAR and SlimSAR are ideal candidates for such a study.

- If the Doppler frequency bins in which spur chirp interference appears in the RDM could be accurately predicted, the need for the CFAR based thresholding within RDSM would be eliminated. This may offer a reduction in the computational cost of RDSM.

Bibliography

[1] G. L. Charvat, *Small and Short-Range Radar Systems.* Boca Raton, FL, USA: CRC Press, 2014.

[2] M. Edwards, D. Madsen, C. Stringham, A. Margulis, B. Wicks, and D. G. Long, "microASAR: A small, robust LFM-CW SAR for operation on UAVs and small aircraft," in *Proc. IEEE Int. Geosci. Remote Sens. Symp. (IGARSS)*, vol. 5, Jul. 2008, pp. 514–517.

[3] C. Stringham, D. G. Long, B. Wicks, and G. Ramsey, "Digital receiver design for an offset IF LFM-CW SAR," in *Proc. IEEE RadarCon (RADAR)*, May 2011, pp. 960–964.

[4] K. Lin, R. H. Messerian, and Y. Wang, "A digital leakage cancellation scheme for monostatic FMCW radar," in *Proc. IEEE MTT-S Int. Microw. Symp. Dig.*, vol. 2, Jun. 2004, pp. 747–750.

[5] K. Lin, Y. E. Wang, C. K. Pao, and Y. C. Shih, "A Ka-band FMCW radar front-end with adaptive leakage cancellation," *IEEE Trans. Microw. Theory Techn.*, vol. 54, no. 12, pp. 4041–4048, Dec. 2006.

[6] S. Xiu-kun and H. Jian, "Development of RF front-end with high T/R isolation for Ka band mono-antenna FMCW radar," in *Proc. IEEE CIE Int. Conf. Radar*, vol. 1, Oct. 2011, pp. 276–279.

[7] B. Razavi, "Design considerations for direct-conversion receivers," *IEEE Trans. Circuits Syst. II*, vol. 44, no. 6, pp. 428–435, Jun. 1997.

[8] B. Boukari, E. Moldovan, S. Affes, K. Wu, R. G. Bosisio, and S. O. Tatu, "A heterodyne six-port FMCW radar sensor architecture based on beat signal phase slope techniques," *Prog. Electromagn. Res.*, vol. 93, pp. 307–322, 2009.

[9] I. Tchekashkin, "Design and implementation of a low-cost FMCW imaging radar," M.Sc. dissertation, Dept. Elect. Eng., Univ. Cape Town, Cape Town, South Africa, 2015.

[10] E. Zaugg, M. Edwards, and A. Margulis, "The SlimSAR: A small, multi-frequency, synthetic aperture radar for UAS operation," in *Proc. IEEE Radar Conf.*, May 2010, pp. 277–282.

[11] B. Kim, J.-S. Koo, D. Kim, and S. Nam, "A wall-clutter rejection technique using two PLLs and a phase controller for wall-penetrating FMCW radar," *IEEE Geosci. Remote Sens. Lett.*, vol. 14, no. 4, pp. 471–474, Apr. 2017.

[12] D. A. Jordan, M. R. Inggs, and M. Y. Abdul Gaffar, "Suppression of spur chirps for fractional-N PLL-based heterodyne FMCW SAR," *IEEE Trans. Microw. Theory Techn.*, vol. 69, no. 1, pp. 409–417, Jan. 2021.

[13] P. D. L. Beasley, "The influence of transmitter phase noise on FMCW radar performance," in *Proc. Eur. Radar Conf. (EuRAD)*, Sep. 2006, pp. 331–334.

[14] Z. Li and K. Wu, "On the leakage of FMCW radar front-end receiver," in *Proc. Global Symp. Millimeter Waves*, Apr. 2008, pp. 127–130.

[15] J. Park, S. Park, D.-H. Kim, and S.-O. Park, "Leakage mitigation in heterodyne FMCW radar for small drone detection with stationary point concentration technique," *IEEE Trans. Microw. Theory Techn.*, vol. 67, no. 3, pp. 1221–1232, Mar. 2019.

[16] X. Guo, Y. Gao, K. Wang, and X. Liu, "Isolation improvement method for frequency modulated continuous wave SAR," in *Proc. IEEE Radar Conf. (RadarConf)*, May 2017, pp. 641–644.

[17] W. L. Melvin and J. A. Scheer, *Principles of Modern Radar, Vol. III: Radar Applications.* Edison, NJ, USA: SciTech Publishing, 2014.

[18] G. M. Brooker, D. Birch, and J. Solms, “W-band airborne interrupted frequency modulated CW imaging radar,” *IEEE Trans. Aerosp. Electron. Syst.*, vol. 41, no. 3, pp. 955–972, Jul. 2005.

[19] S. Hamran, T. Berger, L. Hanssen, and M. J. Oyan, “Gated FMCW SAR system,” in *Proc. 38th Eur. Microw. Conf.*, Oct. 2008, pp. 1644–1647.

[20] R. H. Khan and D. K. Mitchell, “Waveform analysis for high-frequency FMICW radar,” *IEE Proceedings F - Radar and Signal Processing*, vol. 138, no. 5, pp. 411–419, Oct. 1991.

[21] J. A. McGregor, E. M. Poulter, and M. J. Smith, “Switching system for single antenna operation of an S-band FMCW radar,” *IEE Proceedings - Radar, Sonar and Navigation*, vol. 141, no. 4, p. 241, Aug. 1994.

[22] J.-G. Kim, S. Ko, S. Jeon, J.-W. Park, and S. Hong, “Balanced topology to cancel Tx leakage in CW radar,” *IEEE Microw. Wireless Compon. Lett.*, vol. 14, no. 9, pp. 443–445, Sep. 2004.

[23] T. Venkatamuni, L. S. Sudhakara Sarma, and A. T. Kalghatgi, “Adaptive reflected power canceller for single antenna FMCW radar,” in *Proc. Asia Pacific Microw. Conf.*, Dec. 2009, pp. 1841–1844.

[24] P. V. Brennan, Y. Huang, M. Ash, and K. Chetty, “Determination of sweep linearity requirements in FMCW radar systems based on simple voltage-controlled oscillator sources,” *IEEE Trans. Aerosp. Electron. Syst.*, vol. 47, no. 3, pp. 1594–1604, Jul. 2011.

[25] I. M. Milosavljević, Đ. P. Glavonjić, D. P. Krčum, L. V. Saranovac, and V. M. Milovanović, “A highly linear and fully-integrated FMCW synthesizer for 60 GHz radar applications with 7 GHz bandwidth,” *Analog Integr. Circuits Signal Process.*, vol. 90, no. 3, pp. 591–604, Mar. 2017.

[26] S. O. Piper, “Homodyne FMCW radar range resolution effects with sinusoidal nonlinearities in the frequency sweep,” in *Proc. Int. Radar Conf.*, May 1995, pp. 563–567.

[27] D. Weyer, M. B. Dayanik, L. Jie, A. Albalawi, A. Alothaimen, M. Aseeri, and M. P. Flynn, “Design considerations for integrated radar chirp synthesizers,” *IEEE Access*, vol. 7, pp. 13 723–13 736, Jan. 2019.

[28] A. Meta, P. Hoogeboom, and L. Ligthart, “Range non-linearities correction in FMCW SAR,” in *Proc. IEEE Int. Geosci. Remote Sens. Symp. (IGARSS)*, Jul. 2006, pp. 403–406.

[29] P. J. Burke, “Ultra-linear chirp generation via VCO tuning predistortion,” in *Proc. IEEE MTT-S Int. Microw. Symp. Dig.*, May 1994, pp. 957–960.

[30] J. Detlefsen, A. Dallinger, S. Schelkshorn, and S. Bertl, “UWB millimeter-wave FMCW radar using Hubert transform methods,” in *Proc. IEEE 9th Int. Symp. Spread Spectr. Techn. Appl.*, Aug. 2006, pp. 46–48.

[31] A. Anghel, G. Vasile, R. Cacoveanu, C. Ioana, and S. Ciochina, “Short-range wideband FMCW radar for millimetric displacement measurements,” *IEEE Trans. Geosci. Remote Sens.*, vol. 52, no. 9, pp. 5633–5642, Sep. 2014.

[32] P. D. L. Beasley, “Advances in millimetre wave FMCW radar,” in *Proc. Microw. Radar Remote Sens. Symp.*, Sep. 2008, pp. 246–249.

[33] S. Scheiblhofer, S. Schuster, and A. Stelzer, “High-speed FMCW radar frequency synthesizer with DDS based linearization,” *IEEE Microw. Wireless Compon. Lett.*, vol. 17, no. 5, pp. 397–399, May 2007.

[34] *LMX2492/LMX2492-Q1 14 GHz Low Noise Fractional N PLL with Ramp/Chirp Generation (Rev. B)*, Texas Instruments, Dallas, TX, USA, (2015). [Online]. Available: https://www.ti.com/lit/gpn/lmx2492

[35] G. M. Brooker, “Understanding millimetre wave FMCW radars,” in *Proc. 1st Int. Conf. Sens. Technol.*, Nov. 2005, pp. 152–157.

[36] S. Yamada, O. Boric-Lubecke, and V. M. Lubecke, “Cancellation techniques for LO leakage and DC offset in direct conversion systems,” in *Proc. IEEE MTT-S Int. Microw. Symp. Dig.*, Jun. 2008, pp. 1191–1194.

[37] B. Meyer, J. B. de Swardt, and P. van der Merwe, “Comparing baseband and intermediate frequency FMCW radar receivers,” in *Proc. IEEE AFRICON*, Sep. 2017, pp. 563–568.

[38] R. Feger, C. Wagner, and A. Stelzer, “An IQ-modulator based heterodyne 77-GHz FMCW radar,” in *Proc. German Microw. Conf. (GeMIC)*, Mar. 2011, pp. 1–4.

[39] T. Saito, N. Okubo, Y. Kawasaki, O. Isaji, and H. Suzuki, “An FM-CW radar module with front-end switching heterodyne receiver,” in *Proc. IEEE MTT-S Microw. Symp. Dig.*, Jun. 1992, pp. 713–716.

[40] R. Feger, H. J. Ng, C. Pfeffer, and A. Stelzer, “A delta-sigma transmitter based heterodyne FMCW radar,” in *Proc. Eur. Radar Conf. (EuRAD)*, Oct. 2013, pp. 208–211.

[41] E. C. Zaugg, M. C. Edwards, and A. Margulis, “The SlimSAR: A compact, flexible, high-performance, polarimetric, multi-band SAR for operation on a small UAS,” in *Proc. 8th Eur. Conf. Synthetic Aperture Radar*, Jun. 2010, pp. 1–4.

[42] E. C. Zaugg, M. C. Edwards, and A. Margulis, “Theoretical and practical design considerations for a small, multi-band SAR: The SlimSAR,” in *Proc. IEEE Int. Geosci. Remote Sens. Symp. (IGARSS)*, Jul. 2010, pp. 126–129.

[43] E. Zaugg, M. Edwards, B. Wilmhoff, and L. Westbrook, “Multi-frequency, single-aperture SAR,” in *Proc. IEEE RadarCon (RADAR)*, May 2011, pp. 554–558.

[44] R. Feger, E. Kolmhofer, F. Starzer, F. Wiesinger, S. Scheiblhofer, and A. Stelzer, “A heterodyne 77-GHz FMCW radar with offset PLL frequency stabilization,” in *Proc. IEEE Top. Conf. Wireless Sensors Sensor Netw.*, Jan. 2011, pp. 9–12.

[45] M.-T. Dao, D.-H. Shin, Y.-T. Im, and S.-O. Park, “A two sweeping VCO source for heterodyne FMCW radar,” *IEEE Trans. Instrum. Meas.*, vol. 62, no. 1, pp. 230–239, Jan. 2013.

[46] J.-S. Suh, L. Minz, D.-H. Jung, H.-S. Kang, J.-W. Ham, and S.-O. Park, “Drone-based external calibration of a fully synchronized Ku-band heterodyne FMCW radar,” *IEEE Trans. Instrum. Meas.*, vol. 66, no. 8, pp. 2189–2197, Aug. 2017.

[47] B. Kim, D. Kim, Y. Lim, D. Yang, S. Nam, and J.-H. Song, “A clutter rejection technique using a delay-line for wall-penetrating FMCW radar,” *IEICE Trans. Electron.*, vol. E99.C, no. 5, pp. 597–600, May 2016.

[48] J. H. Choi, J. H. Jang, and J. E. Roh, “Optical-delay-based wide-range FMCW radar altimeter,” *Electron. Lett.*, vol. 50, no. 25, pp. 1975–1977, Dec. 2014.

[49] J.-H. Choi, J.-H. Jang, and J.-E. Roh, “Design of an FMCW radar altimeter for wide-range and low measurement error,” *IEEE Trans. Instrum. Meas.*, vol. 64, no. 12, pp. 3517–3525, Dec. 2015.

[50] M. P. Kennedy, “Nonlinearity-induced spurs in fractional-N frequency synthesizers: State of the art,” in *Proc. 26th IEEE Int. Conf. Electron. Circuits Syst. (ICECS)*, Nov. 2019, pp. 823–826.

[51] P. V. Brennan, H. Wang, D. Jiang, and P. M. Radmore, “A new mechanism producing discrete spurious components in fractional-N frequency synthesizers,” *IEEE Trans. Circuits Syst. I*, vol. 55, no. 5, pp. 1279–1288, Jun. 2008.

[52] A. Lauer, R. Follmann, M. Quibeldey, and D. Köther, “A fractional-N PLL spur and phase noise simulator,” in *Proc. 6th Eur. Microw. Integr. Circuit Conf.*, Oct. 2011, pp. 418–421.

[53] S. A. Osmany, F. Herzel, and J. C. Scheytt, “Analysis and minimization of substrate spurs in fractional-N frequency synthesizers,” *Analog Integr. Circuits Signal Process.*, vol. 74, no. 3, pp. 545–556, Mar. 2013.

[54] V. S. Sadeghi, H. Miar Naimi, and M. P. Kennedy, “The role of charge pump mismatch in the generation of integer boundary spurs in fractional-N frequency synthesizers: Why worse can be better,” *IEEE Trans. Circuits Syst. II*, vol. 60, no. 12, pp. 862–866, Dec. 2013.

[55] V. Mazzaro and M. P. Kennedy, “Mitigation of “Horn Spurs” in a MASH-based fractional-N CP-PLL,” *IEEE Trans. Circuits Syst. II*, vol. 67, no. 5, pp. 821–825, May 2015.

[56] F. Herzel and D. Kissinger, “Design and layout strategies for integrated frequency synthesizers with high spectral purity,” *Int. J. Microw. Wireless Technol.*, vol. 9, no. 9, pp. 1791–1797, Nov. 2017.

[57] D. Mai, A. Dahlan, and M. P. Kennedy, “MASH DDSM-induced spurs in a fractional-N frequency synthesizer,” in *Proc. 26th IEEE Int. Conf. Electron. Circuits Syst. (ICECS)*, Nov. 2019, pp. 13–16.

[58] V. Mazzaro and M. P. Kennedy, “Another moving spur phenomenon observed in a MASH-based fractional-N PLL,” in *Proc. 30th Irish Signals Syst. Conf. (ISSC)*, Jun. 2019, pp. 1–5.

[59] D. Banerjee, *PLL Performance, Simulation and Design*, 5th ed. Indianapolis, IN, USA: Dog Ear Publishing (LLC), 2017.

[60] L. Grimaldi, D. Cherniak, W. Grollitsch, and R. Nonis, “Analysis of spurs impact in PLL-based FMCW radar systems,” in *Proc. IEEE Int. Symp. Circuits Syst. (ISCAS)*, Oct. 2020, pp. 1–4.

[61] W. Wu, R. B. Staszewski, and J. R. Long, “A 56.4-to-63.4 GHz multi-rate all-digital fractional-N PLL for FMCW radar applications in 65 nm CMOS,” *IEEE J. Solid-State Circuits*, vol. 49, no. 5, pp. 1081–1096, May 2014.

[62] J. Lee, Y. Li, M. Hung, and S. Huang, “A fully-integrated 77-GHz FMCW radar transceiver in 65-nm CMOS technology,” *IEEE J. Solid-State Circuits*, vol. 45, no. 12, pp. 2746–2756, Dec. 2010.

[63] K. Higuchi, H. Nakamizo, H. Mizutani, T. Suzuki, K. Tajima, and K. Kawakami, “A spur suppression method in FMCW radar by reducing the frequency variation periodicity with a PLL,” in *Proc. 44th Eur. Microw. Conf.*, Oct. 2014, pp. 1024–1027.

[64] D. Jordan, P. Cheng, M. Inggs, A. Langman, and Y. A. Gaffar, “Development of the miloSAR testbed for the one kilogramme radioCamera SAR for small drones,” in *Proc. IEEE Radar Conf. (RadarConf)*, Apr. 2019, pp. 1–6.

[65] T. Barris, “Modelling and resolving of the ambiguous angle of arrival measurements of the SANAE IV SuperDARN radar,” M.Sc. dissertation, Dept. Elect. Eng., Univ. Cape Town, Cape Town, South Africa, 2017.

[66] *LMX2492EVM User’s Guide (Rev. D)*, Texas Instruments, Dallas, TX, USA, (2015). [Online]. Available: https://www.ti.com/lit/pdf/snau160

[67] M. B. Dayanik and M. P. Flynn, “Digital fractional-N PLLs based on a continuous-time third-order noise-shaping time-to-digital converter for a 240-GHz FMCW radar system,” *IEEE J. Solid-State Circuits*, vol. 53, no. 6, pp. 1719–1730, Jun. 2018.

[68] M. A. Richards, *Fundamentals of Radar Signal Processing*, 2nd ed. New York, NY, USA: McGraw-Hill, 2014.

[69] S. Scholl, “Exact Signal Measurements Using FFT Analysis,” Fachbereich Elektrotechnik und Informationstechnik, Tech. Rep., Jan. 2016. [Online]. Available: http://nbn-resolving.de/urn:nbn:de:hbz:386-kluedo-42930

[70] G. Heinzel, A. Rüdiger, and R. Schilling, “Spectrum and spectral density estimation by the discrete Fourier transform (DFT), including a comprehensive list of window functions and some new flat-top windows,” Albert-Einstein-Institut, Tech. Rep., Feb. 2002. [Online]. Available: http://hdl.handle.net/11858/00-001M-0000-0013-5579-7

[71] *Fast Analog IO*, Red Pitaya, Solkan, Slovenia, 2017. [Online]. Available: https://redpitaya.readthedocs.io/en/latest/developerGuide/125-14/fastIO.html

[72] M. A. Richards, “Coherent integration loss due to white Gaussian phase noise,” *IEEE Signal Process. Lett.*, vol. 10, no. 7, pp. 208–210, Jul. 2003.

[73] J. M. Horrell, “Range-Doppler synthetic aperture radar processing at VHF frequencies,” Ph.D. thesis, Dept. Elect. Eng., Univ. Cape Town, Cape Town, South Africa, 1999.

[74] K. Siddiq, M. K. Hobden, S. R. Pennock, and R. J. Watson, "Phase noise in FMCW radar systems," *IEEE Trans. Aerosp. Electron. Syst.*, vol. 55, no. 1, pp. 70–81, Feb. 2019.

[75] M. Kowatsch and H. Stocker, "Effect of Fresnel ripples on sidelobe suppression in low time-bandwidth product linear FM pulse compression," in *IEE Proceedings F (Communications, Radar and Signal Processing)*, vol. 129, no. 1, 1982, pp. 41–44.

[76] C. E. Cook and M. Bernfield, *Radar Signals: An Introduction to Theory and Application.* New York, NY, USA: Academic (Press Inc.), 1967.

[77] M. Brooker, "The design and implementation of a simulator for multistatic radar systems," Ph.D. thesis, Dept. Elect. Eng., Univ. Cape Town, Cape Town, South Africa, 2008.

[78] *LMX2595* 20 GHz *Wideband RF Synthesizer With Phase Synchronization & JESD204B Support*, Texas Instruments, Dallas, TX, USA, 2019. [Online]. Available: https://www.ti.com/lit/gpn/lmx2595

[79] *ADF4372 Microwave Wideband Synthesizer With Integrated VCO*, Analog Devices, Norwood, MA, USA, 2019. [Online]. Available: https://www.analog.com/media/en/technical-documentation/data-sheets/adf4372.pdf

[80] D. Banerjee, "Using a programmable input multiplier to minimize integer boundary spurs," Texas Instruments, Dallas, TX, USA, Tech. Rep. SNAA289, 2016. [Online]. Available: https://www.ti.com/lit/pdf/snaa289

[81] G. M. Brooker, "Mutual interference of millimeter-wave radar systems," *IEEE Trans. Electromagn. Compat.*, vol. 49, no. 1, pp. 170–181, Feb. 2007.

[82] M. Barjenbruch, D. Kellner, K. Dietmayer, J. Klappstein, and J. Dickmann, "A method for interference cancellation in automotive radar," in *Proc. IEEE MTT-S Int. Conf. Microw. Intell. Mobility (ICMIM)*, Apr. 2015, pp. 1–4.

[83] J. Bechter, F. Roos, M. Rahman, and C. Waldschmidt, "Automotive radar interference mitigation using a sparse sampling approach," in *Proc. Eur. Radar Conf. (EURAD)*, Oct. 2017, pp. 90–93.

[84] S. Neemat, O. Krasnov, and A. Yarovoy, “An interference mitigation technique for FMCW radar using beat-frequencies interpolation in the STFT domain,” *IEEE Trans. Microw. Theory Techn.*, vol. 67, no. 3, pp. 1207–1220, Mar. 2019.

[85] A. Correas-Serrano and M. A. Gonzalez-Huici, “Sparse reconstruction of chirplets for automotive FMCW radar interference mitigation,” in *Proc. IEEE MTT-S Int. Conf. Microw. Intell. Mobility (ICMIM)*, Apr. 2019, pp. 1–4.

[86] F. Uysal, “Synchronous and asynchronous radar interference mitigation,” *IEEE Access*, vol. 7, pp. 5846–5852, Jan. 2019.

[87] D. A. Jordan, M. R. Inggs, and M. Y. Abdul Gaffar, “Integer boundary spur considerations for fractional-N PLL based FMCW radar,” *Electron. Lett.*, vol. 56, no. 14, pp. 729–732, Jul. 2020.

[88] M. C. Budge and M. P. Burt, “Range correlation effects in radars,” in *Proc. Nat. Radar Conf.*, Apr. 1993, pp. 212–216.

[89] H. Beise, T. Stifter, and U. Schröder, “Virtual interference study for FMCW and PMCW radar,” in *Proc. 11th German Microw. Conf. (GeMiC)*, Mar. 2018, pp. 351–354.